University of Cyprus

BERGISCHE UNIVERSITÄT WUPPERTAL

DEPARTMENT OF PHYSICS

MODEL STUDY OF CHARM LOOP EFFECTS

SALVATORE CALÌ

A dissertation submitted to the University of Cyprus in partial fulfillment of the requirements for the degree of Doctor of Philosophy and submitted to the University of Wuppertal in partial fulfillment of the requirements for the degree of Doctor Rerum Naturalium.

JUNE 2019

The PhD thesis can be quoted as follows:

urn:nbn:de:hbz:468-20190703-093913-4
[http://nbn-resolving.de/urn/resolver.pl?urn=urn%3Anbn%3Ade%3Ahbz%3A468-20190703-093913-4]

DOI: 10.25926/n9mr-f664
[https://doi.org/10.25926/n9mr-f664]

VALIDATION PAGE

Doctoral Candidate: Salvatore Calì

Dissertation Title: Model study of charm loop effects

The present Doctoral Dissertation was submitted in partial fulfillment of the requirements for the degree of Doctor of Philosophy at the Department of Physics of the University of Cyprus and for the degree of Doctor Rerum Naturalium at the Department of Physics of the University of Wuppertal, and was approved on June 1, 2019 by the members of the Examination Committee.

Examination Committee:

Prof. Dr. Francesco Knechtli, Research Supervisor

Prof. Dr. Haralambos Panagopoulos, Research Supervisor

Prof. Dr. Constantia Alexandrou

Prof. Dr. Luigi Del Debbio

Prof. Dr. Andreas Frommer

Prof. Dr. Mike Peardon

“Things on a very small scale behave like nothing that you have any direct experience about. They do not behave like waves, they do not behave like particles, they do not behave like clouds, or billiard balls, or weights on springs, or like anything that you have ever seen.”

Richard Phillips Feynman

DECLARATION OF DOCTORAL CANDIDATE

The present doctoral dissertation was submitted in partial fulfillment of the requirements for the degree of Doctor of Philosophy at the Department of Physics of the University of Cyprus and for the degree of Doctor Rerum Naturalium at the Department of Physics of the University of Wuppertal. It is a product of original work of my own, unless otherwise mentioned through references, notes, or any other statements.

Salvatore Calì

Acknowledgements

I wish to thank all the people who contributed, directly or indirectly, to the realization of this thesis.

First I would like to express my gratitude to Prof. Francesco Knechtli, for giving me the opportunity to study such a beautiful argument for my Ph.D. thesis. His constant support during my stay in Wuppertal has been fundamental for the conclusion of this work.

I am also indebted to Dr. Tomasz Korzec for sharing his knowledge and experience with me and for his infinite patience. Working with him has been a great pleasure and it has certainly improved my programming skills.

I am also very thankful to Prof. Haris Pananagopoulos and Prof. Mike Peardon for their support and help during my visits to Cyprus and Dublin. They created an enjoyable working atmosphere of which I will keep a good memory.

I would like to thank for their strong support my parents, Silvana and Giovanni, all my relatives and my closest friends: Davide, Saverio, Eliana, Marta, Emanuele and Angela.

Special thanks go to Aurora, for all the nice moments shared together for over ten years now. Thank you Aurora, this work is dedicated to you.

Last but not least, I acknowledge support from the European Union's Horizon 2020 research and innovation programme under the Marie Skłodowska-Curie grant agreement No. 642069.

Abstract

At present, many lattice simulations of Quantum Chromodynamics (QCD) are carried out using $N_f = 2+1$ dynamical light quarks (up, down, strange). This setup has so far provided important results and predictions in Particle Physics and can be considered a good approximation of full QCD at energies much below the charm quark mass. However, a more complete setup would include a dynamical charm quark ($N_f = 2+1+1$ QCD), since it eliminates systematic effects due to the "quenching" of the charm quark in $N_f = 2+1$ QCD simulations and also leads to a better understanding of charm physics.

In this thesis we want to compute the loop effects due to a dynamical charm quark in QCD. For this purpose, instead of working in full QCD we study a simplified setup. We simulate two theories: $N_f = 0$ QCD and QCD with $N_f = 2$ dynamical quarks at the charm mass. The dynamical charm effects are extracted from the comparison of $N_f = 0$ and $N_f = 2$ QCD. For the lattice discretization we use the Wilson plaquette gauge action and twisted mass Wilson fermions at maximal twist including a non-perturbatively determined clover term. The absence of light quarks allows us to reach extremely fine lattice spacings (0.017 fm $\lesssim a \lesssim$ 0.049 fm), which are crucial for reliable continuum extrapolations.

We compute in the continuum both quantities without an explicit charm-quark dependence, like the static quark potential and the strong coupling derived from the static force, and quantities with an explicit charm-quark dependence, like charmonium masses and decay constants, the hyperfine splitting and the renormalization group invariant quark mass. For example, for the hyperfine splitting $(m_{J/\psi} - m_{\eta_c})/m_{\eta_c}$, where m_{η_c} and $m_{J/\psi}$ denote the masses of the pseudoscalar meson η_c and vector meson J/ψ respectively, we find that the relative effects of a dynamical charm quark are around 2%. In the strong coupling determined from the static force we clearly see the effects of a dynamical charm as soon as the distance r between the static quarks becomes smaller than 0.13 fm.

Περίληψη

Στις μέρες μας, πολλές προσομοιώσεις της Κβαντικής Χρωμοδυναμικής (ΚΧΔ) στο πλέγμα διεκπεραιώνονται χρησιμοποιώντας $N_f = 2+1$ δυναμικά, ελαφρά κουάρκ (up, down, strange). Αυτή η διάταξη, μέχρι στιγμής παρείχε σημαντικά αποτελέσματα και προβλέψεις στη Σωματιδιακή Φυσική και μπορεί να θεωρηθεί μια καλή προσέγγιση της ολοκληρωμένης θεωρίας της ΚΧΔ σε ενέργειες πολύ πιο κάτω από τη μάζα του charm κουάρκ. Εντούτοις, μία πιο ολοκληρωμένη διάταξη θα περιλάμβανε και ένα δυναμικό charm κουάρκ ($N_f = 2+1+1$ ΚΧΔ), αφού εξαλείφει συστηματικά αποτελέσματα λόγω της "σβεσης" (quenching) του charm κουάρκ σε $N_f = 2+1$ προσομοιώσεις ΚΧΔ, ενώ παράλληλα οδηγεί και σε καλύτερη κατανόηση της φυσικής του charm.

Σε αυτή τη διατριβή, στόχος είναι να υπολογίσουμε τις επιδράσεις βρόχων ως αποτέλεσμα ενός δυναμικού charm κουάρκ στην ΚΧΔ. Για το σκοπό αυτό, αντί να ασχοληθούμε με όλο το φάσμα της ΚΧΔ, μελετούμε μια απλοποιημένη διάταξη. Προσομοιώνουμε δυο θεωρίες: $N_f = 0$ ΚΧΔ και ΚΧΔ με $N_f = 2$ δυναμικά κουάρκ στη μάζα του charm. Τα δυναμικά αποτελέσματα από το charm, απορρέουν από την σύγκριση της $N_f = 0$ και $N_f = 2$ ΚΧΔ. Για τη διακριτοποίηση στο πλέγμα, χρησιμοποιούμε τη δράση πλακέτας Wilson για πεδία βαθμίδος και φερμιόνια Wilson με μάζα twisted σε μέγιστο twist, συμπεριλαμβανομένου ενός μη διαταρακτικού όρου clover. Η απουσία των ελαφρών κουάρκ μας επιτρέπει να πλησιάσουμε πολύ μικρές τιμές της σταθεράς πλέγματος (0.017 fm $\lesssim a \lesssim 0.049$ fm), κάτι το οποίο είναι μείζονος σημασίας για αξιόπιστη παρέκταση στο συνεχές.

Υπολογίζουμε στο συνεχές ποσότητες χωρίς συγκεκριμένη εξάρτηση από το charm κουάρκ, όπως το στατικό δυναμικό κουάρκ και την ισχυρή σταθερά σύζευξης, τα οποία προκύπτουν από την στατική δύναμη, καθώς επίσης και ποσότητες με συγκεκριμένη εξάρτηση από το charm κουάρκ, όπως μάζες charmonium, σταθερές διάσπασης, υπέρλεπτη άρση εκφυλισμού και αναλλοίωτη μάζα των κουάρκ κάτω από την ομάδα επανακανονικοποίησης. Για παράδειγμα, για την υπέρλεπτη άρση εκφυλισμού $(m_{J/\psi} - m_{\eta_c})/m_{\eta_c}$, όπου m_{η_c} και $m_{J/\psi}$ αντιστοιχούν στις μάζες του ψευδοβαθμωτού μεσονίου η_c και του διανυσματικού μεσονίου J/ψ, παρατηρούμε πως τα σχετικά αποτελέσματα ενός δυναμικού charm κουάρκ ανέρχονται γύρω στα 2%. Στη σταθερά ισχυρής σύζευξης, που υπολογίζεται από τη στατική δύναμη, είναι εμφανής η επίδραση ενός δυναμικού charm κουάρκ, όταν η απόσταση r μεταξύ των στατικών κουάρκ είναι λιγότερη από 0.13 fm.

Zusammenfassung

Viele Gittersimulationen der Quanten Chromodynamik (QCD) werden gegenwärtig mit $N_f = 2+1$ dynamischen, leichten Quarks (up, down, strange) durchgeführt. Das kann als gute Näherung der vollen QCD bei Energien weit unterhalb der Charm Quark Masse angesehen werden, die bisher wichtige Ergebnisse und Vorhersagen in der Elementarteilchenphysik geliefert hat. Allerdings würde eine vollständigere Simulation zusätzlich ein dynamisches Charm Quark einbeziehen ($N_f = 2+1+1$ QCD), um systematische Effekte, die durch dessen Vernachlässigung hervorgerufen werden, zu eliminieren, und um Charm Physik besser zu verstehen.

In dieser Dissertation wollen wir die dynamischen Charm Quark Effekte in der QCD berechnen. Zu diesem Zweck arbeiten wir mit einem vereinfachten Modell statt mit der vollen QCD. Wir simulieren zwei Theorien: $N_f = 0$ QCD und QCD mit $N_f = 2$ dynamischen Quarks mit der Masse eines Charm Quarks. Die dynamischen Charm Effekte werden aus dem Vergleich der $N_f = 0$ und der $N_f = 2$ QCD extrahiert. Als Gitter Diskretisierung benutzen wir Wilsons Plaquette Wirkung und Wilson Fermionen mit einem twisted-mass Term, beim maximalen Twist, sowie mit einem clover Term, dessen Koeffizient nichtperturbativ bestimmt wurde. Die Abwesenheit leichter Fermionen erlaubt uns, sehr feine Gitterabstände (0.017 fm $\lesssim a \lesssim 0.049$ fm) zu realisieren, die für zuverlässige Kontinuumsextrapolationen eine entscheidende Rolle spielen.

Im Kontinuum berechnen wir Größen sowohl ohne eine explizite Charm Quark Abhängigkeit, wie das statische Quark Potential, als auch mit einer expliziten Charm Quark Abhängigkeit. Zu letzteren zählen etwa die Massen und Zerfallskonstanten vom Charmonium, die Feinstrukturaufspaltung oder die Renormierungsgruppen invariante Quark Masse. Zum Beispiel finden wir, dass für die Hyperfeinaufspaltung $(m_{J/\psi} - m_{\eta_c})/m_{\eta_c}$, wobei m_{η_c} und $m_{J/\psi}$ die Massen des pseudo-skalaren Mesons η_c und des Vektormesons J/ψ bezeichnen, die Relativen Effekte eines dynamischen Quarks bei etwa 2% liegen. In der über die statische Kraft definierten starken Kopplung sehen wir eindeutige Effekte eines dynamischen Charm Quarks, sobald der Abstand zwischen den statischen Quarks auf unterhalb von 0.13 fm fällt.

Contents

List of Figures

List of Tables

Chapter 1

Introduction

1.1 A brief overview of the Standard Model and QCD

As far as we know today, the fundamental constituents of matter are fermions of spin $1/2$ and can be classified into two types: *quarks* and *leptons*. The interactions among these elementary building blocks of matter are successfully described by the *Standard Model of Particle Physics* (SM). The latter is a relativistic quantum field theory that was developed through 1970-1973 and is the result of the theoretical effort of several scientists[1].

The SM describes three of the four fundamental interactions: the electromagnetic, the weak and the strong interactions. Gravitational forces are not taken into account and can be considered negligible at the typical energies of particle physics, say $E \sim 1$ GeV. As summarized in Figure 1.1 [2], quarks and leptons in turn exist in six different types, called flavors. However, while leptons interact only through the electromagnetic and/or weak interactions, quarks are also subjected to the strong interaction. The SM forces are mediated by *gauge bosons* of spin 1. Such intermediate particles are called gluons (g), photons (γ), W and Z bosons for the strong, electromagnetic and weak interaction respectively. The SM also includes a scalar particle with spin 0, the so-called *Higgs boson*. This particle is an excitation of the Higgs field, which is responsible of the masses of W and Z bosons, quarks and leptons. Its existence was predicted more than 50 years ago [3, 4] and discovered by the experiments at the LHC (Large Hadron Collider) only recently [5, 6].

In this thesis we will concentrate on one of the four fundamental forces, the strong interaction. Its effects are visible at two different scales of distance. On a larger scale (larger than 1 fm) the strong interaction is (indirectly) responsible for binding protons and neutrons into the nuclei, which form the atoms we are made of. On a smaller scale (less than 0.8 fm) it holds quarks together to form composite particles called *hadrons*, to which the proton and the neutron belong. The strong force is described by an $SU(3)$ gauge theory called *Quantum Chromodynamics* (QCD), whose properties will be discussed in more detail in Chapter 2.

Here, we want to recall some of the most important historical steps that led to the formulation of QCD. In the first studies of nuclear reactions it was observed that protons and neutrons, whose masses are almost identical, behave almost identically under the influence of

[1] See Ref. [1] for a detailed historical and theoretical introduction.

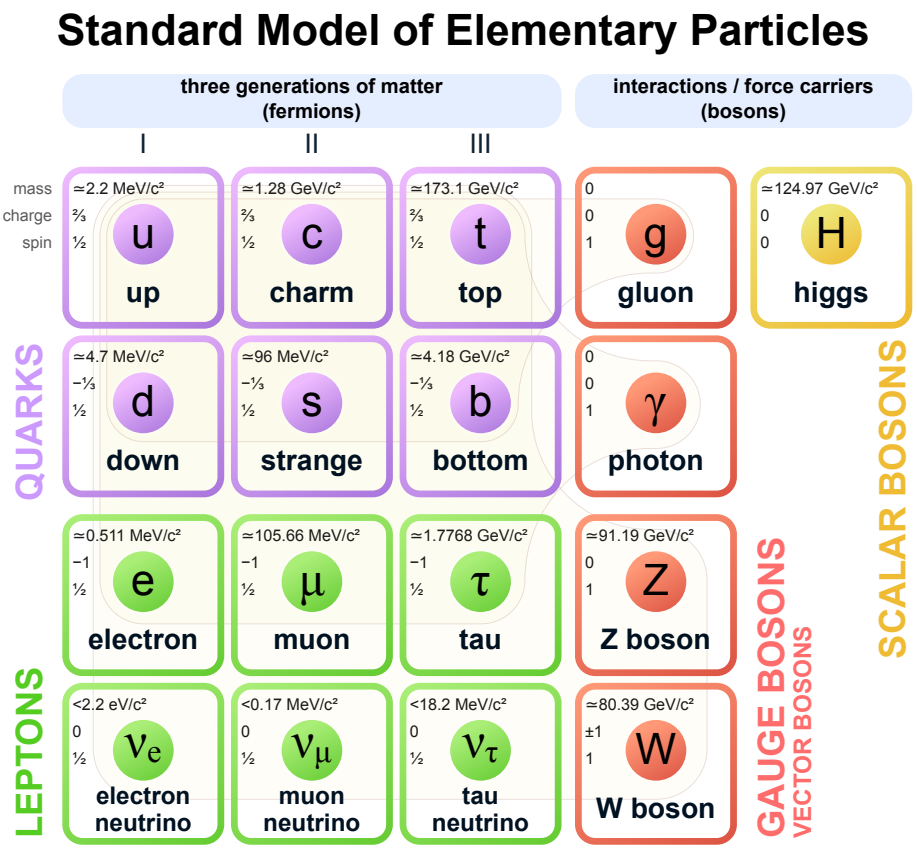

Figure 1.1 Building blocks of matter and force carriers in the Standard Model of Particle Physics. The picture is taken from [2].

the nuclear force within the nucleus, although the proton has a positive electric charge and the neutron is neutral. This induced W. Heisenberg to introduce in 1932 the idea of the isospin invariance of the strong interactions [7]. The mathematical formulation of this symmetry is similar to that of spin, from which the name isospin derives. In this context, the neutron and the proton are seen as a doublet of the symmetry group $SU(2)_I$, where the subscript I stands for isospin. For these reasons protons and neutrons can be grouped together and we often refer to them as *nucleons*. Later, more and more hadrons were discovered and subsequently classified (following Heisenberg's idea) into isospin multiplets of almost mass degenerate particles.

In 1950's and 1960's, the number of known hadrons became huge and to explain the structure of the observed hadron multiplets, M. Gell-Mann and G. Zweig proposed the so-called *quark model* [8, 9]. Their model introduces some fundamental particles of spin $1/2$ that belong to the fundamental representation of the group $SU(3)_f$, where the subscript f stands for flavor. These particles are just the *quarks* introduced above and in the original scenario were thought to exist in three different flavors (up, down, strange)[2]. Following this scheme, it turns out that the hadrons that we observe in Nature are composite particles made of a quark and an antiquark (mesons), or three quarks (baryons) or three antiquarks (antibaryons).

[2]Today we know that the number of flavors is 6, see Figure 1.1.

Although the quark model seemed to explain quite well the structure of the observed hadron multiplets, it gave rise to some paradoxes:

- why do we never observe free quarks?
- why do we not observe other composite particles, like bound states of two or four quarks?
- how can we explain the existence of hadronic states like $|\Delta^{++}, J = 3/2\rangle$, made of three up quarks, which are apparently in contrast with Pauli exclusion principle?

To answer these questions it was assumed that quarks have an extra quantum number [10–12], called *color charge*, that can take three possible values, say *red*, *green* and *blue*. The three color charges represent the triplet of the fundamental representation of the symmetry group $SU(3)_c$, where the subscript c stands for color. On top of this, one assumes that all possible hadron states are singlet under $SU(3)_c$ transformations and therefore we can never observe free quarks, but only composite particles like mesons or baryons. At present, a rigorous proof of the *quark confinement* inside hadrons is still missing, but as we will see in the next chapters, the results of numerical simulations support this assumption.

So far we have summarized the logical steps that led in the early 1970's to the birth of the modern theory of strong interactions, which is today known as QCD. However, it is clear that to understand the properties of hadrons and quark confinement we need to know the QCD behavior at distances larger than the size of a proton (around 1 fm), i.e. at low energies. In this context, one of the main obstacles originates from the running of the coupling α_s of QCD. For non-abelian gauge theories like QCD, it is known that α_s becomes small only at very short distances (below 0.1 fm) [13, 14] and therefore perturbative methods fail when we want to investigate hadronic properties involving long-distance physics.

1.2 Introduction to this work

The failure of perturbation theory in the low energy sector led to the search for alternative tools to study hadron properties and prove confinement. In 1974 Wilson [15] proposed a formulation of QCD on a Euclidean lattice. Nowadays, the *lattice* QCD approach represents the standard method to study QCD in the non-perturbative regime and is the method that has also been used in this thesis. In this approach, the theory is discretized in a hypercubic grid with Euclidean metric and the expectation values of the observables of interest are computed numerically via Monte Carlo methods.

As we already mentioned, QCD encompasses six flavors of quarks. However, since quark masses cover a large range of values that can differ by several orders of magnitude, lattice QCD simulations often include only two, three or at most four flavors. Moreover, exact isospin symmetry is usually assumed and thus up and down quarks are considered mass degenerate. Lattice QCD simulations with just $N_f = 2 + 1$ dynamical light quarks (up, down and strange) are quite common, since adding a dynamical charm quark complicates the parameter tuning and may result in large cutoff effects, because of the heavy mass of the charm quark. Due to

the decoupling [16, 17] of the charm quark, this setup is sufficient for the study of low energy physics with energies far below the charm threshold. However when it is used to study charm physics, neglecting the effects of heavy quarks in the *sea* (*loop effects*) may introduce large uncontrolled systematic uncertainties.

To evaluate how big these effects might be, we compute several physical observables in $N_f = 0$ QCD and $N_f = 2$ QCD, where the second theory contains two heavy quarks, with the mass of a charm quark. This setup, without the light quarks, allows us to isolate the charm loop effects to a very high precision. Their size is extracted through a comparison in the continuum limit of the results obtained in $N_f = 0$ QCD and $N_f = 2$ QCD. The quantities we focus on are: charmonium masses and decay constants, the hyperfine splitting, the renormalization group invariant quark mass, the static quark potential and the strong coupling derived from the static force.

The thesis is organized as follows. In Chapter 2 we review the basics of continuum QCD, chiral symmetries and the effective theory of decoupling. Chapter 3 contains a short introduction to the lattice formulation of QCD and the description of our model of QCD to study charm physics. In Chapter 4 we introduce the observables under study in this thesis and explain the numerical methods that have been used to measure them. In Chapters 5 and 6 we present the results of our investigation. Through a comparison of $N_f = 0$ QCD and QCD with $N_f = 2$ degenerate charm quarks, we compute in the continuum the effects of a dynamical charm quark on the observables mentioned above. Finally, in Chapter 7 we summarize the most relevant results of this thesis and discuss interesting new studies that can follow from our work.

Chapter 2

Quantum Chromodynamics

2.1 Continuum QCD

Quantum Chromodynamics (QCD) is the quantum field theory through which we describe the strong interactions. It is based on the non-abelian color group $SU(3)_c$, where the quark fields represent the fundamental dynamical objects. An important feature of QCD is the so-called *quark confinement*: quarks are never seen in isolation, but they are confined within hadrons. The latter are usually divided into two groups: mesons (bound states made of a quark and an antiquark) and baryons (bound states made of three quarks). Quarks exist in six different flavors (up, down, strange, charm, bottom, top) and are spin-$\frac{1}{2}$ particles. Their masses and electric charges[1] are listed in Table 2.1.

Generation	Flavor	Mass	Q
I	up (u)	$m_u = 2.2^{+0.5}_{-0.4}$ MeV	2/3
	down (d)	$m_d = 4.7^{+0.5}_{-0.3}$ MeV	-1/3
II	charm (c)	$m_c = 1.275^{+0.025}_{-0.035}$ GeV	2/3
	strange (s)	$m_s = 95^{+9}_{-3}$ MeV	-1/3
III	top (t)	$m_t = 173 \pm 4$ GeV	2/3
	bottom (b)	$m_b = 4.18^{+0.04}_{-0.03}$ GeV	-1/3

Table 2.1 Quark masses and electric charges (Q). Masses are given in the $\overline{\text{MS}}$ scheme (see Ref. [18] for further details). The electric charge is a fraction of the elementary charge e (either $-1/3$ or $2/3$, depending on flavor).

Every quark flavor owns an extra index, related to the *color charge*, that can assume one of three possible values (which are usually called red, green, and blue). Thus, a generic quark field at the space-time position x can be described by a Dirac 4-spinor $\psi^f_{\alpha c}(x)$, where f denotes its flavor, $\alpha = 1,2,3,4$ is the Dirac index and $c = 1,2,3$ is the color index. Quark

[1] In this thesis we make use of natural units, which means that the reduced Planck constant $\hbar$, the speed of light c and the vacuum permittivity ε_0 are set to 1: $\hbar = c = \varepsilon_0 = 1$. Therefore masses can be expressed in eV (or its multiples) and the elementary charge e is a pure number.

fields are in the fundamental representation of the color gauge group $SU(3)$, therefore their transformation law under the group $SU(3)$ is[2]

$$\psi^f_{\alpha c} \to U_{cc'}(x)\psi^f_{\alpha c'}, \quad U(x) = e^{i\theta^i(x)T^i}, \tag{2.1}$$

where $\theta^i(x)$ are some local parameters and T^i ($i = 1, \cdots, 8$) represent the traceless hermitian generators of the $SU(3)$ group in the fundamental representation. We recall that these generators satisfy the commutation rules

$$[T^i, T^i] = if^{ijk}T^k \tag{2.2}$$

and that their normalization is given by

$$\mathrm{Tr}[T^iT^j] = \frac{1}{2}\delta_{ij}. \tag{2.3}$$

In Eqs. (2.2) and (2.3) f^{ijk} are the structure constants of the $SU(3)$ group, δ_{ij} is the Kronecker delta and Tr[ ] denotes the usual matrix trace. The Lagrangian density of QCD with N_f flavors reads

$$\mathcal{L}_{QCD}(x) = \mathcal{L}_F(x) + \mathcal{L}_G(x), \tag{2.4}$$

with

$$\mathcal{L}_F(x) = \sum_{f=1}^{N_f} \bar{\psi}^f(x)\left(i\gamma^\mu D_\mu(x) - m_0^f\right)\psi^f(x), \tag{2.5}$$

$$\mathcal{L}_G(x) = -\frac{1}{2}\mathrm{Tr}\left[F_{\mu\nu}(x)F^{\mu\nu}(x)\right]. \tag{2.6}$$

$\mathcal{L}_F$ and $\mathcal{L}_G$ represent the fermionic and purely gluonic part of the QCD Lagrangian (2.4). In Eqs. (2.4), (2.5) and (2.6), γ_μ denote the Dirac gamma matrices and D_μ is the so-called *covariant derivative*

$$D_\mu(x) = \partial_\mu + ig_0A_\mu(x), \tag{2.7}$$

where g_0 is the bare coupling of QCD and A_μ is the (matrix) gauge field, defined as

$$A_\mu(x) = \sum_{a=1}^{8} A^a_\mu(x)T^a. \tag{2.8}$$

The bare quark masses m_0^f differ depending on flavor and $F_{\mu\nu}$ denotes the field strength tensor, which is defined as

$$[D_\mu, D_\nu] \equiv ig_0F_{\mu\nu} \quad \Rightarrow \quad F_{\mu\nu} \equiv \partial_\mu A_\nu - \partial_\nu A_\mu + ig_0\left[A_\mu, A_\nu\right], \tag{2.9}$$

[2]Except where otherwise stated, we always imply summation over repeated indices.

or in terms of the gluon fields A_μ^a as

$$F_{\mu\nu} = F_{\mu\nu}^a T^a, \quad F_{\mu\nu}^a = \partial_\mu A_\nu^a - \partial_\nu A_\mu^a - g_0 f^{abc} A_\mu^b A_\nu^c. \tag{2.10}$$

To guarantee that the QCD Lagrangian (2.4) is invariant under an $SU(3)$ transformation (2.1) on the quark fields, the fields A_μ and $F_{\mu\nu}$ have to satisfy

$$A_\mu \xrightarrow[SU(3)]{} U A_\mu U^\dagger + \frac{i}{g_0}\left(\partial_\mu U\right) U^\dagger, \tag{2.11}$$

$$F_{\mu\nu} \xrightarrow[SU(3)]{} U F_{\mu\nu} U^\dagger. \tag{2.12}$$

From the structure of the Lagrangian (2.4), it is easy to see that in QCD there are three basic interaction terms (vertices): a quark-antiquark-gluon vertex (similar to the QED one), but also a 3-gluon vertex and a 4-gluon vertex (that come from the particular form of $F_{\mu\nu}^a$, see Eq. (2.10), in $SU(N)$ gauge theories). The construction of gauge theories based on $SU(N)$ groups dates back to the famous paper of C. N. Yang and R. Mills in 1954 [19] and we refer to standard quantum field theory books [20, 21] for further details.

By using Feynman's path integral formalism, the vacuum expectation value of a generic observable $\mathcal{O}$ in QCD can be written as

$$\langle \mathcal{O} \rangle = \frac{\int D\bar{\psi} D\psi DA\, \mathcal{O}(\psi, \bar{\psi}, A) e^{iS}}{\int D\bar{\psi} D\psi DA\, e^{iS}}, \tag{2.13}$$

where the action S is given by (see Eqs.(2.5) and (2.6))

$$S = \int d^4x (\mathcal{L}_F + \mathcal{L}_G) \tag{2.14}$$

and the symbols $D\phi$ denote the integration measure over all the configurations of a field $\phi(x)$ with fixed boundary conditions.

2.1.1 Renormalization

In quantum field theories like QCD, one is usually interested in physical observables that are extracted from suitable correlation functions. In perturbation theory the strategy is to expand such correlation functions in powers of the gauge coupling around the free theory. This requires the evaluation of Feynman diagrams, whose number of loops increases with the order of the expansion in the coupling constant. In the computation of Feynman diagrams with one or more loops, one has to deal with ultraviolet divergences when integrating over the momenta of virtual particles inside a loop. To overcome this problem, a *regulator* is usually introduced to make the contribution of loop diagrams finite. In this way, the fields and the parameters that appear in the Lagrangian (2.4) are not physical observables, but they should be seen as *bare* quantities that depend on the regulator. Such dependence must be chosen so that divergences in physical quantities can be removed and it is usually parameterized in

terms of renormalization factors Z and renormalized fields and parameters as

$$A_\mu = Z_A^{1/2} A_{R\mu}, \quad \psi = Z_\psi^{1/2} \psi_R, \quad g_0 = Z_g g_R, \quad m_0 = Z_m m_R, \tag{2.15}$$

where we have introduced the subscript R to denote the renormalized objects. This procedure allows to write the QCD Lagrangian as

$$\mathcal{L}_{QCD} = \mathcal{L}_{R,QCD} + \mathcal{L}_{ct}. \tag{2.16}$$

In Eq. (2.16), $\mathcal{L}_{R,QCD}$ has the same form as $\mathcal{L}_{QCD}$, where the renormalized objects replace the bare ones, whilst $\mathcal{L}_{ct}$ represents a Lagrangian of suitable *counter-terms*, depending both on the Z factors and renormalized fields. By appropriate choice of the counter-terms, divergences in physical quantities can be eliminated and amplitudes expressed by renormalized fields and parameters are finite when the regulator is removed.

A natural choice for the regulator would be to impose a cutoff Λ on the integrated momentum. However, in practice it is better to use other regularization schemes, because the introduction of a cutoff Λ on the momenta may break both $SU(3)$ and Lorentz symmetries. Therefore, we consider here another approach, that has the advantage of preserving these symmetries and it is known as dimensional regularization [22]. It is based on the following idea: a divergent integral in the 4-dimensional space-time can be formally replaced by an identical integral whose contribution is finite in a D-dimensional space-time. Once computing it in D dimensions, it is possible to approach the limit $D \to 4$ through an analytical continuation. The singularities for $D \to 4$ are usually of the type $1/\varepsilon$, with $\varepsilon = (4-D)/2$.

When switching to a D-dimensional space, it is also important to study how the dimensions (in mass) of fields and parameters change. In natural units $\hbar = c = \varepsilon_0 = 1$ the action $S = \int d^D x \mathcal{L}_{QCD}$ is dimensionless, therefore $\dim[\mathcal{L}_{QCD}] = D$. Looking at the kinetic terms, it is then easy to show that $\dim[A_\mu] = (D-2)/2$ and $\dim[\psi] = (D-1)/2$. Therefore, the interaction term $\sim g_0 \bar{\psi} A \psi$ fixes the dimension of the coupling at $dim[g_0] = (4-D)/2 = \varepsilon$, which means that g_0 is not dimensionless for $D \neq 4$. To keep g_R dimensionless a mass scale μ (called *renormalization scale*) is introduced and g_R is replaced by

$$g_R \to \mu^\varepsilon g_R. \tag{2.17}$$

This means that Feynman diagrams have an explicit dependence on the mass scale μ. In the minimal subtraction scheme (often shortened to MS-scheme) [22] the Z-factors are chosen such that only $(1/\varepsilon)$-poles in divergent quantities are removed. Normally, such singularities appear together with the finite term

$$-\gamma_E + \log(4\pi), \tag{2.18}$$

where $\gamma_E \approx 0.577$ is the Euler–Mascheroni constant. In the popular modified minimal subtraction scheme (often shortened to $\overline{\text{MS}}$-scheme) [23], the Z-factors cancel also the finite term (2.18).

2.1.2 Lambda parameter and RGI mass

Let us consider now a physical observable depending on the renormalized mass and coupling and possibly on μ:

$$\mathcal{O} = \mathcal{O}(g_R(\mu), m_R(\mu), \mu). \tag{2.19}$$

Its physical value should be renormalization scale invariant, as μ is only an energy scale that has been introduced in the regularization prescription to define the coupling in $D = 4 - 2\varepsilon$ dimensions. Therefore, we expect

$$\mu \frac{d}{d\mu} \mathcal{O}(g_R(\mu), m_R(\mu), \mu) = 0. \tag{2.20}$$

Expanding the total derivative in (2.20), we obtain the well-known Callan–Symanzik equation [24, 25]

$$\left[\mu \frac{\partial}{\partial \mu} + \beta(g_R) \frac{\partial}{\partial g_R} + \tau(g_R) m_R \frac{\partial}{\partial m_R} \right] \mathcal{O}(g_R(\mu), m_R(\mu), \mu) = 0, \tag{2.21}$$

where

$$\beta(g_R) = \mu \frac{\partial g_R}{\partial \mu}, \tag{2.22}$$

$$\tau(g_R) = \frac{\mu}{m_R} \frac{\partial m_R}{\partial \mu}. \tag{2.23}$$

We consider here only mass independent renormalization schemes, where the renormalization conditions are imposed at zero quark mass (like the MS- and $\overline{\text{MS}}$-schemes). The β-function describes the running of the coupling and its perturbative expansion for small values of the renormalized coupling is given by

$$\beta(g_R) \underset{g_R \to 0}{=} -b_0 g_R^3 - b_1 g_R^5 + O(g_R^7). \tag{2.24}$$

The first two coefficients b_0 and b_1 are universal for mass-independent renormalization schemes and their value is [26, 27]

$$b_0 = \frac{1}{(4\pi)^2} \left(11 - \frac{2}{3} N_f \right), \quad b_1 = \frac{1}{(4\pi)^4} \left(102 - \frac{38}{3} N_f \right). \tag{2.25}$$

Instead, the other coefficients of the expansion (2.24) depend on the renormalization scheme. In the $\overline{\text{MS}}$-scheme the β-function is known up to five loops and we refer to [28–33] for the values of $b_2^{\overline{\text{MS}}}$, $b_3^{\overline{\text{MS}}}$ and $b_4^{\overline{\text{MS}}}$. In a similar way, the running of a quark mass is described by the τ-function, whose perturbative expansion is

$$\tau(g_R) \underset{g_R \to 0}{=} -d_0 g_R^2 - d_1 g_R^4 + O(g_R^6), \qquad d_0 = \frac{8}{(4\pi)^2}. \tag{2.26}$$

For this expansion, only d_0 is a universal coefficient, whilst the higher order coefficients are scheme-dependent (see Ref. [34] for results in the $\overline{\text{MS}}$-scheme up to four loops).

By solving the first order differential equations (2.22) and (2.23), one finds two integration constants that are usually called Λ parameter and renormalization group invariant (RGI) mass M. Their expressions are

$$\Lambda = \mu \left(b_0 g_R^2\right)^{-\frac{b_1}{2b_0^2}} e^{-\frac{1}{2b_0 g_R^2}} \exp\left\{-\int_0^{g_R} dx \left[\frac{1}{\beta(x)} + \frac{1}{b_0 x^3} - \frac{b_1}{b_0^2 x}\right]\right\}, \tag{2.27}$$

$$M = m_R (2b_0 g_R^2)^{-\frac{d_0}{2b_0}} \exp\left\{-\int_0^{g_R} dx \left[\frac{\tau(x)}{\beta(x)} - \frac{d_0}{b_0 x}\right]\right\}. \tag{2.28}$$

Both Λ and M are renormalization group invariant quantities, i.e. they do not depend on the renormalization scale μ. The RGI mass M is also scheme independent [35], whilst the value of Λ depends on the renormalization scheme. However, if g_R and g_R' denote two different renormalization schemes related by

$$g_R' = g_R + c_1 g_R^3 + O(g_R^5), \tag{2.29}$$

the corresponding Lambda parameters Λ and Λ' satisfy the exact one-loop relation [35]

$$\frac{\Lambda'}{\Lambda} = \exp\left(\frac{c_1}{b_0}\right). \tag{2.30}$$

2.1.3 The running of the coupling

From (2.27), it is possible to extract the *strong coupling constant*

$$\alpha_s \equiv \frac{g_R^2(\mu)}{4\pi} \tag{2.31}$$

in a given normalization scheme. In perturbation theory, a compact (but only asymptotic) solution exists at one-loop order and it is given by

$$\alpha_s|_{1\text{ loop}} \underset{\mu\to\infty}{\approx} \frac{1}{4\pi b_0 \log\left(\frac{\mu^2}{\Lambda^2}\right)}. \tag{2.32}$$

Note that Eq. (2.32) is useful to understand the high energy behavior of g_R, but it cannot be used to determine Λ properly, because at least the two-loop β-function is needed[3]. Already at two-loop order, to describe α_s as a function of μ we need to use more complicated formulae or try to solve Eq. (2.27) numerically. For instance, at high energies the asymptotic behavior of the two-loop strong coupling is

$$\alpha_s|_{2\text{ loop}} = \frac{1}{4\pi b_0 t} - \frac{b_1 \log(t)}{4\pi b_0^3 t^2} + O(t^{-3}(\log(t))^2), \quad t = \log\left(\frac{\mu^2}{\Lambda^2}\right), \tag{2.33}$$

whose plot is shown in Figure 2.1.

As can be seen, α_s decreases with increasing energy scale and approaches zero in the limit $\mu \to \infty$. This property, known in the literature as *asymptotic freedom* [13, 14], tells

[3] See Ref. [36] for further details.

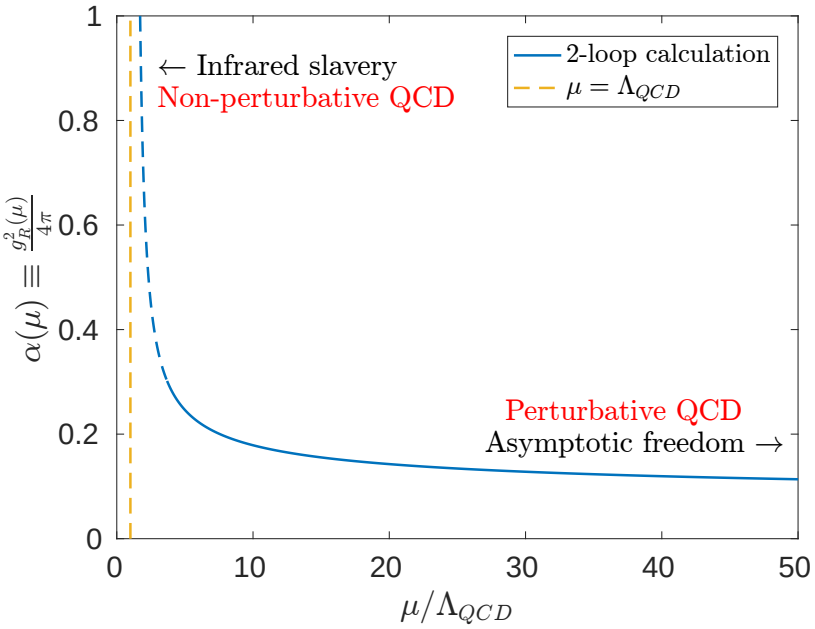

Figure 2.1 Strong coupling constant α_s at two-loop order. This example refers to $N_f = 0$ QCD. For $\alpha \gtrsim 0.3$ we plot the curve only with a dashed line, as in this region perturbation theory fails and the predictions can no longer be considered reliable.

us that perturbation theory works extremely well at high energies μ ($g_R \to 0$) and quarks and gluons almost behave as free particles. When $N_f \leq 16$ ($N_f = 6$ in the real world) the coefficient b_0 of the β-function is positive and this determines the logarithmic decay of the strong coupling α_s[4]. On the other hand, with decreasing energy α_s increases and becomes[5] $\alpha_s \sim O(1)$ when μ approaches Λ, whose physical value is around[6] 300 MeV. Therefore, at energy scales μ comparable to Λ or smaller, perturbation theory is no longer reliable and we need to use non-perturbative methods to understand QCD properties at low energies. The non-perturbative method which has been used in this thesis in known as lattice QCD and it will be presented in Chapter 3. For the time being, we just anticipate that the method mainly consists in replacing the continuum space-time with a Euclidean four-dimensional grid of finite size and it allows one to evaluate the expectation values of physical observables through a multidimensional integral, instead of using the continuum path integrals.

2.2 Flavor symmetries of the QCD Lagrangian

Apart from local gauge symmetry which was already discussed, $\mathcal{L}_{QCD}$ (2.4) is also invariant under Lorentz transformations and it preserves the discrete symmetries of *charge conjugation* (C), *parity* (P) and *time reversal* (T). The latter are exact symmetries, but $\mathcal{L}_{QCD}$ has also an approximate global $U(2) \otimes U(2)$ flavor symmetry, which becomes exact in the limit of massless flavors. Before going into details, we start with a brief summary at the classical level

[4] For $N_f > 16$, b_0 becomes negative and we would observe an opposite behavior: $g_R \to 0$ when $\mu < \Lambda$, as in the case of QED.

[5] This phenomenon is often called *infrared slavery*.

[6] We refer to [37] for a table of the Λ parameters in the $\overline{\text{MS}}$ scheme depending on the number of flavors N_f.

of internal symmetries, namely symmetries that act only on the fields and do not change the coordinates.

2.2.1 Summary at the classical level

Let us consider a Lagrangian $\mathcal{L}$ that depends on the fields ϕ_i and a symmetry group G that transforms ϕ_i according to

$$G : \phi_i \to \phi_i' + \delta\phi_i = \phi_i' + \omega_a \delta_a \phi_i, \tag{2.34}$$

where ω_a are continuous parameters. Then, the *Noether current* associated with the symmetry G is

$$J_\mu^a(x) = -\sum_i \frac{\partial \mathcal{L}}{\partial(\partial^\mu \phi_i)} \delta_a \phi_i. \tag{2.35}$$

At classical level there are two different cases:

1. If $G : \mathcal{L} \to \mathcal{L}' = \mathcal{L}$, then
$$\partial_\mu J_a^\mu(x) = 0. \tag{2.36}$$
2. If $G : \mathcal{L} \to \mathcal{L}' = \mathcal{L} + \delta\mathcal{L}$, with $\delta\mathcal{L} = \omega_a \delta_a \mathcal{L}$, then
$$\partial_\mu J_a^\mu(x) = -\delta_a \mathcal{L}. \tag{2.37}$$

For a conserved current (2.36) localized in space, one can also define a charge Q_a

$$Q_a = \int d^3x J_a^0(x) \tag{2.38}$$

that is also conserved, because

$$\frac{dQ_a}{dt} = \int_V d^3x \vec{\nabla} \cdot \vec{J}^a = \oint_{\partial V} d\vec{s} \cdot \vec{J}^a = 0, \quad \vec{J}^a = 0 \text{ on } \partial V. \tag{2.39}$$

2.2.2 Chiral symmetries

Now, let us go back to the QCD Lagrangian (2.4) and consider the fermion part $\mathcal{L}_F$. For convenience, it is better to rewrite it as

$$\mathcal{L}_F = \mathcal{L}_F^{N_l} + \mathcal{L}_F^{N_f - N_l}, \tag{2.40}$$

where $\mathcal{L}_F^{N_l}$ is the part of $\mathcal{L}_F$ which describes N_l light quarks, while $\mathcal{L}_F^{N_f-N_l}$ describes the remaining $N_f - N_l$ quark fields. Let us focus on $\mathcal{L}_F^{N_l}$ which, using matrix notation, reads

$$\mathcal{L}_F^{N_l} = \bar{\psi}(i\gamma^\mu D_\mu - M)\psi, \tag{2.41}$$

with

$$\psi = \begin{pmatrix} \psi_1 \\ \vdots \\ \psi_{N_l} \end{pmatrix}, \quad \bar{\psi} = \begin{pmatrix} \bar{\psi}_1, \cdots, \bar{\psi}_{N_l} \end{pmatrix}, \quad M = \begin{pmatrix} m_1 & & \\ & \ddots & \\ & & m_{N_l} \end{pmatrix}. \tag{2.42}$$

In the degenerate case $m_1 = m_2 \cdots = m_{N_l}$, it is easy to show that $\mathcal{L}_f^{N_l}$ is invariant under transformations of the unitary group $U(N_l)$:

$$U(N_l) : \begin{cases} \psi \to U\psi, \\ \psi^\dagger \to \psi^\dagger U^\dagger \end{cases}, \quad U \in U(N_l). \tag{2.43}$$

Usually, one assumes $N_l = 2$ (up, down) degenerate quarks, because the quark masses m_u, m_d have a similar value (see Table (2.1))[7]. However, since m_u, m_d are much smaller than the Λ parameter (2.27), which represents the typical energy scales of QCD, it is also worthwhile studying the symmetries of $\mathcal{L}_f^{N_l}$ in the case of N_l degenerate massless quarks ($m_1, \ldots, m_{N_l} = 0$), also called *chiral limit*. To this aim, let us first define the right- and left-handed fermion fields

$$\begin{cases} \psi_L = P_L\psi, \quad \bar{\psi}_L = \bar{\psi}P_R \\ \psi_R = P_R\psi, \quad \bar{\psi}_R = \bar{\psi}P_L \end{cases}, \quad \text{with } P_{R,L} \equiv \frac{1 \mp \gamma^5}{2}, \tag{2.44}$$

where we use the chiral representation of the matrix γ^5

$$\gamma^5 \equiv -i\gamma^0\gamma^1\gamma^2\gamma^3 = \begin{pmatrix} -\mathbb{1}_2 & 0 \\ 0 & \mathbb{1}_2 \end{pmatrix}, \tag{2.45}$$

which satisfies the properties

$$(\gamma^5)^2 = \mathbb{1}, \quad (\gamma^5)^\dagger = \gamma^5, \quad \{\gamma^5, \gamma^\mu\} = 0. \tag{2.46}$$

$P_{R,L}$ are called right- and left-handed projectors and they obey the following relations

$$\begin{aligned} &P_R^2 = P_R, \quad P_L^2 = P_L, \quad P_R P_L = P_L P_R = 0, \quad P_R + P_L = \mathbb{1}, \\ &\gamma^\mu P_L = P_R \gamma^\mu, \quad \gamma^\mu P_R = P_L \gamma^\mu. \end{aligned} \tag{2.47}$$

By using Eqs. (2.44) and (2.47), it is convenient to rewrite $\mathcal{L}_F^{N_l}$ as follows

$$\begin{aligned} \mathcal{L}_F^{N_l} &= \bar{\psi}(P_R + P_L)(i\gamma^\mu D_\mu - M)(P_R + P_L)\psi \\ &= \bar{\psi}P_R(i\gamma^\mu D_\mu)P_L\psi + \bar{\psi}P_L(i\gamma^\mu D_\mu)P_R\psi - \bar{\psi}P_R M P_R\psi - \bar{\psi}P_L M P_L\psi \\ &= \bar{\psi}_L(i\gamma^\mu D_\mu)\psi_L + \bar{\psi}_R(i\gamma^\mu D_\mu)\psi_R - \bar{\psi}_L M\psi_R - \bar{\psi}_R M\psi_L. \end{aligned} \tag{2.48}$$

From (2.48) we immediately realize that unlike the kinetic term $\bar{\psi}(i\gamma^\mu D_\mu)\psi$, the mass term $\bar{\psi}M\psi$ mixes right and left components of the quark fields. Therefore, in the massless case

[7] Sometimes also $N_l = 3$ (up, down, strange) is acceptable, even if this is a worse approximation.

$m_1,\dots,m_{N_l}=0$, the Lagrangian $\mathcal{L}_F^{N_l}$ is invariant under transformations of the group

$$U(N_l)_L\otimes U(N_l)_R:\begin{cases}\psi_L\to U_L\psi_L\\ \psi_R\to U_R\psi_R\end{cases},\quad U_R,U_L\in U(N_l). \tag{2.49}$$

The symmetry group (2.49) is equivalent to

$$G=U(1)_L\otimes U(1)_R\otimes SU(N_l)_L\otimes SU(N_l)_R. \tag{2.50}$$

Notice that this is true at the algebra level only, but it is sufficient for our purposes.

2.2.3 Noether currents associated with the chiral symmetry group

The transformation of a fermion field ψ (2.42) under the group $U(1)_L\otimes U(1)_R$ can be written as

$$U(1)_L:\begin{cases}\psi_L\to\psi_L'=e^{i\alpha_L}\psi_L\\ \psi_R\to\psi_R\end{cases},\quad U(1)_R:\begin{cases}\psi_L\to\psi_L\\ \psi_R\to\psi_R'=e^{i\alpha_R}\psi_R\end{cases}, \tag{2.51}$$

where α_L and α_R are two different phases. A vector transformation $U(1)_V$ corresponds to the case $\alpha_L=\alpha_R\equiv\alpha$, while an axial transformation $U(1)_A$ corresponds to the case $\alpha_L=-\alpha_R\equiv\beta$:

$$U(1)_V:\begin{cases}\psi_L\to\psi_L'=e^{i\alpha}\psi_L\\ \psi_R\to\psi_R'=e^{i\alpha}\psi_R\end{cases},\quad U(1)_A:\begin{cases}\psi_L\to\psi_L'=e^{i\beta}\psi_L\\ \psi_R\to\psi_R'=e^{-i\beta}\psi_R\end{cases}. \tag{2.52}$$

Therefore, if we consider a transformation of the group $U(1)_V\otimes U(1)_A$ with parameters α and β, this is equivalent to a transformation $U(1)_L\otimes U(1)_R$ with parameters $\theta_L\equiv\alpha+\beta$ and $\theta_R\equiv\alpha-\beta$. We can use a similar argument for the group $SU(N_l)_L\otimes SU(N_l)_R$. First, let us write its action on the fermion field ψ

$$SU(N_l)_L\otimes SU(N_l)_R:\begin{cases}\psi_L\to\psi_L'=V_L\psi_L\\ \psi_R\to\psi_R'=V_R\psi_R\end{cases},\quad V_L,V_R\in SU(N_l). \tag{2.53}$$

It is possible to show that a transformation of the group $SU(N_l)_L\otimes SU(N_l)_R$ can be written as a combination of a vector (for which $V_L=V_R=V$) and axial (for which $V_L=V_R^\dagger=A$) transformation, that we call $SU(N_l)_V$ and $SU(N_l)_A$ respectively. Indeed,

$$SU(N_l)_V\otimes SU(N_l)_A:\begin{cases}\psi_L\to\psi_L'=AV\psi_L\\ \psi_R\to\psi_R'=A^\dagger V\psi_R\end{cases}, \tag{2.54}$$

which is formally equivalent to (2.53) if we choose

$$\begin{cases} A = (V_L V_R^\dagger)^{\frac{1}{2}} \\ V = (V_L V_R^\dagger)^{\frac{1}{2}} V_R \end{cases} . \tag{2.55}$$

Thus, from now on we will refer to the chiral group (2.50) by considering

$$G = U(1)_V \otimes U(1)_A \otimes SU(N_l)_V \otimes SU(N_l)_A. \tag{2.56}$$

Again, this is only true at the level of the algebra. One way to see this is that there is multi-valuedness in the square roots of (2.55). To extract the Noether currents associated to this group, it is more convenient to express the transformations in terms of the field ψ, instead of using the right- and left-handed components ψ_L and ψ_R

$$\begin{cases} U(1)_V : \psi \to \psi' = e^{i\alpha}\psi \\ U(1)_A : \psi \to \psi' = e^{i\beta}\psi_L + e^{-i\beta}\psi_R = e^{i\beta\gamma^5}\psi \\ SU(N_l)_V : \psi \to \psi' = e^{i\theta^a T^a}\psi \\ SU(N_l)_A : \psi \to \psi' = e^{i\theta^a T^a}\psi_L + e^{-i\theta^a T^a}\psi_R = e^{i\theta^a T^a \gamma^5}\psi \end{cases} , \tag{2.57}$$

where we used the properties $\gamma^5\psi_L = \psi_L$ and $\gamma^5\psi_R = -\psi_R$. Therefore, the corresponding Noether currents (see Eq. (2.35)) read

$$\begin{cases} U(1)_V : V^\mu = \bar{\psi}\gamma^\mu\psi \\ U(1)_A : A^\mu = \bar{\psi}\gamma^\mu\gamma^5\psi \\ SU(N_l)_V : V_a^\mu = \bar{\psi}\gamma^\mu T_a\psi \\ SU(N_l)_A : A_a^\mu = \bar{\psi}\gamma^\mu\gamma^5 T_a\psi \end{cases} \tag{2.58}$$

and they are all classically conserved in the limit $m_1 = \cdots = m_{N_l} = 0$. However, when dealing with massive quarks the mass term of (2.41) breaks the chiral symmetry explicitly, leading to a variation of $\mathcal{L}_F^{N_l}$ of the form $\delta\mathcal{L}_F^{N_l} = \omega_a\delta_a\mathcal{L}_F^{N_l}$. Thus, because of Eq. (2.37) the four-divergences of the currents (2.58) depend on the quark masses as described below

$$\begin{cases} \partial_\mu V^\mu = 0 \\ \partial_\mu A^\mu = 2i\bar{\psi}\gamma^5 M\psi \\ \partial_\mu V_a^\mu = i\bar{\psi}[M, T_a]\psi \\ \partial_\mu A_a^\mu = i\bar{\psi}\{M, T_a\}\gamma^5\psi \end{cases} . \tag{2.59}$$

From the equations in (2.59), also known as *Ward identities*, we can conclude that:

- The symmetry $U(1)_V$ is always conserved, even in the case of massive quarks and its conserved charge corresponds to the baryon number;

- the symmetry $SU(N_l)_V$ is conserved either for vanishing quark masses or for mass degenerate quarks. For this reason the expression $\partial_\mu V_a^\mu = i\bar{\psi}[M,T_a]\psi$ is known as partially conserved vector current (PCVC) relation. The case $N_l = 2$ ($m_u = m_d$) is called isospin symmetry, while the case $N_l = 3$ ($m_u = m_d = m_s$) is called Gell-Mann symmetry.

- the symmetry $SU(N_l)_A$ is conserved only in the case of vanishing quark masses and we usually refer to the expression $\partial_\mu A_a^\mu = i\bar{\psi}\{M,T_a\}\gamma^5\psi$ as the partially conserved axial current (PCAC) relation.

As concerns the symmetry $U(1)_A$, it is conserved for massless quarks at classical level. However, this result is no longer true when considering quantum effects. In particular, at quantum level this symmetry is affected by the so-called *anomaly* [38–41]. This means that the second expression in (2.59) must be corrected as follows:

$$\partial_\mu A^\mu = 2i\bar{\psi}\gamma^5 M\psi + 2N_l q, \tag{2.60}$$

with

$$q \equiv \frac{g_0^2}{64\pi^2}\varepsilon^{\mu\nu\rho\sigma}F^a_{\mu\nu}F^a_{\rho\sigma}. \tag{2.61}$$

The quantity q is called *topological charge density*, while the integral

$$Q = \int d^4x q(x) \tag{2.62}$$

is called *topological charge*. The axial anomaly plays a very important role in the *Witten-Veneziano mechanism* [42, 43] to explain the large mass of the meson η'.

2.2.4 Spontaneous symmetry breaking

We conclude this section introducing one of the most important features of the chiral symmetry group, namely its *spontaneous breaking*.

From what we have seen so far, we would expect the group $U(1)_V \otimes SU(2)_V \otimes SU(2)_A$ to be an approximate symmetry of QCD, because of the small masses of the up and down quarks. However, experimental findings suggest that only transformations under $U(1)_V$ correspond to an exact symmetry, with the associated conserved charge being the baryon number. An evidence of the $SU(2)_V \otimes SU(2)_A$ symmetry breaking comes from the mass difference between the nucleon N and its opposite parity state $N^\star$, having masses 940 and 1535 MeV respectively. This mass splitting would not exist if $SU(2)_V \otimes SU(2)_A$ was an exact symmetry.

To understand why, let us consider a generic hadron state $|h\rangle$ and study the state $|h'\rangle \equiv Q_a^A|h\rangle$, obtained from $|h\rangle$ by applying the conserved axial charge (see Eq.(2.38)) of the symmetry $SU(2)_A$

$$Q_A^a = \int d^3x A_a^0(x), \tag{2.63}$$

with A_a^μ given in Eq. (2.58). If we focus on zero-momentum states, then $|h\rangle$ and $|h'\rangle$ are eigenstates of the QCD Hamiltonian $\mathcal{H}$, with eigenvalues

$$\mathcal{H}|h\rangle = m_h|h\rangle, \tag{2.64}$$

$$\mathcal{H}|h'\rangle = m_{h'}|h'\rangle = \mathcal{H}Q_A^a|h\rangle = Q_A^a\mathcal{H}|h\rangle = m_h|h'\rangle \quad \rightarrow \quad m_h = m'_h, \tag{2.65}$$

where m_h and $m_{h'}$ denote the masses of states $|h\rangle$ and $|h'\rangle$ respectively and we used the commutation rule $[\mathcal{H}, Q_A^a] = 0$. On the other hand, if η_h and $\eta_{h'}$ are the eigenvalues of $|h\rangle$ and $|h'\rangle$ under the parity operator P, we have

$$P|h\rangle = \eta_h|h\rangle, \tag{2.66}$$

$$\begin{aligned} P|h'\rangle &= \eta'_h|h'\rangle = PQ_A^a|h\rangle = PQ_A^aP^\dagger P|h\rangle = \eta_h(PQ_A^aP^\dagger)|h\rangle = -\eta_h Q_A^a|h\rangle \\ &= -\eta_h|h'\rangle \quad \rightarrow \quad \eta_h = -\eta_{h'}. \end{aligned} \tag{2.67}$$

Thus, if we identify $|h\rangle$ and $|h'\rangle$ with the nucleon N and its parity counterpart $N^\star$, the argument above shows that these two states would have the same mass. Even if the up and down quarks are not massless and chiral symmetry is explicitly broken, the small values of m_u and m_d cannot explain such a large discrepancy in the masses of N and $N^\star$. Theoretical and experimental arguments suggest that these breaking effects originate from the spontaneous breaking of the symmetry $SU(2)_V \otimes SU(2)_A$. We remind that [44]:

- A symmetry is said to be spontaneously broken when the Lagrangian is invariant under symmetry transformations and the ground state is annihilated only by a subset $\tilde{s}$ of all the generators of the symmetry group s. The ground state is then invariant only under transformations generated by the elements of $\tilde{s}$. Under these assumptions, the Goldstone theorem states that for each broken generator $\in \{s\} \setminus \{\tilde{s}\}$ there exists a massless spin 0 particle, the so-called *Goldstone boson*, with the same quantum number as the broken generator.

From the existence of almost degenerate particles (like proton and neutron) it seems that only the symmetry $SU(2)_V$ is preserved, therefore the chiral symmetries of QCD are thought to be spontaneously broken according to the breaking pattern

$$SU(2)_V \otimes SU(2)_A \rightarrow SU(2)_V. \tag{2.68}$$

This hypothesis is supported by the existence of $2^2 - 1 = 3$ pseudoscalar mesons (called pions), whose masses are much lighter than the other states of the hadron spectrum (their mass is around 140 MeV). Apart from the non-vanishing mass of these particles, this matches the expectations of Goldstone's theorem. The non-zero mass of the pions can be explained by the small masses of up and down quarks, that make the symmetry $SU(2)_V \otimes SU(2)_A$ only approximately realized at the level of the Lagrangian. For these reasons, pions are often called pseudo-Goldstone bosons.

The spontaneous symmetry breaking of the chiral group along with the $U(1)_A$ anomaly would deserve much more detail, because of their important physical implications. However,

a full analysis of these arguments is beyond the scope of this work and we refer to [45] for an introductory review.

2.3 Decoupling of heavy quarks

Quark masses cover a large range of energy scales, from around 2 MeV up to 170 GeV, as can be seen from Table 2.1. Compared to the typical energy scale of QCD, i.e. its Λ parameter, quarks can be ideally divided into two groups: light (up, down, strange) and heavy (charm, bottom, top) quarks. In Section 2.2 we reviewed QCD symmetries in the limit of massless quarks and analyzed their physical implications. In this research work, however, we mainly consider QCD properties in the presence of heavy quarks.

As long as one is interested in computing low energy observables which depend only on gluon and light quark fields, like the masses of pions or nucleons, effective field theory arguments [16, 17] show that heavy quarks *decouple* from $\mathcal{L}_{QCD}$ (2.4) and the dynamics of QCD is approximately insensitive to the physics of heavy quarks. This can be understood by making use of the arguments of Refs. [16, 17, 46]. In general, if we indicate the light quark fields with ϕ and the heavy quark fields with Φ, the expectation value of a generic observable $\mathcal{O}(\phi)$ reads

$$\langle \mathcal{O} \rangle = \frac{\int D\phi D\Phi \mathcal{O}(\phi) e^{iS(\phi,\Phi)}}{\int D\phi D\Phi e^{iS(\phi,\Phi)}}, \tag{2.69}$$

where $S(\phi,\Phi)$ is the action depending both on light and quark fields. After integrating out the heavy quarks fields, we obtain

$$\langle \mathcal{O}(\phi) \rangle = \frac{\int D\phi \mathcal{O}(\phi) e^{i\tilde{S}(\phi)}}{\int D\phi e^{i\tilde{S}(\phi)}}, \quad \text{with} \quad e^{i\tilde{S}(\phi)} = \int D\Phi e^{iS(\phi,\Phi)}. \tag{2.70}$$

This means that the expectation value $\langle \mathcal{O}(\phi) \rangle$ can be computed as an integral over ϕ, with weights $e^{i\tilde{S}(\phi)}$, and $\tilde{S}$ can be interpreted as the action of an effective theory depending only on the light quark fields.

Let us apply now the arguments above to QCD with N_f flavors (QCD_{N_f}). If we assume for simplicity to have N_l light degenerate quarks and $N_f - N_l$ heavy degenerate quarks of mass M, one obtains an effective theory "*decQCD*" whose Lagrangian $\mathcal{L}_{dec}$ can be expanded in powers of $(1/M)$:

$$\mathcal{L}_{dec} = \mathcal{L}_{QCD_{N_l}} + \frac{1}{M}\mathcal{L}_1 + \frac{1}{M^2}\mathcal{L}_2 + \dots \quad . \tag{2.71}$$

Here, the leading order $\mathcal{L}_{QCD_{N_l}}$ is the fundamental QCD Lagrangian depending only on the light quark and gauge fields, while $\mathcal{L}_k$, $k \geqslant 1$ are linear combinations of local operators with mass dimension $4+k$. $\mathcal{L}_k$ are operators that involve only light quark and gauge fields and they may depend also on the light quark masses. The effective Lagrangian $\mathcal{L}_{dec}$ has an infinite number of non-renormalizable terms, that however are suppressed by powers of E/M at energies $E \ll M$. Thus, to compare the fundamental theory QCD_{N_f} to the effective theory *decQCD*, their renormalized parameters must be adjusted in such a way that at energies

$E \ll M$ *decQCD* approximately reproduces the physics of QCD_{N_f}. This procedure is usually called *matching*.

The form of the operators that appear in $\mathcal{L}_k$ is determined by the symmetries of the fundamental Lagrangian, like gauge, Lorentz and chiral invariance. In many cases of physical interest, dimension five operators are forbidden and $\mathcal{L}_{dec}$ can be written as

$$\mathcal{L}_{dec} = \mathcal{L}_{QCD_{N_l}} + \frac{1}{M^2}\sum_i \omega_i \Phi_i + \ldots, \tag{2.72}$$

where $\mathcal{L}_2$ has been rewritten as a linear combination of local dimension six operators Φ_i and ω_i are some dimensionless couplings. Let us discuss now some cases where the corrections to the leading order start at $O(1/M^2)$:

- $N_l = 0$ (no light quarks)
  In absence of light quarks, $\mathcal{L}_{QCD_0}$ is just the pure gauge Lagrangian (2.6). In this case it is not possible to write dimension five operators made up of gauge fields alone and at the same time to preserve the gauge invariance. Thus, at leading order we only need to match the gauge coupling of fundamental and effective theory. A complete set of off-shell operators of dimension six is $\Phi_1 = \mathrm{Tr}\{D_\mu F_{\nu\rho} D_\mu F_{\nu\rho}\}$ and $\Phi_2 = \mathrm{Tr}\{D_\mu F_{\mu\rho} D_\nu F_{\nu\rho}\}$.

- $N_l \geq 2$ massless quarks
  In this case the chiral symmetry $SU(N_l)_V \otimes SU(N_l)_A$ in the quark sector does not allow to have dimension five operators, like the Pauli term $\frac{1}{M}\omega_{\mathrm{Pauli}}\bar{\psi} i\sigma_{\mu\nu}F^{\mu\nu}\psi$, with $\sigma_{\mu\nu} = \frac{i}{2}[\gamma_\mu, \gamma_\nu]$. Note that in principle spontaneous symmetry breaking should be taken into account, but if we restrict ourselves to the case of finite volume, the dynamical breaking of the chiral symmetry is absent[8] both in the fundamental and effective theories. Since we are assuming massless quarks, even in this case we only need to match the gauge coupling.

- $N_l \geq 2$ light quarks of mass m
  When considering finite light quark masses, the non-anomaulous chiral symmetry is explicitly broken at the level of the Lagrangian and dimension five operators are now allowed. They are formed by the same operators of $\mathcal{L}_{QCD_{N_l}}$ multiplied by the light mass m. However, we can include their effect in a redefinition of the light mass m and the gauge coupling at order m/M. Thus, even in this case we can assume that corrections to the leading order start at $O(1/M^2)$. One possible dimension six operator that contributes in Φ_i (2.72) is $\frac{1}{M} m\omega_{\mathrm{Pauli}}\bar{\psi} i\sigma_{\mu\nu}F^{\mu\nu}\psi$. This case is more complicated than the previous ones, as both gauge coupling and light quark mass have to be matched.

2.3.1 Matching

Let us focus now on the simplest cases $N_l = 0$ light quarks or $N_l \geq 2$ massless quarks. At leading order, the effective theory *decQCD* coincides with QCD_{N_l}, which has only a free

[8] See Ref. [47] for a simple proof.

parameter, the renormalized gauge coupling. The latter is fixed through the matching of *decQCD* to the fundamental theory. As discussed in Refs. [46, 48], this is equivalent to fix

$$\Lambda_{N_l} = P(M/\Lambda_{N_f})\Lambda_{N_f}, \tag{2.73}$$

where Λ_{N_l} and Λ_{N_f} are the Lambda parameters of QCD_{N_l} and QCD_{N_f}. $P(M/\Lambda_{N_f})$ is a dimensionless factor that determines the mass dependence of Λ_{N_l}. P depends on the quantity used to match QCD_{N_l} and QCD_{N_f}. This dependence is a non-perturbative $O((\Lambda_{N_f}/M)^2)$ effect. After matching the two theories according to Eq. (2.73), a generic low energy quantity m^{had} is equal in QCD_{N_f} and QCD_{N_l}, up to corrections $O((\Lambda_{N_f}/M)^2)$:

$$[m^{had}]_M^{N_f} = [m^{had}]^{N_l} + O((\Lambda_{N_f}/M)^2). \tag{2.74}$$

This implies that QCD_{N_f} and QCD_{N_l} can be matched non-perturbatively by requiring that a generic low energy observable m^{had} is the same in both theories. For m^{had} we intend either some light hadron mass or the inverse of some low energy length scale, like the well-known hadronic scales $1/r_0$ [49] or $1/\sqrt{t_0}$ [50], that will be introduced in Chapter 4. The matching of the effective theory to the fundamental one has been also addressed in perturbation theory. In particular, for QCD with solely one heavy quark (like for instance the charm or bottom quark), the decoupling relation for the renormalized gauge coupling is known up to four loops (see Refs. [17, 51–53] for further details).

Chapter 3

Lattice QCD and description of our model study

As we have seen in Chapter 2, the behavior of QCD at low energies can be understood only using non-perturbative methods. The non-perturbative approach that has been used in this work is called lattice QCD and for a detailed introduction to it we refer to [54–57]. Here we present only the main ideas behind the lattice formulation of QCD and discuss some of the methods that are more relevant for the understanding of this research work. We start with a brief introduction to the standard discretization of the fermion and gluon actions introduced by Wilson [15]. Then we present the improved clover [58] and twisted mass fermion [59, 60] actions. Finally we discuss how to compute a physical observable on the lattice and introduce our model to study charm physics.

3.1 Lattice QCD approach

Since an analytic computation of the path integral (2.13) is difficult already for relatively simple systems, computational approaches like lattice QCD are nowadays considered a standard way to proceed to determine QCD properties starting from first principles. The first step of this numerical approach is to switch to a Euclidean space, through the Wick rotation $x_0 \to ix_0$. Doing so, the QCD action becomes

$$S^E = \int d^4x(\mathcal{L}_F^E + \mathcal{L}_G^E), \tag{3.1}$$

$$\mathcal{L}_F^E = \sum_{f=1}^{N_f} \bar{\psi}^f(x)\left(\gamma_\mu^E D_\mu(x) + m_0^f\right)\psi^f(x), \tag{3.2}$$

$$\mathcal{L}_G^E = \frac{1}{2}\mathrm{Tr}\left[F_{\mu\nu}(x)F_{\mu\nu}(x)\right], \tag{3.3}$$

where the Euclidean gamma matrices are defined as

$$\gamma_0^E = \gamma_0, \quad \gamma_{i=1,2,3}^E = -i\gamma_{i=1,2,3}, \quad \{\gamma_\mu^E, \gamma_\nu^E\} = 2\delta_{\mu\nu}\mathbb{1}. \tag{3.4}$$

Moreover the expectation value of an observable $\mathcal{O}$ reads

$$\langle \mathcal{O} \rangle = \frac{1}{Z} \int D\bar{\psi} D\psi DA \mathcal{O}(\bar{\psi}, \psi, A) e^{-S^E}, \tag{3.5}$$

where Z is the partition function

$$Z = \int D\bar{\psi} D\psi DA e^{-S^E}. \tag{3.6}$$

Thus, $\langle \mathcal{O} \rangle$ can be seen as a statistical average, with weights proportional to the Boltzmann probability e^{-S^E}[1]. This makes the problem suitable to be studied by using Monte Carlo simulations, see Section 3.5. However such approach requires the use of supercomputers, on which we can deal only with a finite number of degrees of freedom. Thus, the second step is to replace the continuum Euclidean space-time with a finite 4-dimensional grid of lattice spacing a. A usual choice is to work with a lattice Λ given by

$$\Lambda = \{ n = (n_0, n_1, n_2, n_3) \,|\, n_\mu = 0, 1, \ldots N_\mu - 1 \}, \tag{3.7}$$

with $N_1 = N_2 = N_3 = N$ and $N_0 = N_t$. Moreover, when computing the Fourier transform of any arbitrary function $f(n) \in \mathbb{C}$ defined on the lattice Λ, it is important to remind that also momenta become discrete, with discretization step[2]

$$p_\mu = \frac{2\pi}{aN_\mu} k_\mu, \quad k_\mu \in \left[-\frac{N_\mu}{2} - 1, \ldots \frac{N_\mu}{2} \right]. \tag{3.8}$$

In other words, the size aN_μ of the lattice Λ determines the discretization of the momenta p_μ, whilst its lattice spacing a fixes a cutoff on the momenta equal to π/a. In this thesis we define (following Ref. [56]) the discrete Fourier transform $\tilde{f}(p)$ as

$$\tilde{f}(p) = \frac{1}{\sqrt{|\Lambda|}} \sum_n f(n) e^{-ip \cdot na} \tag{3.9}$$

and its inverse as

$$f(n) = \frac{1}{\sqrt{|\Lambda|}} \sum_p \tilde{f}(p) e^{ip \cdot na}, \tag{3.10}$$

where $|\Lambda|$ denotes the total number of lattice points

$$|\Lambda| = N_0 N_1 N_2 N_3. \tag{3.11}$$

[1] From now on we will describe QCD in a Euclidean space, therefore for the sake of simplicity we will omit the index E.

[2] Note that N_μ must be an even number.

It is also worth remembering the *master formulae* for the Kronecker deltas

$$\frac{1}{|\Lambda|}\sum_p e^{ip(n-n')a} = \delta(n-n') \quad = \quad \delta_{n_0 n_0'}\delta_{n_1 n_1'}\delta_{n_2 n_2'}\delta_{n_3 n_3'}, \tag{3.12}$$

$$\frac{1}{|\Lambda|}\sum_n e^{i(p-p')na} = \delta(p-p') \quad = \quad \delta_{k_0 k_0'}\delta_{k_1 k_1'}\delta_{k_2 k_2'}\delta_{k_3 k_3'}. \tag{3.13}$$

The introduction of a finite grid gives rise to a series of issues that will be discussed in more detail in this thesis. For instance, physical results are obtained through continuum extrapolations of values obtained at finite lattice spacing. At the same time, one should make sure that finite volume effects are negligible. Furthermore, the introduction of a grid breaks some of the symmetries that exist in the continuum theory, like Lorentz, rotational and translational symmetry. However, it is important that the lattice discretization at least does not break the gauge invariance, because if it does there would be more parameters to tune (different couplings for the quark-antiquark-gluon vertex, the 3-gluon and 4-gluon vertices and also the mass of the gluons), leading to an increase of the computation effort. Moreover, to guarantee perturbative renormalizability on the lattice, the existing proofs are based on the gauge invariance of the lattice QCD action [61].

3.2 Standard discretization

We summarize now the main ideas that lead to the standard lattice formulation of QCD [15]. First, let us naively discretize only the free fermion part of the QCD action, i.e. without the terms containing the gluon field (see Eqs.(3.1) and (3.2)). To this aim, we need to replace $\int d^4x$ with a sum over all the sites of the lattice, $a^4\sum_n$, and introduce a lattice regularization of the continuum derivative, for instance by using the symmetric formula

$$\partial_\mu \psi(x) = \frac{\psi(n+\hat{\mu}) - \psi(n-\hat{\mu})}{2a} + O(a^2), \tag{3.14}$$

where $\hat{\mu}$ is a *unit vector* in the direction μ. Thus, the naive free fermion action S_F^0 for a single quark flavor is given by

$$S_F^0[\psi,\bar{\psi}] = a^4\sum_n \bar{\psi}(n)\left(\sum_\mu \gamma_\mu \frac{\psi(n+\hat{\mu}) - \psi(n-\hat{\mu})}{2a} + m_0\psi(n)\right). \tag{3.15}$$

This kind of action gives rise to a famous problem, known as *fermion doubling*, that will be addressed at the end of this section. For the time being, let us ignore this issue and consider the role of a gauge transformation on a lattice.

3.2.1 Wilson's plaquette action and naive fermion action

Similarly to what happens in the continuum, see Eq. (2.1), a local gauge transformation can be determined by the choice of an element $\Omega(n)$ of the group $SU(3)$ at each site n of the

Figure 3.1 Link variables in the positive and negative directions (left and right hand side respectively).

lattice, such that the transformation law of a quark field $\psi(n)$ under the gauge group is

$$\psi(n) \to \Omega(n)\psi(n), \quad \bar{\psi}(n) \to \bar{\psi}(n)\Omega(n)^\dagger. \tag{3.16}$$

It is easy to see that the mass term in (3.15) is invariant under the transformation (3.16), but terms like $\bar{\psi}(n)\psi(n+\hat{\mu})$ and $\bar{\psi}(n)\psi(n-\hat{\mu})$ are not gauge invariant. To make the action (3.18) gauge invariant, the idea is to introduce a field $U_\mu(n)$ that obeys the following transformation rule under the group $SU(3)$

$$U_\mu(n) \to \Omega(n)U_\mu(n)\Omega^\dagger(n+\hat{\mu}). \tag{3.17}$$

In this way, it is possible to see that the naive fermion action

$$S_F[\psi,\bar{\psi},U] = a^4 \sum_n \bar{\psi}(n) \left(\sum_\mu \gamma_\mu \frac{U_\mu(n)\psi(n+\hat{\mu}) - U_\mu^\dagger(n-\hat{\mu})\psi(n-\hat{\mu})}{2a} + m_0\psi(n) \right) \tag{3.18}$$

is gauge invariant. $U_\mu(n)$ is a matrix of the group $SU(3)$ and represents the gauge field on a lattice. It connects two neighboring sites n and $n+\hat{\mu}$ in the direction $\hat{\mu}$ and it is often called *link variable*. It is also possible to define it in the negative direction $-\hat{\mu}$ through the relation

$$U_{-\mu}(n) \equiv U_\mu^\dagger(n-\hat{\mu}). \tag{3.19}$$

An illustration of the link variables in the positive and negative direction is shown in Figure 3.1. The connection between the link variables $U_\mu(n)$ and the lattice counterpart of the algebra-valued gauge field A_μ is given by

$$U_\mu(n) = \exp\left(ig_0 a A_\mu(n)\right). \tag{3.20}$$

Starting from these basic concepts, let us see how to construct a lattice action that preserves the gauge symmetry and in the limit $a \to 0$ reproduces the continuum pure gauge action, see Eqs. (3.1) and (3.3). The choice is not unique and we focus here on the simplest pure gauge action that we can build up by using the shortest nontrivial closed loop on the lattice. To this aim, it is important to observe that the trace of the ordered product of link variables along a closed path is a gauge invariant object (to show this is enough to use the transformation law (3.17) and the invariance of the trace under cyclic permutations). Therefore, following

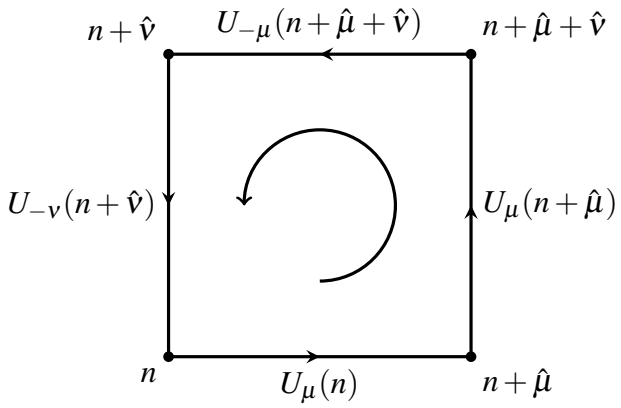

Figure 3.2 Illustration of the plaquette on a generic $\mu\nu$-plane at the coordinate n.

Wilson's idea, we consider the action

$$\begin{aligned} S_G[U] &= \beta \sum_n \sum_{\mu<\nu} \left[1 - \frac{1}{N_c} \mathrm{Re}\left(\mathrm{Tr}[U_{\mu\nu}(n)] \right) \right] \\ &= \beta \sum_n \sum_{\mu<\nu} \left[1 - \frac{1}{2N_c} \mathrm{Tr}\left[U_{\mu\nu}(n) + U^{\dagger}_{\mu\nu}(n) \right] \right], \end{aligned} \tag{3.21}$$

where β is a multiplicative factor, N_c is the number of colors ($N_c = 3$ in QCD) and $U_{\mu\nu}(n)$ is the so-called *plaquette*, which represents the shortest nontrivial closed loop on a lattice (see Figure 3.2):

$$\begin{aligned} U_{\mu\nu}(n) &= U_{\mu}(n) U_{\nu}(n+\hat{\mu}) U_{-\mu}(n+\hat{\mu}+\hat{\nu}) U_{-\nu}(n+\hat{\nu}) \\ &= U_{\mu}(n) U_{\nu}(n+\hat{\mu}) U^{\dagger}_{\mu}(n+\hat{\nu}) U^{\dagger}_{\nu}(n). \end{aligned} \tag{3.22}$$

The value of β in (3.21) has to be taken such that the action S_G reproduces the continuum pure gauge action in the limit $a \to 0$. By using Eq. (3.20) and the Baker-Campbell-Haussdorff formula[3] it is possible to rewrite the plaquette (3.22) as

$$\begin{aligned} U_{\mu\nu}(n) &= \exp\left[i g_0 a^2 \left(\partial_{\mu} A_{\nu}(n) - \partial_{\nu} A_{\mu}(n) + i g_0 [A_{\mu}(n), A_{\nu}(n)] \right) + O(a^3) \right] \\ &= \exp(i g_0 a^2 F_{\mu\nu}(n) + O(a^3)). \end{aligned} \tag{3.23}$$

By inserting this expression in (3.21) it turns out that[4]

$$S_G[U] = \beta \times \frac{g_0^2}{2N_c} \sum_n a^4 \sum_{\mu,\nu} \frac{1}{2} \mathrm{Tr}\left[F^2_{\mu\nu}(n) \right] + O(a^2), \tag{3.24}$$

[3] If A and B are two square matrices that do not commute ($[A,B] \neq 0$), the following relation holds:

$$e^A e^B = e^{A+B+\frac{1}{2}[A,B]+\cdots}$$

[4] Gauge invariance and lattice symmetries forbid $O(a)$ discretization effects in the action (3.24), see Ref. [57].

which gives the pure gauge action in the limit $a \to 0$ if we choose

$$\beta = \frac{2N_c}{g_0^2}. \tag{3.25}$$

3.2.2 Fermion doubling and Wilson term

As already mentioned in Section 3.2, a naive discretization of the fermion actions (3.15) and (3.18) produces unwanted effects in lattice calculations. To understand why, let us first find the structure of the fermion propagator in the free case. For this purpose, it is more convenient to rewrite the action (3.15) as

$$S_F^0 = a^4 \sum_{n,m} \sum_{a,b,\alpha,\beta} \bar{\psi}(n)_{\alpha a} [D(n,m)_{\substack{\alpha\beta \\ ab}} + m_0 \delta_{\alpha\beta} \delta_{ab} \delta_{nm}] \psi(m)_{\beta b}, \tag{3.26}$$

where the free *Dirac operator* $D(n,m)$ is given by

$$D(n,m)_{\substack{\alpha\beta \\ ab}} = \sum_\mu (\gamma_\mu)_{\alpha\beta} \delta_{ab} \frac{\delta_{n+\hat{\mu},m} - \delta_{n-\hat{\mu},m}}{2a}. \tag{3.27}$$

The doubling problem emerges clearly when computing the Fourier transform of $D(n,m)$, which reads (after using Eqs.(3.9), (3.10), (3.12), (3.13) and omitting for simplicity color and Dirac indices)

$$\tilde{D}(p,q) = \delta(p-q)\tilde{D}(p), \tag{3.28}$$

with

$$\tilde{D}(p) = \frac{i}{a} \sum_\mu \gamma_\mu \sin\left(p_\mu a\right). \tag{3.29}$$

Thus, the expression of the free fermion propagator in momentum space is

$$\begin{aligned} [\tilde{D}(p) + m_0]^{-1} &= \left[m_0 \mathbb{1} + \frac{i}{a} \sum_\mu \gamma_\mu \sin\left(p_\mu a\right) \right]^{-1} \\ &= \frac{m_0 \mathbb{1} - i a^{-1} \sum_\mu \gamma_\mu \sin\left(p_\mu a\right)}{m_0^2 + a^{-2} \sum_\mu \sin\left(p_\mu a\right)^2}. \end{aligned} \tag{3.30}$$

If we focus for instance on the massless case $m_0 = 0$, we see that the propagator (3.30) has the correct continuum limit

$$\tilde{D}^{-1}(p) = \frac{-i a^{-1} \sum_\mu \gamma_\mu \sin\left(p_\mu a\right)}{a^{-2} \sum_\mu \sin\left(p_\mu a\right)^2} \xrightarrow{p \cdot a \to 0} \frac{-i \sum_\mu \gamma_\mu p_\mu}{p^2}. \tag{3.31}$$

However, whilst the continuum propagator has only one pole at $p = (0,0,0,0)$, its lattice counterpart has poles whenever the components p_μ are either 0 or π/a, for a total of 16 poles: the one of the continuum, plus other 15 that come from the combinations

$$p_\mu = (\pi/a,0,0,0), (0,\pi/a,0,0), \ldots, (\pi/a,\pi/a,\pi/a,\pi/a). \tag{3.32}$$

These unwanted extra poles are called *doublers*, they do not cancel when $a \to 0$ and modify the value of the fermion propagator. This is also expected in the interacting theory (3.18), as QCD is expected to be asymptotically free. To solve this issue different fermion discretizations have been suggested.

The one that we describe in this section is called *Wilson fermion discretization*. The idea is to add to the action (3.15) an extra term, which vanishes when taking the continuum limit and at the same time it removes the contributions of the doublers from the fermion propagator. In particular, Wilson's free fermion action reads

$$\begin{aligned} S_F = a^4 \sum_n \bar{\psi}(n) \left(\sum_\mu \gamma_\mu \frac{\psi(n+\hat{\mu}) - \psi(n-\hat{\mu})}{2a} + m_0 \psi(n) \right) \\ - a^5 \frac{r}{2} \sum_n \left[\bar{\psi}(n) \left(\sum_\mu \frac{\psi(n+\hat{\mu}) + \psi(n-\hat{\mu}) - 2\psi(n)}{a^2} \right) \right], \end{aligned} \tag{3.33}$$

where r is a positive constant. When $a \to 0$, the extra term in the second line of (3.33) vanishes, because

$$\begin{aligned} a^5 \frac{r}{2} \sum_n \left[\bar{\psi}(n) \left(\sum_\mu \frac{\psi(n+\hat{\mu}) + \psi(n-\hat{\mu}) - 2\psi(n)}{a^2} \right) \right] \xrightarrow{a \to 0} \\ \approx a^5 \frac{r}{2} \sum_n \bar{\psi}(n) \left(\sum_\mu \partial_\mu \partial_\mu \psi(n) \right) \approx a \frac{r}{2} \int d^4x \bar{\psi}(x) \partial_\mu \partial_\mu \psi(x). \end{aligned} \tag{3.34}$$

If we write the action (3.33) as in Eq.(3.26) and then take the discrete Fourier transform of the Dirac operator $D(n,m)$, it is easy to show that Eq. (3.29) changes into

$$\tilde{D}(p) = \frac{i}{a} \sum_\mu \left[\gamma_\mu \sin\left(p_\mu a\right) + \mathbb{1} \frac{r}{a} \left(1 - \cos\left(p_\mu a\right)\right) \right]. \tag{3.35}$$

The last term in (3.35) is exactly what we need to remove the doublers, at least in the limit $a \to 0$. Indeed, on one hand when $p = (0,0,0,0)$ it vanishes and does not modify the value of the propagator. On the other hand, the mass contribution of a doubler with l components $p_\mu = \pi/a$ is

$$m_0 + r\frac{2l}{a}, \tag{3.36}$$

which diverges when $a \to 0$. This means that when we approach the continuum limit, the mass of the doublers becomes heavier and heavier and they decouple from the theory. This is one of the easiest ways to overcome the doubling problem and $r = 1$ is the standard value used in the numerical simulations. There exist other possibilities to avoid the fermion doubling, like for instance the staggered formulation [62], but here we will focus only on the discretizations used in our numerical setup (see Section 4.7). For further details we refer to the lattice field theory books [54–57].

We conclude this section, giving the final expression of the standard Wilson action S^W for an interacting theory with N_f flavors:

$$\begin{aligned} S^W[U,\psi,\bar{\psi}] &= S^W_G[U] + S^W_F[U,\psi,\bar{\psi}]; && (3.37)\\ S^W_G[U] &= \beta \sum_n \sum_{\mu<\nu} \left[1 - \frac{1}{N_c} \mathrm{Re}\left(\mathrm{Tr}[U_{\mu\nu}(n)] \right) \right], \quad \beta = \frac{2N_c}{g_0^2}; && (3.38)\\ S^W_F[U,\psi,\bar{\psi}] &= \sum_{f=1}^{N_f} a^4 \sum_{n,m} \bar{\psi}^f(n)[D(n,m) + m_0^f]\psi^f(m), && (3.39) \end{aligned}$$

where $D(n,m)$ is the Wilson-Dirac operator

$$\begin{aligned} D(n,m)^{\alpha\beta}_{ab} = & \frac{4r}{a}\delta_{\alpha\beta}\delta_{ab}\delta_{nm} \\ & - \frac{1}{2a}\sum_\mu \left[(r-\gamma_\mu)_{\alpha\beta} U_\mu(n)_{ab} \delta_{n+\hat{\mu},m} + (r+\gamma_\mu)_{\alpha\beta} U_\mu(n-\hat{\mu})^\dagger_{ab} \delta_{n-\hat{\mu},m} \right] \end{aligned} \tag{3.40}$$

3.2.3 Features of Wilson's action

Before introducing $O(a)$ improved actions, let us summarize some important properties of standard Wilson's action S^W (3.37):

1. S^W is invariant under the discrete symmetries C, P , T;
2. S^W if free of fermion doublers;
3. the massive Wilson-Dirac operator (see Eqs. (3.39) and (3.40))

$$D^f(n,m) = D(n,m) + m_0^f \tag{3.41}$$

   is γ^5-hermitian, namely it obeys

$$(\gamma_5 D^f)^\dagger = \gamma_5 D^f \quad \Leftrightarrow \quad (D^f)^\dagger = \gamma_5 D^f \gamma_5; \tag{3.42}$$

4. because of the γ_5-hermiticity, the eigenvalues of D^f can be either real or complex conjugate pairs. Therefore, the determinant of D^f is real;
5. the leading lattice artifacts are of order $O(a)$ in the fermion part and $O(a^2)$ in the pure gauge part.

We discuss now some consequences originating from the properties above. By using the relation (3.42) it is easy to see that even the *Wilson propagator* $[D^f]^{-1}$ possesses γ_5-hermiticity:

$$\begin{aligned} (D^f)^\dagger = \gamma_5 D^f \gamma_5 \quad &\Rightarrow \quad [(D^f)^\dagger]^{-1} = [\gamma_5 D^f \gamma_5]^{-1} \\ &\Rightarrow \quad ([D^f]^{-1})^\dagger = \gamma_5([D^f]^{-1})\gamma_5. \end{aligned} \tag{3.43}$$

The equation above leads to an important advantage in the numerical calculations in which the knowledge of a quark propagating backward is needed. Indeed, if a forward propagator $[D^f]^{-1}(n,m)$ has been already computed, applying the γ_5 matrix on both sides is sufficient to extract also $[D^f]^{-1}(m,n)$, without performing new inversions.

A consequence of the fourth item in the list above is that the massive Wilson-Dirac operator D^f is not protected against zero modes. Therefore, it can happen that for certain gauge configurations U, called *exceptional configurations*, the eigenvalues of D^f are very close to zero and the numerical inversion of the operator breaks down. To understand this, let us write the general form of the eigenvalues of $[D^f]$ as

$$m_0^f + \lambda_i[U], \tag{3.44}$$

where λ_i are the eigenvalues of D (3.40). λ_i are in general complex numbers, but in principle they can also be real negative numbers with magnitude similar to m_0^f. Therefore, to avoid the exceptional configurations, one should use a sufficiently large bare masses m_0^f that may not reproduce the physical values of baryon and meson masses. As we will see in Section 3.4, the *twisted mass* Dirac operator is not affected by this phenomenon.

Finally, it is straightforward to show that the Wilson term (3.34), introduced to remove the fermion doublers, breaks the chiral symmetry explicitly even for massless quarks. Therefore, Wilson fermions are not suitable to study phenomena that are strictly connected to chiral symmetries. Actually, this is a problem of many lattice discretizations and it originates from the famous No-Go theorem [63]. The theorem states that it is not possible to write a lattice fermion Lagrangian $\mathcal{L}_F$ which satisfies the conditions below simultaneously:

1. $\mathcal{L}_F$ is hermitian, local and invariant under traslational and chiral transformation;

2. $\mathcal{L}_F$ reproduces the correct fermion spectrum (no doublers).

These problems can be solved by an operator which fulfills a relation found by Ginsparg-Wilson and is invariant under a lattice version of the chiral symmetry [64]. Since this lattice discretization of the QCD action has not been used in this research work, we omit here the technical details that can be found in Ref. [65].

3.3 The clover fermion action

The final goal of a general lattice calculation is to compute the continuum value of a given physical observable. In practice, the standard way to proceed is to perform the measurements at different lattice spacings and find the physical value of the observable at $a = 0$ through a continuum extrapolation. As we have seen in Section 3.2, the Wilson fermion action S_F^W (3.39) and the plaquette action S_G^W (3.38) lead to $O(a)$ and $O(a^2)$ discretization effects respectively. Therefore, reducing the discretization errors on these actions can in principle pay dividends when performing continuum extrapolations, as a higher rate of convergence would be desirable.

In this section we explain how the $O(a)$ improvement in the fermion action S_F^W can be accomplished by using the so-called *clover term*, introduced in Refs. [58, 66]. In this respect, it is useful to remind that when $a \to 0$, a lattice theory can be seen as a continuum theory, which is expandable in powers of the lattice spacing a [67, 68]

$$S_{eff} = \int d^4x \left(\mathcal{L}_0 + a\mathcal{L}_1 + a^2\mathcal{L}_2 + \dots \right). \tag{3.45}$$

If we restrict ourselves to the QCD case, in Eq. (3.45) $\mathcal{L}_0$ is nothing but the QCD Lagrangian in the continuum (see Eqs.(3.2) and (3.3)), whilst $\mathcal{L}_k$, with $k \geq 1$, are terms of dimension $4+k$ that can be built up from the product of quark and gluon fields. The structure of $\mathcal{L}_k$ is restricted, as the $(k+1)$-terms have to preserve the same symmetries of the fundamental Lagrangian $\mathcal{L}_0$. In particular, it is possible to show that $\mathcal{L}_1$ can be written as a linear combination of the following operators [69, 70]

$$\begin{aligned}
O_1 &= \bar{\psi} i \sigma_{\mu\nu} F^{\mu\nu} \psi, && (3.46)\\
O_2 &= \bar{\psi} D_\mu D_\mu \psi + \bar{\psi} \overleftarrow{D}_\mu \overleftarrow{D}_\mu \psi, && (3.47)\\
O_3 &= m_0 \mathrm{Tr}\left[F_{\mu\nu} F_{\mu\nu} \right], && (3.48)\\
O_4 &= m_0 \{ \bar{\psi} \gamma_\mu D_\mu \psi - \bar{\psi} \overleftarrow{D}_\mu \gamma_\mu \psi \}, && (3.49)\\
O_5 &= m_0^2 \bar{\psi} \psi, && (3.50)
\end{aligned}$$

where D_μ is the covariant derivative introduced in Eq. (2.7), $\overleftarrow{D}_\mu$ is the covariant derivative acting on the fields on its left and

$$\sigma_{\mu\nu} \equiv \frac{i}{2} [\gamma_\mu, \gamma_\nu]. \tag{3.51}$$

It is possible to get rid of some of the operators above, by using the equation of the motion $(\gamma_\mu D_\mu + m_0)\psi = 0$. This allows to write both O_2 and O_4 as a linear combination of the operators O_1, O_3 and O_5. Moreover, looking at the form of the latter, we immediately realize that the terms O_3 and O_5 are already present in $\mathcal{L}_0$ up to some factors, thus we can incorporate them in the original action through a reparametrization of the bare parameters m_0 and g_0. This means that to get $O(a)$ improvement of the Wilson fermion action it is enough to consider

$$S_F^{cl} = S_F^W + a^5 c_{SW} \sum_n \sum_{\mu\nu} \bar{\psi}(n) \frac{i}{4} \sigma_{\mu\nu} \hat{F}_{\mu\nu}(n) \psi(n), \tag{3.52}$$

where c_{SW} is the so-called Sheikholeslami–Wohlert coefficient and $\hat{F}_{\mu\nu}$ is the lattice counterpart of the continuum operator $F_{\mu\nu}$, which reads

$$\hat{F}_{\mu\nu}(n) = \frac{1}{8a^2} \left[Q_{\mu\nu}(n) - Q_{\nu\mu}(n) \right]. \tag{3.53}$$

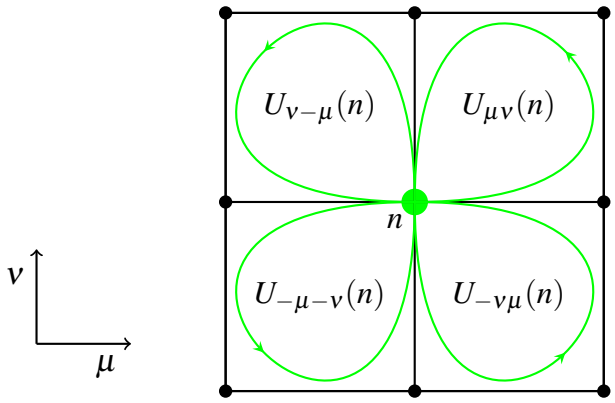

Figure 3.3 Graphical representation of the term $Q_{\mu\nu}$ introduced in Eq. (3.54).

In Eq. (3.53) $Q_{\mu\nu}(n)$ is the sum of the plaquettes in the μ-ν plane starting from the space-time coordinate n, as illustrated in Figure 3.3:

$$Q_{\mu\nu}(n) \equiv U_{\mu\nu}(n) + U_{\nu-\mu}(n) + U_{-\mu-\nu}(n) + U_{-\nu\mu}(n). \tag{3.54}$$

$O(a)$ improvement is then obtained for a certain value of c_{SW} that is not known a priori and it requires lattice simulations to be determined non perturbatively. We provide here the determination of c_{SW} obtained for $N_f = 0$ and $N_f = 2$ QCD in Refs. [71, 72], where Wilson's plaquette action S_G^W (3.38) has been used in the gluon sector

$$c_{SW}^{N_f=0} = \frac{1 - 0.656 g_0^2 - 0.152 g_0^4 - 0.054 g_0^6}{1 - 0.922 g_0^2} \qquad 0 \le g_0^2 \le 1, \tag{3.55}$$

$$c_{SW}^{N_f=2} = \frac{1 - 0.45 g_0^2 - 0.175 g_0^4 + 0.012 g_0^6 + 0.045 g_0^8}{1 - 0.720 g_0^2} \qquad 0 \le g_0^2 \le 6/5.4. \tag{3.56}$$

We stress that the procedure described here leads to $O(a)$ improvement for on-shell quantities only, like for instance the hadron masses. For off-shell quantities, like the correlation functions of local operators, an improvement of the operator is also needed to remove the $O(a)$ discretization effects.

3.4 Twisted mass QCD

In this section we present another approach to lattice fermions, that is known as twisted mass QCD (tmQCD) [59, 60]. Initially introduced to protect the Wilson-Dirac operator against zero-modes and avoid the problem of the so-called exceptional configurations, tmQCD has become a very popular formulation for the advantage of reducing the scaling violations to $O(a^2)$ without the need of any counterterms, unlike Wilson's fermion action.

3.4.1 Basic formulation for $N_f = 2$ tmQCD

Let us start giving the fermion continuum expression of the tmQCD action for $N_f = 2$ degenerate quarks in the so-called twisted-basis $\{\chi, \bar{\chi}\}$[5]:

$$S_F^{tw} = \int d^4x \bar{\chi}(x)(\gamma_\mu D_\mu + m_0 \mathbb{1}_2 + i\mu_q \gamma_5 \tau^3)\chi(x). \tag{3.57}$$

In Eq. (3.57) the quark fields χ and $\bar{\chi}$ carry, apart from the usual color and Dirac indices, a flavor index that takes $N_f = 2$ values. The matrices $\mathbb{1}_2$ and τ^3 (the third Pauli matrix, $\tau^3 = diag(1,-1)$) act on flavor space, m_0 is the usual bare quark mass and μ_q is a real parameter called *twisted mass*.

To relate tmQCD to standard QCD we can consider the following global chiral field rotation

$$\psi = R(\omega)\chi, \quad \bar{\psi} = \bar{\chi}R(\omega), \tag{3.58}$$

with

$$R(\omega) = \exp\left(i\omega\gamma_5\frac{\tau^3}{2}\right) = \cos\left(\frac{\omega}{2}\right) + i\gamma_5\tau^3 \sin\left(\frac{\omega}{2}\right), \quad R(\omega)R(-\omega) = \mathbb{1}_2. \tag{3.59}$$

Under the rotation (3.59) the action (3.57) turns into

$$S_F[\psi, \bar{\psi}, U] = \int d^4x \bar{\psi}(x) \left[\gamma_\mu D_\mu + \left(m_0 + i\mu_q\gamma_5\tau^3\right) R(-2\omega)\right] \psi(x). \tag{3.60}$$

Thus, if we introduce the so-called *polar mass M*

$$M = \left(m_0 + i\mu_q\gamma_5\tau^3\right) R(-2\omega), \tag{3.61}$$

which satisfies

$$m_0 = M\cos(\omega), \quad \mu_q = M\sin(\omega), \quad M = \sqrt{m_0^2 + \mu_q^2}, \tag{3.62}$$

the action (3.60) takes the standard form

$$S_F[\psi, \bar{\psi}, U] = \int d^4x \bar{\psi}(x) \left(\gamma_\mu D_\mu + M\right) \psi(x) \tag{3.63}$$

for a rotation $R(\omega)$ such that the angle $\omega = \arctan(\mu_q/m_0)$. The relation between the expectation values of a generic observable $\mathcal{O}$ computed in physical and twisted basis reads

$$\langle \mathcal{O}[\psi, \bar{\psi}] \rangle_{M,0} = \langle \mathcal{O}[\chi, \bar{\chi}] \rangle_{m_0,\mu_q}, \tag{3.64}$$

where $\langle \mathcal{O}[\psi, \bar{\psi}] \rangle_{M,0}$ and $\langle \mathcal{O}[\chi, \bar{\chi}] \rangle_{m_0,\mu_q}$ indicate the expectation values computed in standard QCD with quark mass M and tmQCD with bare masses m_0 and μ_q.

[5] For the sake of simplicity, we omit the unit matrices for color and Dirac space.

On the lattice, the tmQCD action for a doublet of $N_f = 2$ degenerate Wilson quarks is given by

$$S_F^{tw} = a^4 \sum_{n,m} \bar{\chi}(n) \left[D(n,m)\mathbb{1}_2 + m_0 \mathbb{1}_2 \delta_{nm} + i\mu_q \gamma_5 \tau^3 \delta_{nm} \right] \chi(m), \tag{3.65}$$

where $D(n,m)$ is the Wilson-Dirac operator (3.40). In this case, a rotation (3.59) modifies the lattice action (3.65) into

$$S_F[\psi, \bar{\psi}, U] = a^4 \sum_{m,n} \bar{\psi}(n) (D^{tw}(n,m) + M\mathbb{1}_2 \delta_{nm}) \psi(m), \tag{3.66}$$

where $D^{tw}(n,m)$ is the twisted Dirac operator, whose expression is

$$\begin{aligned} D^{tw}(n,m) = \frac{4r}{a}\delta_{nm} e^{-i\omega\gamma_5\tau^3} - \frac{1}{2a}\sum_{\mu} \left[(re^{-i\omega\gamma_5\tau^3} - \gamma_\mu) U_\mu(n) \delta_{n+\hat{\mu},m} \right] \\ - \frac{1}{2a}\sum_{\mu} \left[(re^{-i\omega\gamma_5\tau^3} + \gamma_\mu) U_\mu(n-\hat{\mu})^\dagger \delta_{n-\hat{\mu},m} \right]. \end{aligned} \tag{3.67}$$

Thus, in the *physical basis* $\{\psi, \bar{\psi}\}$ the mass and kinetic terms assume their standard form (compare with (3.40)) and only the Wilson term, which anyway vanishes when $a \to 0$, is chirally rotated. We conclude this introductory part, showing an important property of the twisted mass formulation. Indeed, it is easy to prove that the presence of the twisted mass parameter μ_q eliminate the zero modes, since

$$\begin{aligned} \det[D\mathbb{1}_2 + m_0\mathbb{1}_2 + i\mu_q\gamma_5\tau^3] &= \det[D + m_0 + i\mu_q\gamma_5] \det[D + m_0 - i\mu_q\gamma_5] \\ &= \det[D + m_0 + i\mu_q\gamma_5] \det[\gamma_5(D + m_0 - i\mu_q\gamma_5)\gamma_5] \\ &= \det[D + m_0 + i\mu_q\gamma_5] \det[D^\dagger + m_0 - i\mu_q\gamma_5] \\ &= \det[(D + m_0 + i\mu_q\gamma_5)(D^\dagger + m_0 - i\mu_q\gamma_5)] \\ &= \det[(D + m_0)(D + m_0)^\dagger + \mu_q^2] > 0. \end{aligned} \tag{3.68}$$

3.4.2 Relation between currents in physical and twisted basis

When performing a lattice calculation in tmQCD, it is important to know the relation between interpolating fields in physical and twisted basis, in order to obtain a correct physical interpretation of the results. Therefore, in this section, we summarize the relations between physical and twisted basis for the axial and vector currents along with pseudoscalar and scalar densities. In twisted basis they read

$$\begin{aligned} A_\mu^a &= \bar{\chi}\gamma_\mu\gamma^5\frac{\tau^a}{2}\chi, \quad V_\mu^a = \bar{\chi}\gamma_\mu\frac{\tau^a}{2}\chi, \\ P^a &= \bar{\chi}\gamma^5\frac{\tau^a}{2}\chi, \quad S^0 = \bar{\chi}\chi. \end{aligned} \tag{3.69}$$

To derive the expressions above in the physical basis, we only need to use the rotations defined in Eq. (3.59). A brief calculation shows that

$$\mathcal{A}_\mu^a \equiv \bar{\psi}\gamma_\mu\gamma^5\frac{\tau^a}{2}\psi = \begin{cases} \cos(\omega)A_\mu^a + \varepsilon^{3ab}\sin(\omega)V_\mu^b & (a=1,2) \\ A_\mu^3 & (a=3) \end{cases}, \tag{3.70}$$

$$\mathcal{V}_\mu^a \equiv \bar{\psi}\gamma_\mu\frac{\tau^a}{2}\psi = \begin{cases} \cos(\omega)V_\mu^a + \varepsilon^{3ab}\sin(\omega)A_\mu^b & (a=1,2) \\ V_\mu^3 & (a=3) \end{cases}, \tag{3.71}$$

$$\mathcal{P}^a \equiv \bar{\psi}\gamma_5\frac{\tau^a}{2}\psi = \begin{cases} P^a & (a=1,2) \\ \cos(\omega)P^3 + i\sin(\omega)\frac{1}{2}S^0 & (a=3) \end{cases}, \tag{3.72}$$

$$\mathcal{S}^0 \equiv \bar{\psi}\psi = \cos(\omega)S^0 + 2i\sin(\omega)P^3, \tag{3.73}$$

where we used calligraphic symbols to denote the currents in the physical basis. In the twisted basis $\{\chi,\bar{\chi}\}$, the Ward identities slightly differ from the standard form (2.59). For example, the forms of the partially conserved axial current (PCAC) and partially conserved vector current (PCVC) become

$$\partial_\mu V_\mu^a = -2\mu_q\varepsilon^{3ab}P^b, \tag{3.74}$$

$$\partial_\mu A_\mu^a = 2m_0P^a + i\mu_q\delta^{3a}S^0. \tag{3.75}$$

When rotating to the physical basis we get back to the standard relations (2.59).

3.4.3 Renormalization of tmQCD with Wilson quarks

As we have seen in Section 2.1.1, in the continuum all the parameters and fields that appear in $\mathcal{L}_{QCD}$ (2.4) are bare quantities that renormalize with a given multiplicative constant Z. This constant Z depends somehow on the regulator that has been chosen to remove the divergences.

When simulating QCD or tmQCD on a lattice, the lattice spacing acts like a regulator, as it introduces a cutoff π/a on the momenta. Therefore, on the lattice a natural choice would be to assume that the bare mass m_0 and the twisted mass μ get multiplicatively renormalized by

$$m_R = Z_m(g_0^2, a\mu)m_0, \tag{3.76}$$

$$\mu_{q,R} = Z_\mu(g_0^2, a\mu)\mu_q, \tag{3.77}$$

where μ denotes the renormalization scale. However, in the case of the bare mass m_0 there are some issues to be considered. Indeed, looking at the expression of the Wilson fermion action S_F^W (see Eqs. (3.39) and (3.40)), it is clear that the chiral symmetry is explicitly broken by the Wilson term (which is however mass-independent) even for $m_0 = 0$. This introduces a shift of the chiral point where the symmetry is restored. Thus, the quantity which renormalizes multiplicatively is no longer m_0, but $m_q = m_0 - m_{cr}$, where m_{cr} represents a critical value of the bare mass m_0 such that $m_q = 0$. In other words, in order to reproduce a vanishing

renormalized quark mass, for Wilson fermions we have to include the additive renormalization

$$m_R = Z_m(g_0^2, a\mu)m_q, \quad m_q = m_0 - m_{cr}. \tag{3.78}$$

Moreover, by using the PCVC (3.74) and PCAC (3.75) relations as normalization conditions, it is possible to find a relation between the renormalization factor Z_μ and Z_m and the renormalization factors of composite fields. In particular, it turns out that (see Refs. [59, 60, 73, 74])

$$Z_P Z_\mu = 1, \tag{3.79}$$

$$Z_{S^0} Z_m = 1, \tag{3.80}$$

where Z_P and Z_{S^0} are the renormalization factors of the pseudoscalar and scalar density respectively.

In order to connect the results between tmQCD and standard QCD on the lattice, we need to determine the value of the twist angle ω. In the renormalized theory, its definition is

$$\tan(\omega) = \frac{\mu_{q,R}}{m_R} = \frac{Z_\mu}{Z_m}\frac{\mu_q}{m_0 - m_{cr}}. \tag{3.81}$$

Thus, to compute ω one has to determine, apart from the ratio of renormalization constants, the value of the critical mass m_{cr}. The evaluation of m_{cr} is usually carried out looking at the so-called *PCAC mass*, using for instance the definition given in [75]

$$m_R = \frac{Z_A}{Z_P} m_{PCAC}, \quad m_{PCAC} = \frac{\sum_{\mathbf{x}} \langle \partial_0 A_0^a(x) P^a(0) \rangle}{2 \sum_{\mathbf{x}} \langle P^a(x) P^a(0) \rangle}, \quad a = 1,2. \tag{3.82}$$

Thus, we can write the twist angle as

$$\tan(\omega) = \frac{Z_P Z_\mu \mu_q}{Z_A m_{PCAC}} = \frac{\mu_q}{Z_A m_{PCAC}}, \tag{3.83}$$

where we used (3.79) to get rid of the renormalization factors in the numerator. The choice $\omega = \frac{\pi}{2}$, which corresponds to a vanishing PCAC mass, is often called *full* or *maximal twist*, because the physical renormalized quark mass (see Eqs. (3.62), (3.79) and (3.82))

$$m_R^{phys} = \sqrt{\frac{1}{Z_P^2}\mu_q^2 + \frac{Z_A^2}{Z_P^2} m_{PCAC}^2} = \frac{1}{Z_P}\sqrt{\mu_q^2 + Z_A^2 m_{PCAC}^2} \tag{3.84}$$

is entirely given by the twisted mass parameter μ_q.

3.4.4 $O(a)$ improvement at maximal twist

Now, we briefly discuss an important property of tmQCD, namely the $O(a)$ improvement at maximal twist. In other words, it is possible to show that at $\omega = \pi/2$ the $O(a)$ discretization errors of a large class of observables, like correlation functions between two currents measured at different lattice points, vanish and the leading corrections are of order $O(a^2)$.

To understand why, we use the Symanzik improvement program again. At maximal twist, the bare mass m_0 is tuned to its critical value m_c and therefore the untwisted renormalized mass $m_R = 0$. Thus, when $a \to 0$ we can consider the lattice action as an effective action S_{eff} that can be expanded in powers of a

$$S_{eff} = S_0 + aS_1 + O(a^2), \tag{3.85}$$

with

$$S_0 = \int d^4x \bar{\chi}(\gamma_\mu D_\mu + i\mu\gamma_5\tau^3)\chi, \quad S_1 = c_{SW}\int d^4x \bar{\chi} i\sigma_{\mu\nu}F_{\mu\nu}\chi. \tag{3.86}$$

In Eq. (3.86) S_0 contains only the twisted mass μ because we are assuming maximal twist (note that the renormalization of the untwisted mass is only multiplicative in the continuum), while the form of S_1 is the clover fermion action in twisted basis (see Section 3.3). In a similar way, a general multiplicatively renormalizable multilocal field in the effective theory can be represented by the effective field

$$\Phi_{eff} = \Phi_0 + a\Phi_1 + O(a^2), \tag{3.87}$$

where Φ_0 is its value in the continuum and Φ_1 is a suitable counterterm with the correct dimension and symmetry properties. It is easy to show that its expectation value can be written as

$$\langle\Phi_{eff}\rangle = \langle\Phi_0\rangle_0 - a\langle S_1\Phi_0\rangle_0 + a\langle\Phi_1\rangle_0 + O(a^2), \tag{3.88}$$

where the subscript $\langle\rangle_0$ denotes the continuum expectation value taken with S_0. Following [73], we introduce a transformation R^1 such that

$$R^1 : \begin{cases} \chi \to i\gamma_5\tau^1\chi \\ \bar{\chi} \to \bar{\chi} i\gamma_5\tau^1 \end{cases} . \tag{3.89}$$

Under this transformation, one finds that

$$S_0 \to S_0, \quad S_1 \to -S_1. \tag{3.90}$$

Since for gauge invariant fields the transformation (3.89) squares to the identity, a generic operator can be even or odd under the transformation R^1. In particular if Φ_0 has a given parity under R^1, it is possible to show that the counterterm Φ_1 has an opposite parity [74], i.e.

$$\Phi_0 \to \pm\Phi_0 \quad \Rightarrow \quad \Phi_1 \to \mp\Phi_1. \tag{3.91}$$

Thus, if Φ_0 is an even operator

$$\langle S_1\Phi_0\rangle_0 = -\langle S_1\Phi_0\rangle_0 = 0, \quad \langle\Phi_1\rangle_0 = -\langle\Phi_1\rangle_0 = 0, \tag{3.92}$$

otherwise

$$\langle \Phi_0 \rangle_0 = -\langle \Phi_0 \rangle_0 = 0, \quad \langle S_1 \Phi_0 \rangle_0 = \langle S_1 \Phi_0 \rangle_0, \quad \langle \Phi_1 \rangle_0 = \langle \Phi_1 \rangle_0. \tag{3.93}$$

Therefore, we can conclude that

$$\langle \Phi_{eff} \rangle = \langle \Phi_0 \rangle_0 + O(a^2) \qquad \text{for } \Phi_0 \text{ even}, \tag{3.94}$$

$$\langle \Phi_{eff} \rangle = a\,(\langle \Phi_1 \rangle_0 - \langle S_1 \Phi_0 \rangle_0) + O(a^2) \qquad \text{for } \Phi_0 \text{ odd}. \tag{3.95}$$

This means that in tmQCD at maximal twist the operators that are even under the transformation R^1 have leading lattice artifacts of order $O(a^2)$, whilst the odd operators have a vanishing expectation value.

3.5 Computing observables

Once the theory has been discretized, the purpose of a lattice QCD simulation is to find the expectation value of a generic physical observable $\mathcal{O}$, that in principle may depend on the fermion fields ψ and $\bar{\psi}$ and on the link variables U. Through the path integral representation, we have seen that expectation values can be written as

$$\langle \mathcal{O} \rangle = \frac{1}{Z} \int D[\bar{\psi}\psi] D[U] e^{-S_F[\bar{\psi},\psi,U] - S_G[U]} \mathcal{O}(\psi, \bar{\psi}, U). \tag{3.96}$$

However, the integration over the fermion fields can be carried out analytically using the fact the ψ and $\bar{\psi}$ are Grassmann numbers and the expectation value above becomes

$$\langle \mathcal{O} \rangle = \int D[U] \underbrace{\left(\frac{1}{Z} e^{-S_G[U]} \prod_{f=1}^{N_f} \det[D^f] \right)}_{\rho[U] \equiv \text{probability density}} \times \tilde{\mathcal{O}}[U], \tag{3.97}$$

where $\tilde{\mathcal{O}}[U]$ depends on U either explicitly or implicitly[6] through the inverse of the Dirac operator $[D^f]^{-1}[U]$.

Thus, the expectation value $\langle \mathcal{O} \rangle$ can be computed using Monte Carlo methods, that consist in generating an ensemble of field configurations with the probability density $\rho[U]$ and approximate $\langle \mathcal{O} \rangle$ with the sample average:

$$\langle \mathcal{O} \rangle = \bar{\mathcal{O}} \pm \delta\bar{\mathcal{O}}, \quad \bar{\mathcal{O}} = \frac{1}{N} \sum_{i=1}^{N} \mathcal{O}_i, \quad \delta\bar{\mathcal{O}} \propto \frac{1}{\sqrt{N}}, \tag{3.98}$$

where N is the size of the ensemble and $\mathcal{O}_i$ represents the observable $\mathcal{O}$ evaluated on the field configuration labeled with the index i.

The contribution of quarks in (3.97) can be ideally divided into two parts, called *sea* and *valence* quarks. Sea quarks contribute in $\det[D^f]$ via created and annihilated virtual pairs of

[6] In Chapter 4 we will discuss the shape of $\tilde{\mathcal{O}}[U]$ in the case of the meson correlators.

quarks and antiquarks, whilst valence quarks contribute in $\tilde{O}[U]$ and they are responsible of the quantum numbers of hadrons. Neglecting the effect of the sea quarks, which is equivalent to assume that $\det[D^f] = constant$, is called *quenched approximation*. The latter is considered a reasonable approximation only for heavy quarks. This can be better understood having in mind that the massive Wilson-Dirac operator D^f (see Eqs. (3.40) and (3.41)) can be written as

$$D^f \propto (\mathbb{1} - \kappa\mathcal{H}[U]), \quad \kappa = \frac{1}{2(am_0^f + 4)}, \tag{3.99}$$

where $\mathcal{H}$ is the so-called *hopping term* (we refer to [56] for its exact form). For large quark masses the *hopping parameter* κ approaches zero and we can assume that $\det[D^f] \approx$ constant.

Generating gauge configurations is not an easy task and is computationally more demanding for lattice simulations with dynamical fermions. Indeed, $\int DU$ is a high dimensional integral, with eight dimensions for each link of the lattice. To make an example, for a lattice of size 192×48^3 (which corresponds to a lattice volume employed in this work), $\int DU$ is a $679,477,248$ dimensional integral. If the simulation includes a dynamical fermion, it is necessary to compute also $\det[D^f]$, where D^f is a square matrix of size $12N^3N_t \times 12N^3N_t$. Thus, for a volume 192×48^3, D^f would correspond to a $254,803,968 \times 254,803,968$ matrix. For these reasons, the first lattice QCD simulations were performed without dynamical fermions (quenched approximation). Nowadays, the modern computer facilities allow to simulate QDC with three or four dynamical fermions, with a partial quenching of the heavy quarks ($\det[D^c] \times \det[D^b] \times \det[D^t] \approx$ constant or $\det[D^b] \times \det[D^t] \approx$ constant).

One of the most used methods to include $\det[D^f]$ in the probability density consists in introducing some auxiliary boson fields $\{\phi, \phi^\star\}$ (usually called *pseudofermion* fields) and using the well-known relation

$$\int D\phi^\star D\phi e^{-\phi^\star \frac{1}{D^f[U]}\phi} \propto \det[D^f[U]]. \tag{3.100}$$

For the conditions of existence of Eq. (3.100) we refer to [76]. QDC simulations with dynamical fermions are usually performed with the algorithms HMC and RHMC, that are based on the use of these pseudofermion fields as shown in the formula above. For further details, we refer to [54–57].

3.5.1 Error analysis

The Monte Carlo methods used in lattice QCD are typically based on the generation of the so-called *Markov chains*. The main idea behind these methods is to define a stochastic path (a Markov chain) in the space of all the possible states of a system. Such stochastic path visits, regardless of its initial point, different states with a frequency which is proportional to the desired probability density. The price to pay in this kind of algorithms is that Markov chains are generated through a certain transition matrix and this induces correlations between successive configurations.

Let us go into a bit more detail and assume that a Monte Carlo algorithm has generated an ensemble of N gauge configurations. For a given observable a, a stochastic estimator of the path integral expectation value $\langle a \rangle$ is the sample average

$$\bar{a} = \frac{1}{N} \sum_{i=1}^{N} a_i, \tag{3.101}$$

where a_i is the evaluation of a on the i-th gauge configuration. If the measurements a_i are uncorrelated, it is known that the variance of the sample average is simply given by

$$\sigma_{\bar{a}}^2 = \frac{\mathrm{var}(a)}{N}, \quad \mathrm{var}(a) = \langle (a - \langle a \rangle)^2 \rangle = \langle a^2 \rangle - \langle a \rangle^2. \tag{3.102}$$

On the other hand, when there is correlation between successive measurements this is no longer true. To see this, it is convenient to write $\sigma_{\bar{a}}^2$ as

$$\begin{aligned} \sigma_{\bar{a}}^2 = \langle (\bar{a} - \langle a \rangle)^2 \rangle_{\mathrm{MC}} &= \frac{1}{N^2} \left\langle \left(\sum_{i=1}^{N} (a_i - \langle a \rangle) \right)^2 \right\rangle_{\mathrm{MC}} = \frac{1}{N^2} \left\langle \left(\sum_{i=1}^{N} \delta a_i \right)^2 \right\rangle_{\mathrm{MC}} \\ &= \frac{1}{N^2} \sum_{i=1}^{N} \sum_{j=1}^{N} \langle \delta a_i \delta a_j \rangle_{\mathrm{MC}} = \frac{1}{N^2} \sum_{i=1}^{N} \sum_{j=1}^{N} \langle \delta a_i \delta a_j \rangle, \end{aligned} \tag{3.103}$$

where

$$\delta a_i = a_i - \langle a \rangle \tag{3.104}$$

denotes the deviation of the measurement a_i from the expectation value and the symbol $\langle \rangle_{\mathrm{MC}}$ denotes an average over infinitely many Markov chains of length N. To evaluate Eq. (3.103), let us introduce the so-called *autocorrelation function*

$$\Gamma_a(t) \equiv \langle a_i a_{i+t} \rangle - \langle a \rangle^2 = \langle \delta a_i \delta a_{i+t} \rangle, \tag{3.105}$$

which satisfies

$$\Gamma_a(t) = \Gamma_a(-t), \quad \Gamma_a(0) = \mathrm{var}(a). \tag{3.106}$$

$\Gamma_a(t)$ depends only on the difference t because of the translation invariance in Monte Carlo time. Inserting the autocorrelation function $\Gamma_a(t)$ in (3.103) we have

$$\begin{aligned} \sigma_{\bar{a}}^2 &= \frac{1}{N^2} \sum_{i=1}^{N} \sum_{j=1}^{N} \Gamma_a(|i-j|) = \frac{1}{N^2} \sum_{t=-(N-1)}^{N-1} \sum_{k=1}^{N-|t|} \Gamma_a(|t|) \\ &= \frac{1}{N^2} \sum_{t=-(N-1)}^{N-1} (N - |t|) \Gamma_a(|t|) = \frac{1}{N^2} \sum_{t=-N}^{N} (N - |t|) \Gamma_a(|t|) \\ &= \frac{1}{N} \sum_{t=-N}^{N} \Gamma_a(|t|) \left(1 - \frac{|t|}{N} \right) \approx \frac{1}{N} \left(\Gamma_a(0) + 2 \sum_{t=1}^{N} \Gamma_a(t) \right). \end{aligned} \tag{3.107}$$

The last step is justified only if we consider a large statistics N and we assume that $\Gamma_a(t) \approx 0$ when $t \gg 1$. Finally, after defining the normalized autocorrelation function

$$\rho_a(t) \equiv \frac{\Gamma_a(t)}{\Gamma_a(0)} \tag{3.108}$$

and the integrated autocorrelation time

$$\tau^a_{int} = \frac{1}{2} + \sum_{t=1}^{N} \rho_a(t), \tag{3.109}$$

it is easy to show that

$$\sigma^2_{\bar{a}} = \frac{\mathrm{var}(a)}{N} \times 2\tau^a_{int}. \tag{3.110}$$

From the equation above, we realize that working with correlated data is equivalent to work with a reduced sample of uncorrelated data, with size $N_{eff} = N/2\tau^a_{int}$. In practice, we have to work only with a biased estimator of the correlation function Γ_a, because $\langle a \rangle$ is not known a priori and its value is replaced with the sample average $\bar{a}$. The asymptotic behavior of the normalized autocorrelation function (3.108) is typically given by

$$\rho_a(t) \sim A \exp\left(-\frac{t}{\tau_{exp}}\right), \tag{3.111}$$

where A is a constant which depends on the observable and τ_{exp}, known as *exponential autocorrelation time*, represents a characteristic of the Markov chain.

The arguments above can be generalized to the case of more observables, as shown in Ref. [77]. For instance, let us assume to have a derived observable F that depends on N_α primary observables $F \equiv F(a^1, \dots a^{N_\alpha})$ and whose expectation value is

$$\langle F \rangle = F(\langle a^1 \rangle, \dots, \langle a^{N_\alpha} \rangle). \tag{3.112}$$

With arguments similar to the ones that led to Eq. (3.110), it is possible to show that

$$\sigma^2_F = \frac{\Gamma_F(0)}{N} \times 2\tau^F_{int}, \quad \tau^F_{int} = \frac{1}{2} + \sum_{t=1}^{N} \rho_F(t), \tag{3.113}$$

with

$$\begin{aligned} \rho_F(t) &= \sum_{t=1}^{N} \frac{\Gamma_F(t)}{\Gamma_F(0)}, \\ \Gamma_F(t) &= \sum_{\alpha\beta} \left[\frac{\partial F}{\partial a^\alpha}\right]_{a^\alpha = \bar{a}^\alpha} \left[\frac{\partial F}{\partial a^\beta}\right]_{a^\beta = \bar{a}^\beta} \Gamma_{\alpha\beta}(t), \\ \Gamma_{\alpha\beta}(t) &\equiv \langle a^\alpha_i a^\beta_{i+t} \rangle - \langle a^\alpha \rangle \langle a^\beta \rangle = \langle \delta a^\alpha_i \delta a^\beta_{i+t} \rangle. \end{aligned} \tag{3.114}$$

In this work the effect of the autocorrelations in Monte Carlo data has been taken into account, both for primary and derived observables, using the Matlab package *UWerr.m* (see Ref. [77] for details about the software).

3.5.2 Scale setting

When simulating the QCD action on a computer, all the numbers we input are dimensionless, because g_0 is a pure number and the other parameters and fields are given in units of the lattice spacing a. As a consequence, even the observables that we compute in a lattice QCD simulation are dimensionless and to convert them in physical units we need to know the value of the lattice spacing.

For instance, in a theory with two light degenerate quarks ($m_u = m_d$) and a strange quark of mass m_s ($N_f = 2+1$ QCD), the standard approach consists in performing several simulations for a fixed value of g_0, varying the values of the bare quark masses. Then one computes hadron masses from the exponential decay of suitable correlation functions (see Section 4.1) and fixes the value of the bare masses requiring that some mass ratios of different hadrons correspond to their physical value, e.g.

$$\frac{am_h}{am_p} = \frac{m_h^{phys}}{m_p^{phys}}, \quad h = K, \pi. \tag{3.115}$$

Here the symbols p, K, π denote a proton, a kaon and a pion, $am_{p,K,\pi}$ are their masses obtained from the simulation and $m_{p,K,\pi}^{phys}$ indicate their experimental values. The lattice spacing corresponding to the bare coupling g_0 can be determined, for instance, from the ratio

$$a = \frac{am_p}{m_p^{phys}}. \tag{3.116}$$

In alternative, one can fix the lattice spacing either through other hadron masses, or a pseudoscalar decay constant or a particular reference scale like r_0 [49] or $\sqrt{t_0}$ [50], that will be introduced in Sections 4.3.2 and 4.6. Once the lattice spacing a and bare masses have been determined, a lattice simulation can predict the value of any other mass m through

$$m = am(g_0, am_u, am_s)\frac{m_p^{phys}}{am_p} + O(a^d), \tag{3.117}$$

where $O(a^d)$ represents the size of the scaling violations and usually depends on the lattice action.

3.5.3 Continuum limit

If we want to extract physical information from a lattice QCD calculation, we need to perform the limit $a \to 0$. It is possible to show that this limit is reached when $g_0 \to 0$. To understand why, let us focus for simplicity on a pure gauge theory and consider a physical observable $\mathcal{O} \equiv \mathcal{O}(g_0, a)$. When the lattice spacing is small enough, we expect that such observable is

independent of a, up to small scaling violations which are typically of order $O(a^2)$. This gives rise to a Renormalization Group Equation similar to the one we have seen in Section 2.1.2:

$$\left[a\frac{\partial}{\partial a} - \beta_{lat}(g_0)\frac{\partial}{\partial g_0}\right]\mathcal{O}(g_0,a) = 0 + O(a^2), \tag{3.118}$$

where

$$\beta_{lat}(g_0) = -a\frac{\partial g_0}{\partial a} \tag{3.119}$$

is the lattice counterpart of the β-function (2.22). Its perturbation expansion for small g_0 is equivalent to (2.24)[7] and solving (3.119) one finds the integration constant

$$\Lambda_{lat} = \frac{1}{a}(b_0 g_0^2)^{-\frac{b_1}{2b_0^2}} e^{-\frac{1}{2b_0 g_0^2}}(1 + O(g_0^2)), \tag{3.120}$$

that is identical to (2.27) if we replace $\mu \to 1/a$ and $g_R \to g_0$. Therefore, when $a \to 0$ the asymptotic behavior of g_0 is

$$g_0^2(a) = \frac{1}{b_0 \log\left(\frac{1}{a^2\Lambda_{lat}^2}\right)} \quad \Rightarrow \quad \lim_{a\to 0} g_0^2(a) = 0. \tag{3.121}$$

Note that the limit $g_0 \to 0$ represents a critical point of the system, because the correlation length ξ of a given particle of mass m diverges, as $\xi = 1/(am)$. Thus, when extracting the continuum limit one has to choose $g_0(a)$ such that the following relations are verified

$$1 \ll \xi_{min}, \quad \xi_{max} \ll N. \tag{3.122}$$

Here ξ_{min} and ξ_{max} denote the minimum and maximum correlation lengths of the system respectively and their value is determined from the heaviest and lightest particles of the theory. Moreover, for lattice field theory one expects that the integrated autocorrelation time of an observable a is related to its correlation length ξ_a through

$$\tau_{int}^a \sim \xi_a^z \sim a^{-z}. \tag{3.123}$$

The *dynamical critical exponent* $z \geqslant 0$ usually depends on the Monte Carlo algorithm and on the observable. The relation (3.123) leads to the so-called *critical slowing down* and limits the range of lattice spacings that can be explored. On top of this, we remind that to keep the physical volume constant the number of lattice sites in 4 dimensions increases as a^{-4}. Therefore, when approaching the critical point $g_0 = 0$, the computational effort of lattice QCD simulations grows at least as:

$$\textit{numerical cost} \propto \left(\frac{1}{a}\right)^{z+4}. \tag{3.124}$$

[7] We remind that only b_0 and b_1 are universal. The other coefficients depend on the renormalization scheme.

Further limitations come from the convergence rate of the inversion of the Dirac operator, which is governed by the condition number $h \sim 1/(m_0^f a)$ [78]. In modern lattice QCD simulations, the typical range of lattice spacings is 0.05 fm $\lesssim a \lesssim$ 0.10 fm.

3.6 Open boundary conditions

Lattice QCD simulations are performed in a finite size grid, therefore boundary conditions need to be implemented. The standard choice is to use periodic boundary (PB) conditions in space and time for the gauge field $U_\mu(n)$ and antiperiodic in time for the fermion fields. However, for QCD simulations at small lattice spacings, the choice of these boundary conditions leads to large autocorrelation times for the topological charge (2.62), as the latter gets trapped in fixed topological charge sectors. This phenomenon, called *freezing of the topological charge*, can produce biased estimates of a path integral, because the sampling of the gauge configurations is limited to certain regions of the field space. In Ref. [79] it has been shown that such problems can be reduced making use of *open boundary* (OB) conditions in the time direction. In this way, the topological charge can flow through the boundaries and all the relevant regions of the field space become accessible. In the continuum, OB conditions in time are imposed requiring that the gauge field tensor $F_{\mu\nu}$ satisfies

$$F_{0\nu}(0,\vec{x}) = F_{\nu 0}(T,\vec{x}) = 0, \tag{3.125}$$

where $x_0 = 0$ and $x_0 = T$ are the values of the time coordinate at the boundaries. PB conditions are still imposed in space directions. As for the fermion fields, OB conditions in time are fixed through

$$\begin{aligned} P_+ \psi(x)|_{x_0=0} &= P_- \psi(x)|_{x_0=T} = 0, \\ \bar{\psi}(x) P_-|_{x_0=0} &= \bar{\psi}(x) P_+|_{x_0=T} = 0, \end{aligned} \tag{3.126}$$

where

$$P_\pm = \frac{1}{2}(1 \pm \gamma_0). \tag{3.127}$$

On the lattice, choosing OB conditions in time slightly changes the form of the discretized actions. For instance, Wilson's plaquette gauge action becomes

$$S_G^{W,ob} = \beta \sum_n \sum_{\mu<\nu} \omega \left[1 - \frac{1}{N_c} Re(Tr[U_{\mu\nu}(n)]) \right], \tag{3.128}$$

where the weight ω is set to

$$\omega = \begin{cases} \frac{1}{2} c_G & \text{for space-like plaquettes at } n_0 = 0 \text{ and } n_0 = T = a(N_t - 1), \\ 1 & \text{otherwise.} \end{cases} \tag{3.129}$$

c_G is a free parameter that is usually set to 1 to obtain on-shell $O(a)$ improvement at tree level. As concerns the fermion action, a clover improved doublet of twisted mass Wilson fermions

is described by the action

$$S_F^{tw,ob} = a^4 \sum_{n,m} \bar{\chi}(n) \left[D(n,m)\mathbb{1}_2 + m_0\mathbb{1}_2 + \delta D_b \mathbb{1}_2 \delta_{nm} + i\mu_q \gamma_5 \tau^3 \delta_{nm} \right] \chi(m) + a^5 c_{SW} \sum_n \sum_{\mu\nu} \bar{\chi}(n) \frac{i}{4} \sigma_{\mu\nu} \hat{F}_{\mu\nu}(n) \chi(n), \tag{3.130}$$

where the fermion fields satisfy boundary conditions of the Schrödinger Functional type

$$\chi(n)|_{n_0=0} = 0 \quad \text{and} \quad \chi(n)|_{n_0=a(N_t-1)} = 0 \tag{3.131}$$

and δD_b is a boundary improvement term given by

$$\delta D_b \chi(n) = \{(c_F - 1)\delta_{n_0,a} + (c_F - 1)\delta_{n_0,a(N_t-2)}\}\chi(n). \tag{3.132}$$

Setting the parameter $c_F = 1$ in the formula above gives on-shell $O(a)$ improvement at tree level. For further details we refer to the documentation of the software openQCD[8]. The actions (3.128) and (3.130) correspond to the lattice discretization used in this work. More details regarding the lattice setup will be given in Chapter 4.

Even though choosing OB conditions reduces the critical slowing down at small lattice spacings, such numerical setup produces some drawbacks. For instance, this setup explicitly breaks time translational invariance, which is a symmetry of QCD in the continuum. Moreover, when local observables are set close to the boundaries, they are affected by boundary effects that alter the corresponding vacuum expectation values. As we will see better in Chapter 4, these undesired effects decay exponentially far away from the boundaries and become negligible towards the middle of the lattice. This means that the usable portion of lattice gets reduced to a fraction that typically depends on the observables. In some cases, boundary effects can be canceled forming suitable ratio of two-point correlation functions [80] and this will be our strategy to extract meson decay constants.

3.7 Typical QCD simulations

Nowadays, many large scale QCD simulations are carried out in the 2+1 flavor theory, i.e. with light quarks only (see for instance Refs. [81–85]). The main reasons for not including a dynamical charm quark are explained below.

1. When simulating QCD on a lattice, one has to face a multi-scale problem. Indeed, on one hand the spatial lattice size L must be large enough to accommodate a physical pion, i.e.

$$L \gg \frac{1}{m_\pi}, \tag{3.133}$$

where m_π is the mass of a pion (~ 140 MeV). This is due to unwanted finite volume effects on the particle energy spectra [86], whose leading contribution originates from

[8] http://luscher.web.cern.ch/luscher/openQCD/

the smallest mass hadron (i.e. the pion) and is given by $O(e^{-Lm_\pi})$. In QCD simulations, L usually has to satisfy the rule of thumb $Lm_\pi > 4$, for which it has been seen that such effects can be neglected. On the other hand, the lattice spacing a must be fine enough to resolve the small correlation associated with charmonium states, that are bound states made of a charm quark (c) and a charm antiquark $\bar{c}$. This means that to reduce possible discretization effects, the lattice spacing should roughly satisfy

$$a < \frac{1}{m_{J/\psi}} \approx 0.064 \text{ fm}, \tag{3.134}$$

where $m_{J/\psi}$ is the mass of the vector charmonium state J/ψ.

2. Including a dynamical charm quark increases the costs of the simulation and requires the tuning of a further bare parameter.

3. If one is interested in low energy quantities, with energies E much smaller than the RGI charm mass M_c, decoupling of charm quark applies and the loop effects due to a dynamical charm quark can be neglected, with leading order power corrections of size $O(1/M_c^2)$. This is further confirmed in Refs. [46, 48, 87, 88], where it is shown that the effect of a dynamical charm quark on low energy quantities requires a very high precision to be resolved.

3.8 Our model to study charm physics

One of the main goals of this work is to understand how reliable $N_f = 2+1$ QCD is to describe charm physics, with special focus on charmonium systems. The charmonium system, frequently characterized as the "hydrogen atom" of meson spectroscopy owing to the fact that it is non-relativistic enough to be reasonably well described by certain potential models, is the perfect testing ground for a comparison of theory with experiment. Moreover, in the last few years there has been a renewed interest in spectral calculations with charmonia, because of the experimental discovery of many unexpected states, see Figure 3.4, which highlight the need for a more complete theoretical understanding, be they hybrid mesons, tetra-quarks or some other hitherto unknown form of matter.

For such studies, $N_f = 2+1+1$ QCD would be a better setup than $N_f = 2+1$ QCD, as it removes any systematic errors originating from the "quenching" the charm quark. However, for what we have seen in the previous sections, the inclusion of a heavy dynamical charm quark requires

- high precision in low energy observables to resolve tiny charm loop effects;
- small lattice spacings to control cutoff effects proportional to the quark mass.

The points above lead to a significant increase of the computational costs, therefore it is important to understand if $N_f = 2+1$ QCD can be suitable to study charm physics. Since a comparison of $N_f = 2+1$ and $N_f = 2+1+1$ simulations is still obscured by many

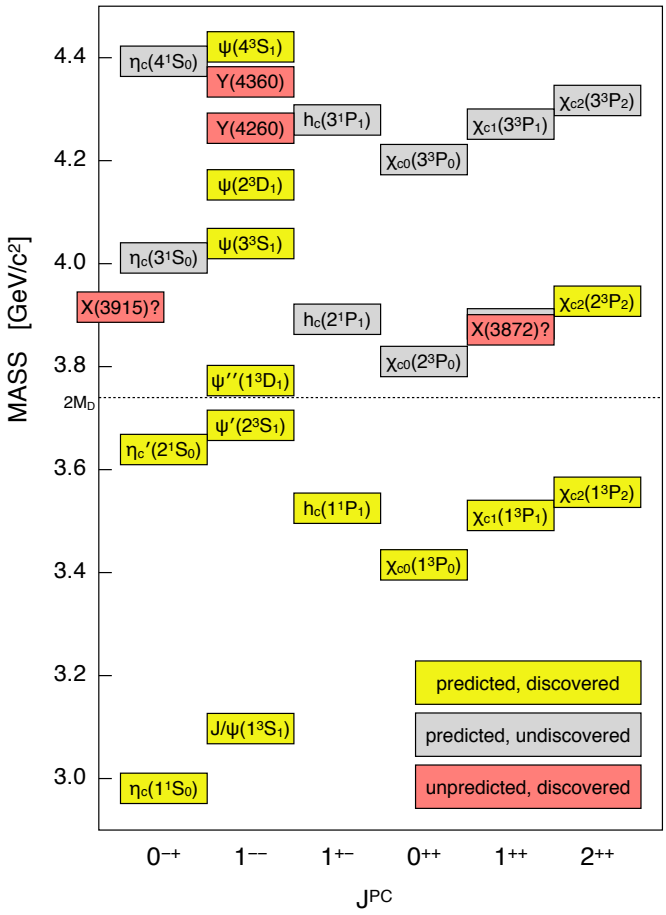

Figure 3.4 Picture taken from a talk by R. Mitchell: it shows the masses of charmonium states as a function of spin, parity and charge conjugation, J^{PC}. The yellow boxes represent charmonium states which are predicted by theory and discovered by experiments, the grey ones describe states that are predicted by the theory, but still undiscovered and the red ones denote particles discovered by the experiments, but whose nature is not well understood yet.

uncertainties, we consider here a simplified setup. We compare results for different physical observables obtained with two different models:

- $N_f = 2$ QCD with two degenerate charm quarks;
- $N_f = 0$ QCD, which is also called quenched QCD.

The absence of light quarks allows us to keep the volumes moderately large, which in turn makes simulations at extremely fine lattice spacings feasible. For low energy observables without explicit charm-quark dependence, decoupling applies and the effects are expected to be small. But we study also quantities with explicit charm-quark dependence, like the charmonium mass spectrum, where it is not known a priori if decoupling applies. Our study puts an emphasis on careful continuum extrapolations, which require very small lattice spacings when heavy quarks are present in the action.

Chapter 4

Observables and Methodology

In this chapter we introduce the observables under investigation in this thesis and the methods that have been used to determine them. We focus both on pure gluonic observables, like the QCD static potential and the strong coupling α_{qq} extracted from the static force, and on observables with an explicit charm-quark dependence, like charmonium masses and decay constants. Finally we present the lattice setup used in this research work.

4.1 Correlation functions

Physical information from lattice QCD is generally extracted from suitable *Euclidean correlators*. For the time being, let us assume for simplicity to have a scalar field theory discretized in a periodic box of volume L^3 and that the field ϕ satisfies the boundary conditions in time $\phi(0,\vec{x}) = \phi_i(\vec{x})$ and $\phi(T,\vec{x}) = \phi_f(\vec{x})$. Under this assumptions it is known that the *Euclidean correlator*

$$\begin{aligned} &\langle O_2(x)O_1(y)\rangle_T \equiv \frac{1}{Z_T}\langle\phi_f|e^{-(T-x_0)\hat{H}}\hat{O}_2(\vec{x})e^{-(x_0-y_0)\hat{H}}\hat{O}_1(\vec{y})e^{-y_0\hat{H}}|\phi_i\rangle, \\ &Z_T = \langle\phi_f|e^{-\hat{H}T}|\phi_i\rangle, \end{aligned} \tag{4.1}$$

can be expressed through the path integral

$$\begin{aligned} \langle O_2(x)O_1(y)\rangle_T &= \frac{1}{Z_T}\int D\phi O_2[\phi(x)]O_1[\phi(y)]e^{-S[\phi]}, \\ Z_T &= \int D\phi e^{-S[\phi]}. \end{aligned} \tag{4.2}$$

In Eqs. (4.1) and (4.2) $\hat{H}$ is the Hamiltonian operator and $\hat{O}_1$ and $\hat{O}_2$ are two generic operators defined at the space-time points $x = (x_0,\vec{x})$ and $y = (y_0,\vec{y})$. $|\phi_i\rangle$ and $|\phi_f\rangle$ are the eigenstates of the field operator $\hat{\phi}(\vec{x})$ at the boundaries $x_0 = 0$ and $x_0 = T$.

Let us evaluate Eq. (4.1) after the insertion of a complete set of eigenstates of $\hat{H}$

$$\hat{H}|\vec{p},l\rangle = E_l(\vec{p})|\vec{p},l\rangle, \tag{4.3}$$

where $\vec{p}$ denotes the momentum of the states and l indicates other quantum numbers. We assume that the states have the following normalization

$$\langle \vec{p}, l | \vec{q}, m \rangle = \delta_{lm} \delta_{\vec{p},\vec{q}} \tag{4.4}$$

and we write the identity as

$$\mathbb{1} = \sum_{\vec{p},l} |\vec{p}, l\rangle \langle \vec{p}, l|, \tag{4.5}$$

where the vacuum state $|0\rangle$ is defined as

$$|0\rangle \equiv |\vec{0}, 0\rangle. \tag{4.6}$$

After inserting three times the identity (4.5) in Eq. (4.1), we obtain

$$\begin{aligned} \langle O_2(x) O_1(y) \rangle_T = \frac{1}{Z_T} \sum_{l,m,n} \sum_{\vec{p},\vec{q},\vec{s}} & \langle \phi_f | \vec{p}, l \rangle e^{-(T-x_0)E_l(\vec{p})} \langle \vec{p}, l | \hat{O}_2(\vec{x}) | \vec{q}, m \rangle \\ & \times e^{-(x_0-y_0)E_m(\vec{q})} \langle \vec{q}, m | \hat{O}_1(\vec{x}) | \vec{s}, n \rangle e^{-y_0 E_n(\vec{s})} \langle \vec{s}, n | \phi_i \rangle, \end{aligned} \tag{4.7}$$

with

$$Z_T = \sum_{\vec{p},l} \langle \phi_f | \vec{p}, l \rangle e^{-TE_l(\vec{p})} \langle \vec{p}, l | \phi_i \rangle \xrightarrow[T\to\infty]{} \langle \phi_f | 0 \rangle e^{-TE_0} \langle 0 | \phi_i \rangle, \tag{4.8}$$

where $E_0 \equiv E_0(\vec{0})$ is the energy of the vacuum $|0\rangle$. The correlation function (4.7) receives also contributions from the boundary states, but if we put the *source* y_0 and the *sink* x_0 far away from the boundaries, these effects become negligible. Thus, if we consider the limits $T \to \infty$, $T - x_0 \to \infty$ and $y_0 \to \infty$ the expression (4.7) gets simplified in

$$\begin{aligned} \lim_{\substack{T\to\infty \\ T-x_0, y_0 \to \infty}} \langle O_2(x) O_1(y) \rangle_T &= \frac{1}{Z_T} \sum_{\vec{q},m} \langle \phi_f | 0 \rangle e^{-(T-x_0)E_0} \langle 0 | \hat{O}_2(\vec{x}) | \vec{q}, m \rangle \\ &\quad \times e^{-(x_0-y_0)E_m(\vec{q})} \langle \vec{q}, m | \hat{O}_1(\vec{x}) | 0 \rangle e^{-y_0 E_0} \langle 0 | \phi_i \rangle \\ &= \sum_{\vec{q},m} \langle 0 | \hat{O}_2(\vec{x}) | \vec{q}, m \rangle e^{-(x_0-y_0)\Delta E_m(\vec{q})} \langle \vec{q}, m | \hat{O}_1(\vec{y}) | 0 \rangle, \end{aligned} \tag{4.9}$$

where in the last line we have defined $\Delta E_m(\vec{q}) = E_m(\vec{q}) - E_0$ and canceled the amplitudes $\langle \phi_f | 0 \rangle$ and $\langle 0 | \phi_i \rangle$, as they appear also in Z_T (see Eq. (4.8)). Note that in the equations above we are assuming that the boundary states $|\phi_{i,f}\rangle$ share the same quantum numbers of the vacuum. For this to happen, it is enough that $|\phi_{i,f}\rangle$ can be written as linear combinations of all the states with vacuum quantum numbers. As the correlator (4.9) depends only on energies normalized relative to the energy E_0 of the vacuum (the ones that can be actually measured in an experiment), from now on we replace the symbol $\Delta E_m(\vec{q}) = E_m(\vec{q}) - E_0$ with $E_m(\vec{q})$. As a consequence, the energy of the vacuum $|0\rangle$ is normalized to zero. The operators $\hat{O}_{1,2}$ can be shifted to the origin through the translation operator and therefore we can rewrite Eq. (4.9) as

$$\lim_{\substack{T\to\infty \\ T-x_0, y_0 \to \infty}} \langle O_2(x) O_1(y) \rangle_T = \sum_{\vec{q},m} e^{i\vec{q}\cdot(\vec{x}-\vec{y})} \langle 0 | \hat{O}_2 | \vec{q}, m \rangle e^{-(x_0-y_0)E_m(\vec{q})} \langle \vec{q}, m | \hat{O}_1 | 0 \rangle. \tag{4.10}$$

The expression (4.10) is very important in lattice field theories, as it allows to extract the energy levels of a generic particle. Indeed, if $\hat{O}_1$ is an operator $\hat{O}^\dagger$ which creates from the vacuum a particle with certain quantum numbers and $\hat{O}_2$ is the adjoint operator $\hat{O}$ which annihilates this particle, the two-point correlation function becomes

$$\lim_{\substack{T\to\infty \\ T-x_0,y_0\to\infty}} \langle O(x)O^\dagger(y)\rangle_T = \sum_{\vec{q},m} e^{i\vec{q}\cdot(\vec{x}-\vec{y})} |\langle \vec{q},m|\hat{O}^\dagger|0\rangle|^2 e^{-(x_0-y_0)E_m(\vec{q})}. \tag{4.11}$$

Since the matrix element $\langle \vec{q},m|\hat{O}^\dagger|0\rangle$ is different from zero only for states $|\vec{q},m\rangle$ with the same quantum numbers of the particle created by the operator $\hat{O}^\dagger$, the correlator (4.11) becomes a sum of exponentials, where each term corresponds to the energy levels of the particle of interest. If we want to study a particle with a given momentum, it is enough to consider the Fourier transform of the sink operator

$$\tilde{O}(x_0,\vec{k}) = \frac{1}{\sqrt{N^3}} \sum_{\vec{x}} O(x_0,\vec{x}) e^{-i\vec{k}\cdot\vec{x}} \tag{4.12}$$

and study the correlator $\langle \tilde{O}(x_0,\vec{k})O^\dagger(y)\rangle_T$. Indeed,

$$\begin{aligned} \lim_{\substack{T\to\infty \\ T-x_0,y_0\to\infty}} \langle \tilde{O}(x_0,\vec{k})O^\dagger(y)\rangle_T &= \frac{1}{\sqrt{N^3}} \sum_{\vec{x}} \sum_{\vec{q},m} e^{i(\vec{q}-\vec{k})\cdot\vec{x}} e^{-i\vec{q}\cdot\vec{y}} |\langle \vec{q},m|\hat{O}^\dagger|0\rangle|^2 e^{-(x_0-y_0)E_m(\vec{q})} \\ &= \sqrt{N^3} \sum_{m} e^{-i\vec{k}\cdot\vec{y}} |\langle \vec{k},m|\hat{O}^\dagger|0\rangle|^2 e^{-(x_0-y_0)E_m(\vec{k})}. \end{aligned} \tag{4.13}$$

The choice $\vec{k}=\vec{0}$ corresponds to the zero-momentum projection and allows to extract the particle masses. In this case a two-point correlation function can be written as

$$\begin{aligned} f(x_0,y_0) &\equiv \lim_{\substack{T\to\infty \\ T-x_0,y_0\to\infty}} \langle \tilde{O}(x_0,\vec{0})O^\dagger(y)\rangle_T \\ &= A_0 e^{-(x_0-y_0)m_0} + A_1 e^{-(x_0-y_0)m_1} + A_2 e^{-(x_0-y_0)m_2} \ldots, \end{aligned} \tag{4.14}$$

where A_0, A_1, etc. are some coefficients proportional to the squared amplitudes $|\langle \vec{0},m|\hat{O}^\dagger|0\rangle|^2$, m_0 is the mass of the ground state of the particle of interest and m_1, m_2, etc. are the masses of its excited states. If we want to extract the mass of the ground state, it is convenient to study the so-called *effective mass*

$$am_{eff}\left(x_0+\frac{a}{2},y_0\right) \equiv \log\left(\frac{f(x_0,y_0)}{f(x_0+a,y_0)}\right), \tag{4.15}$$

that for large time separations x_0-y_0 gives

$$\lim_{x_0-y_0\to\infty} am_{eff}\left(x_0+\frac{a}{2},y_0\right) = am_0. \tag{4.16}$$

Particle masses are typically computed through the weighted plateau average of the effective mass (4.15)

$$am = \frac{\sum_{x_0=t_i}^{t_f} w(x_0+a/2,y_0) am_{eff}(x_0+a/2,y_0)}{\sum_{x_0=t_i}^{t_f} w(x_0+a/2,y_0)}, \tag{4.17}$$

where $x_0 = t_{i,f}$ are the start and the end of the plateau, the weights w are given by the inverse squared errors of the corresponding effective masses and t_i is chosen such that excited state contributions are completely negligible.

The results of this section can be easily generalized to the QCD case. We just need to replace scalar fields with fermion and gluon fields and construct suitable operators that annihilate and create the particle states we want to investigate. Using the OB conditions in time discussed in Section 3.6 the boundary states $|\phi_{i,f}\rangle$ will be simply denoted by the state $|\Omega\rangle$, as the conditions at the boundaries $x_0 = 0$ and $x_0 = T$ are equivalent.

4.1.1 Meson correlators

For meson states, which consist of one quark and one antiquark, the interpolating fields have the form

$$O(x) = \bar{\psi}(x)\Gamma\frac{\tau^a}{2}\psi(x), \tag{4.18}$$

where Γ is a combination of Dirac matrices chosen in such a way that $O(x)$ reproduces the same quantum numbers of the meson state under study. Moreover, ψ is a doublet of fermion fields in physical basis and the Pauli matrix τ^a acts on flavor space. Since here we make use of twisted mass Wilson fermions, we remind that at maximal twist the relation between physical and twisted basis is (see Eq. (3.58))

$$\psi = \frac{1+i\gamma_5\tau^3}{\sqrt{2}}\chi, \quad \bar{\psi} = \bar{\chi}\frac{1+i\gamma_5\tau^3}{\sqrt{2}}. \tag{4.19}$$

In the framework of the model considered in this work, i.e. QCD with two heavy degenerate charm quarks (see Section 3.8), we denote the physical and twisted doublets as

$$\psi = \begin{pmatrix} c_1 \\ c_2 \end{pmatrix}, \quad \chi = \begin{pmatrix} \tilde{c}_1 \\ \tilde{c}_2 \end{pmatrix}. \tag{4.20}$$

In Table 4.1 we report the most commonly used interpolators of the form (4.18) for the flavor components $\tau^{1,2}$ in physical and twisted basis, along with the name of the corresponding charmonium state (here we will focus only on the ground states).

To extract charmonium masses, we use zero-momentum correlation functions of the form

$$f_{O_1,O_2}(x_0,y_0) = -\frac{a^6}{L^3}\sum_{\vec{x},\vec{y}}\langle O_2(x)O_1^\dagger(y)\rangle \tag{4.21}$$

and we focus only on definite flavor assignments, e.g. $\mathcal{P}^+ \equiv \mathcal{P}^1 + i\mathcal{P}^2 = \bar{c}_1\gamma_5 c_2$. This choice allows to compute the two-point correlation functions only through the so-called *connected*

State	J^{PC}	Particle	Physical basis	Twisted basis
Scalar	0^{++}	χ_{c0}	$\mathcal{S}^{1,2} = \bar{\psi}\frac{\tau^{1,2}}{2}\psi$	$S^{1,2} = \bar{\chi}\frac{\tau^{1,2}}{2}\chi$
Pseudoscalar	0^{-+}	η_c	$\mathcal{P}^{1,2} = \bar{\psi}\gamma_5\frac{\tau^{1,2}}{2}\psi$	$P^{1,2} = \bar{\chi}\gamma_5\frac{\tau^{1,2}}{2}\chi$
Vector	1^{--}	J/ψ	$\mathcal{V}_i^{1,2} = \bar{\psi}\gamma_i\frac{\tau^{1,2}}{2}\psi$	$\pm A_i^{2,1} = \pm\bar{\chi}\gamma_i\gamma_5\frac{\tau^{2,1}}{2}\chi$
Axial vector	1^{++}	χ_{c1}	$\mathcal{A}_i^{1,2} = \bar{\psi}\gamma_i\gamma_5\frac{\tau^{1,2}}{2}\psi$	$\pm V_i^{2,1} = \pm\bar{\chi}\gamma_i\frac{\tau^{2,1}}{2}\chi$
Tensor	1^{+-}	h_c	$\mathcal{T}_{ij}^{1,2} = \bar{\psi}\gamma_i\gamma_j\frac{\tau^{1,2}}{2}\psi$	$T_{ij}^{1,2} = \bar{\chi}\gamma_i\gamma_j\frac{\tau^{1,2}}{2}\chi$

Table 4.1 Typical interpolators for meson states and relations between physical and twisted basis.

pieces. Indeed, integrating over the fermion fields one obtains

$$\begin{aligned}\langle \bar{c}_1(x)\Gamma c_2(x)\bar{c}_2(y)\Gamma c_1(y)\rangle_F &= \Gamma_{\alpha_1\beta_1}\Gamma_{\alpha_2\beta_2}\langle \bar{c}_1(x)_{\alpha_1 a_1} c_2(x)_{\beta_1 a_1}\bar{c}_2(y)_{\alpha_2 a_2} c_1(y)_{\beta_2 a_2}\rangle_F \\ &= -\Gamma_{\alpha_1\beta_1}\Gamma_{\alpha_2\beta_2}\langle c_2(x)_{\beta_1 a_1}\bar{c}_2(y)_{\alpha_2 a_2}\rangle_{c_2}\langle c_1(y)_{\beta_2 a_2}\bar{c}_1(x)_{\alpha_1 a_1}\rangle_{c_1} \\ &= -\Gamma_{\alpha_1\beta_1}\Gamma_{\alpha_2\beta_2} D_{c_2}^{-1}(x,y)_{\substack{\beta_1\alpha_2\\ a_1 a_2}} D_{c_1}^{-1}(y,x)_{\substack{\beta_2\alpha_1\\ a_2 a_1}} \\ &= -\mathrm{Tr}\left[\Gamma D_{c_2}^{-1}(x,y)\Gamma D_{c_1}^{-1}(y,x)\right],\end{aligned} \tag{4.22}$$

where the subscript $\langle \quad \rangle_F$ denotes the fermion integration and in the second and third line we have reordered the Grassmann variables and applied Wick's theorem. Contributions of the form $\mathrm{Tr}\left[\Gamma D_{c_2}^{-1}(x,y)\Gamma D_{c_1}^{-1}(y,x)\right]$ are called *connected pieces*, because the inverse of the Dirac operator $D_{c_2}^{-1}(x,y)$ propagates a c_2 quark from the coordinate y to the coordinate x, while $D_{c_1}^{-1}(y,x)$ propagates a c_1 quark in opposite direction. A graphic representation of Eq. (4.22) is reported in left-hand side of Figure 4.1. For correlators of the form $\langle \bar{c}_{1,2}(x)\Gamma c_{1,2}(x)\bar{c}_{1,2}(y)\Gamma c_{1,2}(y)\rangle$ (obtained using $a = 3$ in Eq. (4.18)), it is simple to show that after fermion integration we have

$$\begin{aligned}\langle \bar{c}_{1,2}(x)\Gamma c_{1,2}(x)\bar{c}_{1,2}(y)\Gamma c_{1,2}(y)\rangle_F = &-\mathrm{Tr}\left[\Gamma D_{c_{1,2}}^{-1}(x,y)\Gamma D_{c_{1,2}}^{-1}(y,x)\right] \\ &+\mathrm{Tr}\left[\Gamma D_{c_{1,2}}^{-1}(x,x)\right]\mathrm{Tr}\left[\Gamma D_{c_{1,2}}^{-1}(y,y)\right].\end{aligned} \tag{4.23}$$

The new terms that appear in the second line of Eq. (4.23) are called *disconnected pieces*, because the propagators $D_{c_{1,2}}^{-1}(x,x)$ and $D_{c_{1,2}}^{-1}(y,y)$ transport the $c_{1,2}$ quarks from a given space-time point back to the same point, as shown on the right hand side of Figure 4.1. Disconnected

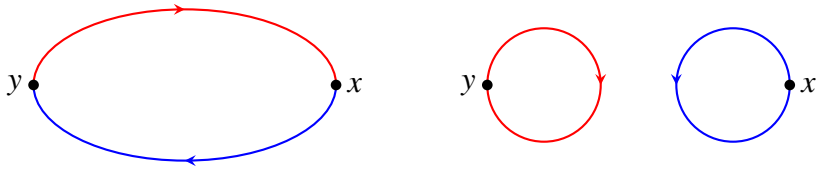

Figure 4.1 Schematic representation of connected (l.h.s) and disconnected (r.h.s) pieces of a meson correlator.

pieces require a larger computational effort with respect to the connected ones and this is the reason why we focus here only on interpolators of the type $\bar{c}_1\Gamma c_2$.

4.1.2 Stochastic sources

Looking at Eq. (4.13), we see that the projection to zero-momentum can be realized performing a sum either over $\vec{x}$ or $\vec{y}$. However, keeping the two sums typically leads to highly improved signal for the meson correlators and this is the reason of our choice (4.21), where the sum is performed both over $\vec{x}$ and $\vec{y}$. Switching to the twisted basis, this means that we need to compute objects like (see Eqs (3.97), (4.21) and (4.22))

$$\begin{aligned} f(x_0,y_0) &= -\frac{a^6}{L^3}\sum_{\vec{x},\vec{y}}\langle\langle\bar{\tilde{c}}_1(x)\Gamma_A\tilde{c}_2(x)\bar{\tilde{c}}_2(y)\bar{\Gamma}_B\tilde{c}_1(y)\rangle_F\rangle_G \\ &= \frac{a^6}{L^3}\sum_{\vec{x},\vec{y}}\langle \mathrm{Tr}\left[\Gamma_A S_2(x,y)\bar{\Gamma}_B S_1(y,x)\right]\rangle_G, \end{aligned} \tag{4.24}$$

where the subscripts $\langle\quad\rangle_G$ and $\langle\quad\rangle_F$ denote gluon and fermion integrations, $\Gamma_{A,B}$ are some matrices in spin space and the symbol $\bar{\Gamma}$ stands for $\bar{\Gamma}=\gamma_0\Gamma^\dagger\gamma_0$. $S_{1,2}$ are the twisted mass propagators (see Eq. (3.65)), which satisfy

$$\sum_y [D(x,y)+m_1+i\gamma_5\mu_1]S_1(y,z)=\mathbb{1}\delta_{x,z}, \tag{4.25}$$

$$\sum_y [D(x,y)+m_2-i\gamma_5\mu_2]S_2(y,z)=\mathbb{1}\delta_{x,z}. \tag{4.26}$$

In principle, the calculation of (4.24) would require $O(N^3)$ solutions of the Dirac equation and, as a consequence, a huge computational effort. However, the number of inversions can be dramatically reduced using stochastic methods (we refer to [57, 78] for an introduction). The idea is to introduce noise vectors $\vec{\eta}\in\mathbb{C}^{12N^3N_t}$ with the properties [89, 90]

$$\begin{aligned} \langle\eta_{\alpha a}(u)\rangle_\eta &= 0, \\ \langle\eta^\star_{\alpha a}(u)\eta_{\beta b}(v)\rangle_\eta &= \delta_{u_0,x_0}\delta_{v_0x_0}\delta_{\vec{u},\vec{v}}\delta_{\alpha\beta}\delta_{ab}, \end{aligned} \tag{4.27}$$

where u and v are two generic space-time points and $\langle\quad\rangle_\eta$ is the expectation value over the random noise sources. Note that the stochastic sources described in (4.27) are distributed on one specific time-slice. This technique is known in literature as *time-dilution* and reduces the variance of the observables at the same cost of N_{noise} random sources [91]. Popular choices for noise vectors are $\eta_{\alpha a}\in Z_4=\{1,i,-1,-i\}$ and $\eta_{\alpha a}\in U(1)$. Any choice satisfying Eq. (4.27) allows to evaluate the trace over $\vec{x}$, α, a of a matrix A as

$$\mathrm{Tr}_{\vec{x},\alpha,a}[A]=\langle\eta^\dagger A\eta\rangle_\eta. \tag{4.28}$$

In addition, it is convenient to define two derived stochastic quantities

$$\zeta(y)=\sum_u [D+m_1+i\gamma_5\mu_1]^{-1}(y,u)\eta(u)=\sum_u S_1(y,u)\eta(u), \tag{4.29}$$

$$\begin{aligned}\xi(y) &= \sum_v [D+m_2+i\gamma_5\mu_2]^{-1}(u,v)\gamma_5\Gamma_A^\dagger\eta(v)\\ \gamma_5\xi(y) &= \sum_v S_2^\dagger(y,v)\Gamma_A^\dagger\eta(v),\end{aligned} \tag{4.30}$$

where in the second line of (4.30) we use the property of the twisted mass Dirac operator

$$\gamma_5[D+m+i\gamma_5\mu]\gamma_5 = [D+m-i\gamma_5\mu]^\dagger. \tag{4.31}$$

Doing so, we can rewrite Eq. (4.24) as

$$\begin{aligned}f(x_0,y_0) &= \frac{a^6}{L^3}\sum_{\vec{x},\vec{y}}\langle\langle\eta^\dagger(x)\Gamma_A S_2(x,y)\bar{\Gamma}_B S_1(y,x)\eta(x)\rangle_\eta\rangle_G\\ &= \frac{a^6}{L^3}\sum_{\vec{y}}\sum_{u,v}\langle\langle\eta^\dagger(v)\Gamma_A S_2(v,y)\bar{\Gamma}_B S_1(y,u)\eta(u)\rangle_\eta\rangle_G\\ &= \frac{a^6}{L^3}\sum_{\vec{y}}\langle\langle\xi^\dagger(y)\gamma_5\bar{\Gamma}_B\zeta(y)\rangle_\eta\rangle_G = \frac{a^6}{L^3}\sum_{\vec{y}}\langle\langle(\bar{\Gamma}_B^\dagger\gamma_5\xi(y))^\dagger\zeta(y)\rangle_\eta\rangle_G.\end{aligned} \tag{4.32}$$

This means that the meson correlation function (4.24) can be evaluated at a cost of two inversions per stochastic vector and gauge field configuration. In the pseudoscalar channel $\Gamma_A = \gamma_5$, therefore if $m_1 = m_2$ and $\mu_1 = \mu_2$ only one inversion per noise vector is required, because $\xi = \zeta$.

The strategy above can be summarized as follows:

1. for each gauge configuration create N_{noise} random vectors;
2. with each vector calculate both ζ and ξ;
3. calculate $\sum_{\vec{y}}(\bar{\Gamma}_B^\dagger\gamma_5\xi(y))^\dagger\zeta(y)$ for each gauge field and noise vector;
4. after averaging over the noise vectors, carry out the autocorrelation analysis with respect to the gauge field average as explained in Section 3.5.1.
5. extract meson masses from the weighted plateau average (4.17) of the effective mass (4.15).

4.1.3 Mass derivatives

In some cases, it can be useful to compute the derivatives of the correlators (4.24) with respect to the bare mass m_1, m_2 or bare twisted mass μ_1, μ_2. We can still use (4.32) to write [89, 90]

$$\frac{\partial f(x_0,y_0)}{\partial m_1} = \frac{a^6}{L^3}\sum_{\vec{y}}\left\langle\left\langle\left(\bar{\Gamma}_B^\dagger\gamma_5\xi(y)\right)^\dagger\frac{\partial\zeta(y)}{\partial m_1}\right\rangle_\eta\right\rangle_G, \tag{4.33}$$

$$\frac{\partial f(x_0,y_0)}{\partial m_2} = \frac{a^6}{L^3}\sum_{\vec{y}}\left\langle\left\langle\left(\bar{\Gamma}_B^\dagger\gamma_5\frac{\partial\xi(y)}{\partial m_2}\right)^\dagger\zeta(y)\right\rangle_\eta\right\rangle_G, \tag{4.34}$$

$$\frac{\partial f(x_0,y_0)}{\partial \mu_1} = \frac{a^6}{L^3}\sum_{\vec{y}}\left\langle\left\langle\left(\bar{\Gamma}_B^\dagger\gamma_5\xi(y)\right)^\dagger\frac{\partial\zeta(y)}{\partial \mu_1}\right\rangle_\eta\right\rangle_G, \tag{4.35}$$

$$\frac{\partial f(x_0,y_0)}{\partial \mu_2} = \frac{a^6}{L^3}\sum_{\vec{y}}\left\langle\left\langle\left(\bar{\Gamma}_B^\dagger\gamma_5\frac{\partial\xi(y)}{\partial \mu_2}\right)^\dagger\zeta(y)\right\rangle_\eta\right\rangle_G, \tag{4.36}$$

with

$$\frac{\partial\zeta}{\partial m_1} = -[D+m_1+i\gamma_5\mu_1]^{-2}\eta, \tag{4.37}$$

$$\frac{\partial\xi}{\partial m_2} = -[D+m_2+i\gamma_5\mu_2]^{-2}\gamma_5\Gamma_A^\dagger\eta, \tag{4.38}$$

$$\frac{\partial\zeta}{\partial \mu_1} = -i[D+m_1+i\gamma_5\mu_1]^{-1}\gamma_5[D+m_1+i\gamma_5\mu_1]^{-1}\eta, \tag{4.39}$$

$$\frac{\partial\xi}{\partial \mu_2} = -i[D+m_2+i\gamma_5\mu_2]^{-1}\gamma_5[D+m_2+i\gamma_5\mu_2]^{-1}\gamma_5\Gamma_A^\dagger\eta. \tag{4.40}$$

To compute the derivatives above we need twice as many inversions as for the computation of the correlators themselves. Indeed

$$\frac{\partial\zeta}{\partial m_1} = -[D+m_1+i\gamma_5\mu_1]^{-1}\zeta, \tag{4.41}$$

$$\frac{\partial\xi}{\partial m_2} = -[D+m_2+i\gamma_5\mu_2]^{-1}\xi, \tag{4.42}$$

$$\frac{\partial\zeta}{\partial \mu_1} = -i[D+m_1+i\gamma_5\mu_1]^{-1}\gamma_5\zeta, \tag{4.43}$$

$$\frac{\partial\xi}{\partial \mu_2} = -i[D+m_2+i\gamma_5\mu_2]^{-1}\gamma_5\xi. \tag{4.44}$$

If ξ and ζ are already known from the computation of (4.32), the computational effort is reduced by a factor two.

4.2 Decay constants

So far we have discussed how to extract meson masses from two point correlation functions. Another set of observables that can be determined from the same correlators are the meson decay constants, that are related to matrix elements between the meson state of interest and

the vacuum. They play an important role in Particle Physics, as they are strictly related to weak decay properties of a meson.

In our model, QCD with $N_f = 2$ degenerate charm quarks, we can define the decay constant f_{η_c} of a pseudoscalar meson η_c with momentum q_μ as [92]

$$\langle O|\mathcal{A}_\mu^+(x)|\eta_c(q)\rangle \equiv i f_{\eta_c} q_\mu e^{-iq\cdot x}, \tag{4.45}$$

with

$$\mathcal{A}_\mu^+(x) = \mathcal{A}_\mu^1(x) + i\mathcal{A}_\mu^2(x) = \bar{c}_1(x)\gamma_\mu\gamma_5 c_2(x). \tag{4.46}$$

If we take the divergence of (4.45) it is easy to show that

$$\langle 0|\partial^\mu \mathcal{A}_\mu^+(0)|\eta_c(q)\rangle = f_{\eta_c} m_{\eta_c}^2, \tag{4.47}$$

where m_{η_c} is the mass of the meson η_c. In a similar way we can define the decay constant $f_{J/\psi}$ of the vector meson J/ψ at rest as [93]

$$\frac{1}{3}\sum_{i=1}^{3}\langle 0|\mathcal{V}_i^+(0)|J/\psi\rangle = f_{J/\psi} m_{J/\psi}, \tag{4.48}$$

where

$$\mathcal{V}_i^+(x) = \mathcal{V}_i^1(x) + i\mathcal{V}_i^2(x) = \bar{c}_1\gamma_i c_2(x) \tag{4.49}$$

and $m_{J/\psi}$ denotes the mass of the meson J/ψ.

Since in this work we study tmQCD on a lattice, it is convenient to express the definitions (4.47) and (4.48) in a Euclidean space-time and write the interpolators in the twisted basis. At maximal twist, $\omega = \pi/2$, the left hand side of (4.47) becomes

$$\begin{aligned}\langle 0|\partial_\mu \mathcal{A}_\mu^+|\eta_c\rangle &= \langle 0|\partial_\mu V_\mu^2 - i\partial_\mu V_\mu^1|\eta_c\rangle = 2\mu\langle 0|P^1 + iP^2|\eta_c\rangle \\ &= 2\mu\langle 0|P^+|\eta_c\rangle = 2\mu\langle 0|\bar{\tilde{c}}_1\gamma_5\tilde{c}_2|\eta_c\rangle,\end{aligned} \tag{4.50}$$

where in the first line we used the PCVC relation (3.74). Therefore, the definition of f_{η_c} in twisted basis reads

$$2\mu\langle 0|P^+(0)|\eta_c(q)\rangle = 2\mu\langle 0|\bar{\tilde{c}}_1(0)\gamma_5\tilde{c}_2(0)|\eta_c(q)\rangle = f_{\eta_c} m_{\eta_c}^2. \tag{4.51}$$

Using similar arguments, one can show that, up to a non-relevant phase factor, the vector decay constant in twisted basis is

$$\frac{1}{3}\sum_{i=1}^{3}\langle 0|A_i^+|J/\psi\rangle = \frac{1}{3}\sum_{i=1}^{3}\langle 0|\bar{\tilde{c}}_1(0)\gamma_i\gamma_5\tilde{c}_2(0)|J/\psi\rangle = f_{J/\psi} m_{J/\psi}. \tag{4.52}$$

The twisted mass formulation of QCD is a particularly convenient setup for the pseudoscalar decay constant f_{η_c}, because the renormalization factors Z_P and Z_μ obey $Z_P Z_\mu = 1$. Therefore the lattice calculation of f_{η_c} does not need any renormalization factors, as already discuss

in Ref. [94]. As concerns $f_{J/\psi}$, the relevant matrix element must be multiplied by the renormalization factor Z_A.

We conclude this section observing that the normalization in the continuum of the states of Eqs. (4.45) and (4.48) is defined in the standard way

$$\langle \vec{p}|\vec{q}\rangle = 2E(\vec{p})(2\pi)^3\delta^3(\vec{p}-\vec{q}), \tag{4.53}$$

where the combination $2E(\vec{p})\delta^3(\vec{p}-\vec{q})$ is Lorentz invariant. When working on the lattice, the integral $\int d^3p$ is replaced by $(\frac{2\pi}{L})^3\sum_n$, therefore the lattice counterpart of $\delta^3(\vec{p}-\vec{q})$ is $\left(\frac{L}{2\pi}\right)^3\delta_{\vec{p},\vec{q}}$. Thus, to be consistent with Eq. (4.53), the lattice normalization of the states is

$$\langle \vec{p}|\vec{q}\rangle = 2E(\vec{p})L^3\delta_{\vec{p},\vec{q}}. \tag{4.54}$$

4.2.1 Extraction of matrix elements

Since we use open boundary conditions in the time direction, computing the meson decay constant through an exponential fit to the two-point correlation function may lead to unreliable results, because of the boundary effects. As a first attempt, one could place source and sink positions in the middle of the lattice to make the boundary effects negligible and compute the decay constant from the exponential decay of the two-point correlation function, see Eq. (4.13). This approach can potentially bring advantages, provided that the additional contributions of the excited states do not reduce too much the remaining portion of the lattice needed to extract the meson decay constants. For this reason, we follow here the method described in Refs. [80, 95], whose advantage is to remove the unwanted boundary effects from our lattice calculation by forming a suitable ratio of two-point correlation functions.

To understand how this method works, let us first write the relevant matrix elements in Eqs. (4.51) and (4.52) as

$$\langle 0|X^+(0)|\sigma\rangle, \quad \text{with } X^+ = P^+, A_i^+ \text{ and } |\sigma\rangle = |\eta_c\rangle, |J/\psi\rangle \tag{4.55}$$

and study in detail the two-point correlation function

$$f_X(x_0,y_0) = -\frac{a^6}{L^3}\sum_{\vec{x},\vec{y}}\langle X^+(x)X^-(y)\rangle_T. \tag{4.56}$$

To simplify as much as possible the notation, for the time being we denote the eigenstates of the Hamiltonian as

$$\hat{H}|\alpha,l\rangle = E_l^\alpha|\alpha,l\rangle, \quad \mathbb{1} = \sum_{\alpha,l}|\alpha,l\rangle\langle\alpha,l|, \tag{4.57}$$

assuming the normalization of the states

$$\langle\alpha,l|\beta,m\rangle = \delta_{\alpha\beta}\delta_{lm}. \tag{4.58}$$

In Eq. (4.57) l indicates the energy levels and α any other quantum number. We omit the momentum $\vec{p}$ from the notation for two reasons:

1. in this work we focus only on zero-momentum states;
2. the boundary states $|\Omega\rangle$ are invariant under spatial translations, therefore

$$\langle\Omega|\vec{p}\rangle \neq 0 \text{ only if } \vec{p} = \vec{0}. \tag{4.59}$$

Keeping this in mind and repeating some of the calculations already seen in Section 4.1, it is easy to show that in the limit of large T

$$f_X(x_0,y_0) = -\sum_{\substack{\alpha,\beta\\ l,m}} \frac{\langle\Omega|\alpha,l\rangle}{\langle\Omega|0,0\rangle} e^{-E_l^\alpha(T-x_0)} \langle\alpha,l|\hat{X}^+(0)|\beta,m\rangle e^{-E_m^\beta(x_0-y_0)} \langle\beta,m|\phi_\sigma(y_0)\rangle, \tag{4.60}$$

with

$$|\phi_\sigma(y_0)\rangle = L^3 \sum_{\gamma,n} \hat{X}^-(0)|\gamma,n\rangle e^{-E_n^\gamma y_0} \frac{\langle\gamma,n|\Omega\rangle}{\langle 0,0|\Omega\rangle}, \quad \langle\beta,m|\phi_\sigma(y_0)\rangle = \delta_{\sigma\beta}\langle\sigma,n|\phi_\sigma(y_0)\rangle. \tag{4.61}$$

In the two equations above $|0,0\rangle$ stands for the vacuum and we assume energies normalized relative to the energy E_0^0 of the vacuum (therefore $E_0^0 = 0$). Since the boundary state $|\Omega\rangle$ has overlap only with states having $\alpha = 0$, i.e. the vacuum quantum numbers, we can simplify Eqs. (4.60) and (4.61) and write

$$f_X(x_0,y_0) = -\sum_{\beta,l,m} \frac{\langle\Omega|0,l\rangle}{\langle\Omega|0,0\rangle} e^{-E_l^0(T-x_0)} \langle 0,l|\hat{X}^+(0)|\beta,m\rangle e^{-E_m^\beta(x_0-y_0)} \langle\beta,m|\phi_\sigma(y_0)\rangle, \tag{4.62}$$

with

$$|\phi_\sigma(y_0)\rangle = L^3 \sum_{n} \hat{X}^-(0)|0,n\rangle e^{-E_n^0 y_0} \frac{\langle 0,n|\Omega\rangle}{\langle 0,0|\Omega\rangle}, \quad \langle\beta,m|\phi_\sigma(y_0)\rangle = \delta_{\sigma\beta}\langle\sigma,n|\phi_\sigma(y_0)\rangle. \tag{4.63}$$

We study now the case $x_0 - y_0 \to \infty$ of Eq. (4.62). In this limit, the only remaining term in the sum over the states $|\beta,m\rangle$ is $|\sigma,0\rangle$ and we obtain

$$f_X(x_0,y_0) = -\sum_{l} \frac{\langle\Omega|0,l\rangle}{\langle\Omega|0,0\rangle} e^{-E_l^0(T-x_0)} \langle 0,l|\hat{X}^+(0)|\sigma,0\rangle e^{-m_\sigma(x_0-y_0)} \langle\sigma,0|\phi_\sigma(y_0)\rangle, \tag{4.64}$$

where $E_0^\sigma = m_\sigma$ is the mass of the lowest energy state $|\sigma,0\rangle$. To extract the matrix element (4.55), it is convenient to consider also the correlators

$$L^3 f_X(T-y_0,y_0) = e^{-m_\sigma(T-2y_0)} |\langle\sigma,0|\phi_\sigma(y_0)\rangle|^2, \tag{4.65}$$

$$f_X(T-x_0,y_0) = -\sum_{l} \frac{\langle\Omega|0,l\rangle}{\langle\Omega|0,0\rangle} e^{-E_l^0 x_0} \langle 0,l|\hat{X}^+(0)|\sigma,0\rangle e^{-m_\sigma(T-x_0-y_0)} \langle\sigma,0|\phi_\sigma(y_0)\rangle. \tag{4.66}$$

When x_0 is far enough from the boundaries ($0 \ll x_0 \ll T$), Eqs. (4.64) and (4.66) are only given by the term of the sum with $l = 0$ and they read

$$f_X(x_0, y_0) = -\langle 0,0|\hat{X}^+(0)|\sigma,0\rangle e^{-m_\sigma(x_0-y_0)}\langle \sigma,0|\phi_\sigma(y_0)\rangle, \tag{4.67}$$

$$f_X(T-x_0, y_0) = -\langle 0,0|\hat{X}^+(0)|\sigma,0\rangle e^{-m_\sigma(T-x_0-y_0)}\langle \sigma,0|\phi_\sigma(y_0)\rangle. \tag{4.68}$$

Thus, the matrix element of interest can be extracted through the following combination of correlators

$$\langle 0,0|\hat{X}^+(0)|\sigma,0\rangle = \sqrt{\frac{|f_X(x_0,y_0)f_X(T-x_0,y_0)|}{L^3 f_X(T-y_0,y_0)}}. \tag{4.69}$$

If we want to use the Lorentz invariant normalization of the states (4.54), we must replace $|\sigma,0\rangle \to |\sigma,0\rangle/(\sqrt{2m_\sigma L^3})$ and we can conclude that

$$\frac{\langle 0,0|\hat{X}^+(0)|\sigma,0\rangle}{\sqrt{2m_\sigma}} = \sqrt{\frac{|f_X(x_0,y_0)f_X(T-x_0,y_0)|}{f_X(T-y_0,y_0)}} \equiv R_X(x_0,y_0). \tag{4.70}$$

The main advantage of this approach is that there are no restrictions in the position of the source y_0, so even choices of y_0 very close to the boundaries reproduce correct results. Note that Eq. (4.70) is satisfied for a large range of sink positions $0 \ll x_0 \ll T$, where boundary effects and excited state contributions can be neglected, thus an improved estimate of the relevant matrix element is the plateau average

$$R_X^{av} \equiv \frac{1}{t_f - t_i + 1}\sum_{x_0=t_i}^{t_f} R_X(x_0,y_0) = \frac{\langle 0,0|\hat{X}^+(0)|\sigma,0\rangle}{\sqrt{2m_\sigma}}, \tag{4.71}$$

where t_i and t_f are the start and the end of the plateau. Therefore, to compute the pseudoscalar and vector decay constants f_{η_c} and $f_{J/\psi}$ we will make use of the following relations (see Eqs. (4.71), (4.51) and (4.52))

$$f_{\eta_c} = 2\mu R_P^{av}\sqrt{\frac{2}{m_{\eta_c}^3}} \qquad (Z_P Z_\mu = 1), \tag{4.72}$$

$$f_{J/\psi} = Z_A\left(\frac{1}{3}\sum_{i=1}^{3} R_{A_i}^{av}\right)\sqrt{\frac{2}{m_{J/\psi}}}. \tag{4.73}$$

The meson masses $m_{J/\psi}$ and m_{η_c}, in turn, can be estimated through the weighted plateau average of the effective mass, see Eq. (4.17).

4.3 Wilson loops

One of the main features of QCD is the appearance of a confining potential. The static potential allows to study the properties of QCD from small to large distances and offers the possibility to probe charm loop effects at different energy scales.

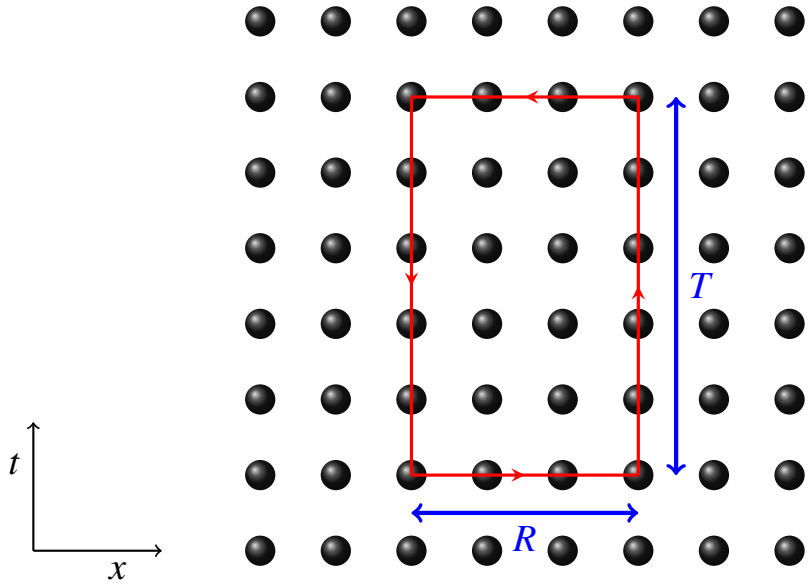

Figure 4.2 Example of a rectangular Wilson loop in the $t-x$ plane.

4.3.1 QCD static potential

In Lattice QCD the static potential between static color sources can be extracted, for instance, from the expectation values of Wilson loops (see [54] for a detailed proof). They are traces of ordered products of link variables along a rectangular path, whose sides of length T and R (in lattice units) lie on the time direction and one spatial direction respectively (see Figure 4.2). In the limit of infinite time separation, $T \to \infty$, the static potential $V(r)$ at a distance $r = Ra$ is given by

$$aV(r) = -\lim_{T\to\infty} \frac{1}{T} \log(\langle W(R,T)\rangle), \tag{4.74}$$

where the triangular brackets $\langle \quad \rangle$ denote the expectation value of a Wilson loop $W(R,T)$ of sizes R and T. In the literature it is possible to find several references where the shape of the static potential has been studied making use of Wilson loops (see for instance [96] for $N_f = 0$ QCD and [97] for $N_f = 2+1$ QCD). From these previous investigations, we know that at intermediate distances $V(r)$ can be described by the phenomenological Cornell parametrization [98]

$$V(r) = A + \frac{B}{r} + \sigma r, \tag{4.75}$$

where A is a constant that originates from an irrelevant normalization of the energy and B/r is a pure Coulomb term with strength B. At large separations the potential is dominated by the linear term σr, where σ is a constant called *string tension*. It has been found experimentally that the physical value of σ is around $1\text{GeV}/\text{fm}$.

4.3.2 Strong coupling α_{qq}

Starting from $V(r)$, it is also possible to define a strong coupling α_V. However, since the static potential is defined up to a constant, which corresponds to the unphysical self energy contribution of the static sources, it is better to define a non-perturbative strong coupling

through the static force $F(r) = dV(r)/dr \equiv V'(r)$

$$\alpha_{qq} = \frac{g_{qq}^2}{4\pi} \equiv \frac{1}{C_F} r^2 F(r), \tag{4.76}$$

where $C_F = 4/3$ for $SU(3)$ gauge theories. In the static force the additive renormalization of V cancels out. The static force $F(r)$ can also be used to define the hadronic scale r_0 [49], by the relation

$$r^2 F(r)|_{r=r_0} = 1.65. \tag{4.77}$$

The physical value is around $r_0 \approx 0.5$ fm [99].

Eq. (4.76) is the definition of α_{qq} in the continuum, therefore if we are interested in measuring this quantity on a lattice, first of all we need a lattice regularization of the derivative $V'(r)$. Even though

$$F(r_{naive}) = \frac{V(Ra) - V(Ra-a)}{a}, \quad \frac{r_{naive}}{a} = R - \frac{1}{2} \tag{4.78}$$

seems to be the most natural choice, it has been shown [96, 49] that an improved definition is

$$F(r_I) = \frac{V(Ra) - V(Ra-a)}{a} = C_F \frac{g^2}{4\pi r_I^2} + O(g^4 a^2). \tag{4.79}$$

The distance r_I is chosen such that the static force has no cutoff effects at the tree-level in perturbation theory. In this work we use the improved distances r_I for HYP2-smeared links (see Section 4.4) provided in Table 2 of Ref. [100].

The running of the coupling g_{qq} is described by the Renormalization Group β_{qq}-function

$$\beta_{qq} \equiv -r \frac{\partial g_{qq}}{\partial r}. \tag{4.80}$$

Its perturbative expansion in powers of g_{qq} is known up to 4 loops [100–105] and is given by

$$\begin{aligned} \beta_{qq} = &- g_{qq}^3 \left[b_0^{(qq)} + b_1^{(qq)} g_{qq}^2 + b_2^{(qq)} g_{qq}^4 + \left(b_3^{(qq)} + b_{3,\text{IR}}^{(qq)} \log\left(\frac{3 g_{qq}^2}{8\pi} \right) + \right) g_{qq}^6 \right] \\ &+ O(g_{qq}^{11}), \end{aligned} \tag{4.81}$$

where the resummation of infrared divergence at 4 loops gives rise to the logarithmic term $b_{3,\text{IR}}^{(qq)} \log\left(\frac{3g_{qq}^2}{8\pi}\right)$. For an $SU(3)$ gauge theory with N_f massless quarks, the first two coefficients $b_0^{(qq)} = b_0$ and $b_1^{(qq)} = b_1$ do not depend on the renormalization scheme and are given in (2.25).

The other coefficients are scheme dependent. In the qq-scheme they are

$$\begin{aligned} b_2^{(qq)} &= \frac{1}{(4\pi)^3}(1.6524 - 0.28933N_f + 0.00527N_f^2 + 0.00011N_f^3), \\ b_3^{(qq)} &= \frac{1}{(4\pi)^4}(4.94522 - 1.07965N_f + 0.079107N_f^2 - 0.002774N_f^3 + 0.000051N_f^4), \\ b_{3,\mathrm{IR}}^{(qq)} &= \frac{1}{(4\pi)^4}(1.25385 - 0.07599N_f). \end{aligned} \tag{4.82}$$

4.4 Smearing techniques

The main difficulties that arise in Wilson loop measurements come from the exponential decay of the signal with the area of the loop, while the variance stays approximately constant. Thus, to improve the signal-to-noise ratio of the static potential at large distances, we make use of the *HYP smearing* method [106]. Such technique leads to a significant increase of the statistical precision when extracting the static potential from Wilson loop measurements.

4.4.1 APE smearing

Smearing techniques usually consist in replacing a link variable $U_\mu(n)$ with local averages over short paths that connect the endpoints of $U_\mu(n)$. They are in general used to reduce the contamination by excited states and smooth the fluctuations of the gauge field.

One of the simplest smearing algorithms is the so-called *APE smearing* [107]. In this case the original link is replaced by

$$U_\mu(n) \to V_\mu(n) = (1-\alpha)U_\mu(n) + \frac{\alpha}{6}\sum_{\nu\neq\mu} C_{\mu\nu}(n), \tag{4.83}$$

where $C_{\mu\nu}$ is the sum of the *staples*

$$\begin{aligned} C_{\mu\nu}(n) = {} & U_\nu(n)U_\mu(n+\hat{\nu})U_\nu(n+\hat{\mu})^\dagger \\ & + U_\nu(n-\hat{\nu})^\dagger U_\mu(n-\hat{\nu})U_\nu(n-\hat{\nu}+\hat{\mu}) \end{aligned} \tag{4.84}$$

and α is a parameter to tune depending on the problem at hand. A graphic representation

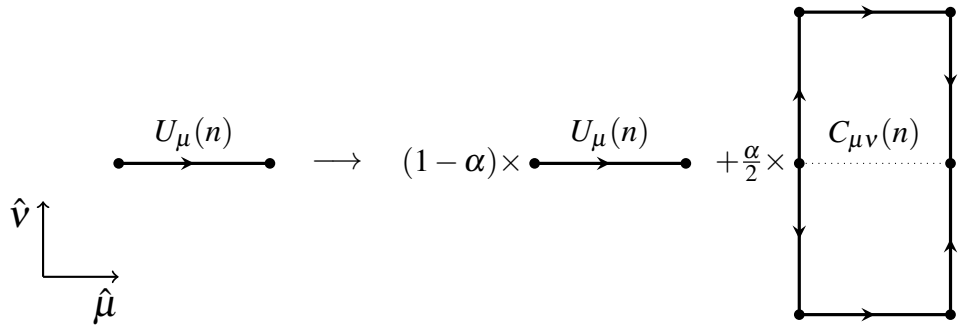

Figure 4.3 Example of APE smearing in the two dimensional case.

of the APE-smeared link (4.83) is reported in Figure 4.3 in the two dimensional case. Note

that the smeared link $V_\mu(n)$ is not an element of the group $SU(3)$, because the sum of $SU(3)$ matrices does not belong to the group $SU(3)$. Therefore, to obtain an $SU(3)$ element one has to project back $V_\mu(n)$ to $SU(3)$:

$$V_\mu(n) \to \mathrm{Proj}_{SU(3)}[V_\mu(n)]. \tag{4.85}$$

The way to do that is not unique and many algorithms for the $SU(3)$ projection have been developed. In this thesis, we use the iterative method described in Ref. [108]. It consists in replacing

$$V_\mu(n) \to \frac{V_\mu(n)}{\sqrt{\mathrm{Tr}[V_\mu(n)V_\mu(n)^\dagger]/3}}, \tag{4.86}$$

followed by n_{iter} iterations of

$$V_\mu(n) \to X\left(1 - \frac{i}{3}\mathrm{Im}(\det[X])\right), \quad \text{with } X = V_\mu(n)\left(\frac{3}{2} - \frac{1}{2}V_\mu(n)^\dagger V_\mu(n)\right). \tag{4.87}$$

After a few iterations, the deviations from $SU(3)$ are usually very small. Here we choose $n_{iter} = 4$, as suggested in Ref. [108].

4.4.2 HYP smearing

In the HYP smearing [106] the link $U_\mu(n)$ is replaced by the average of paths that lie within hypercubes attached to the original link. The algorithm can be reconstructed through three levels of modified APE smearing. In the first level, one constructs *decorated links* starting from the original links via

$$\begin{aligned} &\bar{V}_{\mu;\nu\rho}(n) = (1-\alpha_3)U_\mu(n) + \frac{\alpha_3}{2}\sum_{\pm\eta\neq\rho,\mu,\nu} U_\eta(n)U_\mu(n+\hat{\eta})U_\eta(n+\hat{\mu})^\dagger, \\ &\bar{V}_{\mu;\nu\rho}(n) \to \mathrm{Proj}_{SU(3)}[\bar{V}_{\mu;\nu\rho}(n)]. \end{aligned} \tag{4.88}$$

Then, in the second step *higher decorated links* $\tilde{V}_{\mu;\nu}(n)$ are built up from the previous $\bar{V}_{\mu;\nu\rho}(n)$ according to

$$\begin{aligned} &\tilde{V}_{\mu;\nu}(n) = (1-\alpha_2)U_\mu(n) + \frac{\alpha_2}{4}\sum_{\pm\rho\neq\mu,\nu} \bar{V}_{\rho;\nu\mu}(n)\bar{V}_{\mu;\rho\nu}(n+\hat{\rho})\bar{V}_{\rho;\nu\mu}(n+\hat{\mu})^\dagger, \\ &\tilde{V}_{\mu;\nu}(n) \to \mathrm{Proj}_{SU(3)}[\tilde{V}_{\mu;\nu}(n)]. \end{aligned} \tag{4.89}$$

Finally, in the last level the HYP-smeared links $V_\mu(n)$ are constructed through

$$\begin{aligned} &V_\mu(n) = (1-\alpha_1)U_\mu(n) + \frac{\alpha_1}{6}\sum_{\pm\nu\neq\mu} \tilde{V}_{\nu;\mu}(n)\tilde{V}_{\mu;\nu}(n+\hat{\nu})\tilde{V}_{\nu;\mu}(n+\hat{\mu})^\dagger, \\ &V_\mu(n) \to \mathrm{Proj}_{SU(3)}[V_\mu(n)]. \end{aligned} \tag{4.90}$$

A graphical representation of the HYP smearing algorithm in the three dimensional case is shown in Figure 4.4.

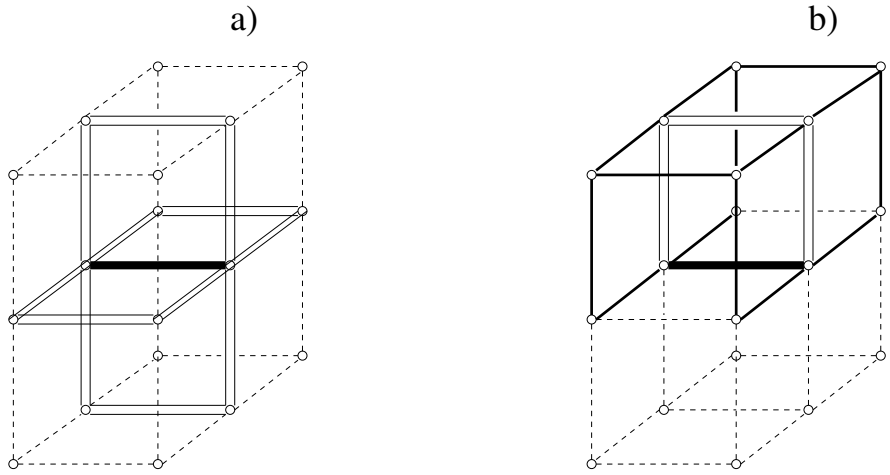

Figure 4.4 Example of HYP smearing in the three dimensional case [106]: a) The HYP-smeared link is built from staples of decorated (double-lined) links; b) Each decorated link is built from two staples which lie in hypercubes attached to the original link.

Usual choices of the HYP-smearing parameters α_1, α_2, α_3 are

$$\begin{cases} \text{HYP1} : \alpha_1 = 0.75, & \alpha_2 = 0.60 & \alpha_3 = 0.30; \\ \text{HYP2} : \alpha_1 = 1.00, & \alpha_2 = 1.00 & \alpha_3 = 0.50. \end{cases} \tag{4.91}$$

The HYP1 parameters correspond to a maximization of the average of the smallest plaquette [106], while the HYP2 ones minimize the one-loop coefficient of the $1/a$ self-energy contribution of a static quark [108, 109]. In Ref. [100] it has been observed that choosing HYP2 parameters produces a static potential with a slightly better signal-to-noise ratio and therefore this will be our choice for the smearing HYP parameters in the rest of this thesis.

4.5 Static-charm mesons

In QCD with $N_f = 2$ degenerate charm quarks, we expect that at a certain distance r_{sb} the energy stored in the string connecting a pair of heavy quark and antiquark is enough to create a charm-anticharm pair. The latter combines with the static quark-antiquark pair, producing a pair of static-charm mesons (bound state made of a static quark (antiquark) and a charm antiquark (quark)). This kind of transition is known as *string breaking*. Lattice studies of this phenomenon can be found for instance in Refs. [110–114]. The main difficulties in the study of these string breaking phenomena come from the poor overlap between Wilson loops and the lowest state of a pair of static-light (static-charm in our case) mesons. One needs to construct a correlation matrix whose diagonal elements describe a pure string-like state (Wilson loop) and two static-light mesons, whilst the off-diagonal elements describe the transition between a string-like state and a state made of two static-light mesons. In this thesis we will not use such techniques, thus we refer to [114] further details.

To estimate r_{sb} we will fit the potential at distances much smaller than r_{sb} (which can be extracted from Wilson loops alone) to a Cornell potential (4.75). Then we determine r_{sb} such

that $V_{\text{fitted}}(r_{sb}) = 2M_{ps}$, where M_{ps} is the ground state of the static-charm spectrum. Notice that this determination of r_{sb} is analogous to the one adopted in [114]. To this aim, we study the correlation function of a static-charm meson, which is given by

$$\begin{aligned} f(x_0,y_0) &= -\langle\langle \bar{c}_1(x_0,\vec{x})\gamma_5 h(x_0,\vec{x})\bar{h}(y_0,\vec{x})\gamma_5 c_1(y_0,\vec{x})\rangle_F\rangle_G \\ &= \langle \mathrm{Tr}[\gamma_5 S^\dagger_{\vec{x}}(x_0-y_0)P_+\gamma_5 D^{-1}_{c_1}(y_0,\vec{x};x_0,\vec{x})]\rangle_G, \quad P_+ = \frac{1+\gamma_0}{2}. \end{aligned} \tag{4.92}$$

In the equation above h denotes a static quark field and its propagator is given by $S^\dagger_{\vec{x}}(x_0-y_0)P_+$ [115], where $S^\dagger_{\vec{x}}(x_0-y_0)$ is the timelike Wilson-line

$$S^\dagger_{\vec{x}}(x_0-y_0) = U_0(y_0,\vec{x})U_0(y_0+a,\vec{x})\ldots U_0(x_0-a,\vec{x}). \tag{4.93}$$

A graphical representation of the static-charm correlator is shown in Figure 4.5.

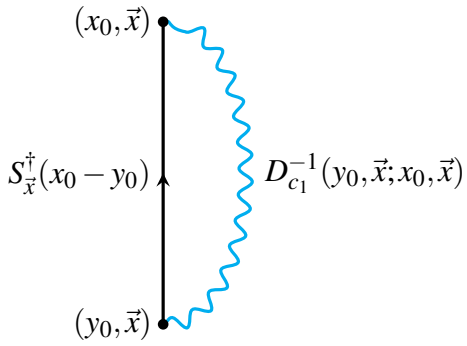

Figure 4.5 Sketch of a static-charm meson correlator.

In twisted basis ($\omega = \pi/2$), the correlator (4.92) becomes

$$f(x_0,y_0) = \frac{1}{2}\langle \mathrm{Tr}[(-\gamma_0+i\gamma_5)S^\dagger_{\vec{x}}(x_0-y_0)D^{-1}_{\tilde{c}_1}(y_0,\vec{x};x_0,\vec{x})]\rangle_G. \tag{4.94}$$

The temporal gauge links of $S^\dagger_{\vec{x}}(x_0-y_0)$ are HYP2-smeared (see Section 4.4) so that the static potential obtained from our Wilson loop measurements has the same static-self energy as $2M_{ps}$. To compute the static-charm correlator (4.94), we use the so-called *point sources*

$$S_0^{(m_0,\alpha_0,a_0)}(m)_{\alpha a} = \delta_{mm_0}\delta_{\alpha\alpha_0}\delta_{aa_0}, \tag{4.95}$$

which allow to determine the *point-to-all propagator*

$$D^{-1}_{\tilde{c}_1}(n,m_0)^{\beta\alpha_0}_{ba_0} = \sum_{m,\alpha,a} D^{-1}(n,m)^{\beta\alpha}_{ba} S_0^{(m_0,\alpha_0,a_0)}(m)_{\alpha a} \tag{4.96}$$

from a generic fixed source at m_0 to any site of the lattice. Such calculation requires twelve inversions per point source, one for each value of spin (α_0) and color (a_0) indices. To improve the accuracy of the correlator, one can use a number N_{src} of random source positions and average the signal over the N_{src} point sources. From the correlator (4.94) we can extract M_{PS} through the plateau average (4.17) of the effective mass (4.15).

4.6 Wilson flow

In the last few years, hadron scales extracted from the so-called *gradient flow* [50] have become very popular. The idea is to introduce an extra dimension, a fictitious *flow-time t* of mass dimension -2, and study the evolution of a gauge field $B_\mu(x,t)$ according to the flow equation

$$\begin{aligned} &\frac{dB_\mu(x,t)}{dt} = D_\nu G_{\nu\mu}(x,t) = -\frac{\delta S_G(B)}{\delta B_\mu(x,t)}, \\ &B_\mu(x,t)|_{t=0} = A_\mu(x), \quad D_\rho G_{\mu\nu} = \partial_\rho + ig_0[B_\rho, G_{\mu\nu}], \end{aligned} \tag{4.97}$$

where $G_{\mu\nu}$ is the field strength tensor evaluated on the field $B_\mu(x,t)$

$$G_{\mu\nu}(x,t) = \partial_\mu B_\nu(x,t) - \partial_\nu B_\mu(x,t) + ig_0\left[B_\mu(x,t), B_\nu(x,t)\right]. \tag{4.98}$$

A lattice version of the flow equation (4.97) is

$$\frac{dV_\mu(x,t)}{dt} = -g_0^2\left[\partial_{x,\mu} S_G^W(V(t))\right] V_\mu(x,t), \quad V_\mu(x,0) = U_\mu(x), \tag{4.99}$$

where $S_G^W(V(t))$ is the plaquette gauge action evaluated on the gauge fields $V_\mu(x,t)$ and the link derivatives are defined by

$$\partial_{x,\mu} f(U) = i\sum_a T^a \frac{d}{ds} f(e^{isX^a}U)\Big|_{s=0}, \quad X^a(y,\nu) = \begin{cases} T^a & \text{if } (y,\nu) = (x,\mu) \\ 0 & \text{else} \end{cases}. \tag{4.100}$$

As shown in Ref. [50], one of the benefits of using the flow $V_\mu(x,t)$ is that correlators built up from the links V_μ at finite $t > 0$ are renormalized quantities. Thus, we can use the Wilson flow (4.99) to define some non-perturbative reference scales. Let us consider, for instance, the energy density

$$E(x,t) = \frac{1}{4}\hat{G}^a_{\mu\nu}(x,t)\hat{G}^a_{\mu\nu}(x,t), \tag{4.101}$$

where $\hat{G}^a_{\mu\nu}$ are the Lie algebra components of the lattice strength tensor defined in (3.53). Using the energy density (4.101), we can construct the dimensionless combination $t^2E(x,t)$ and define the hadron scales $\sqrt{t_0}$ [50], $\sqrt{t_c}$ and w_0 [116]:

$$t^2\langle E(x,t)\rangle|_{t=t_0} = 0.3, \tag{4.102}$$

$$t^2\langle E(x,t)\rangle|_{t=t_c} = 0.2, \tag{4.103}$$

$$t\frac{d}{dt}t^2\langle E(x,t)\rangle|_{t=w_0^2} = 0.3. \tag{4.104}$$

In our calculations, we will use the hadron scale t_0, along with the Sommer parameter r_0 (4.77), to fix the lattice spacing and form dimensionless observables. In Ref. [80] it has been found that the physical value of the scale $\sqrt{t_0}$ in $N_f = 2+1$ QCD is $\sqrt{t_0} \approx 0.15$ fm.

4.7 Description of the lattice setup

In this section we explain the lattice discretization which has been used in this work and some details of the Monte Carlo simulations. We simulate two theories: QCD with $N_f = 2$ degenerate charm quarks and quenched QCD (pure $SU(3)$ gauge theory). As a lattice discretization we use:

- Wilson's plaquette gauge action for the gluon sector;
- a clover improved doublet of twisted mass fermions at maximal twist;
- open boundary conditions in the time direction to avoid the freezing of the topological charge, therefore the lattice actions are those given in Eqs. (3.128) and (3.130).

As concerns $N_f = 2$ QCD, we have used six dynamical ensembles [88, 46] and explored lattice spacings in the range 0.023 fm $\lesssim a \lesssim$ 0.066 fm. The lattice spacings have been determined through the scale L_1 [117, 118], which corresponds to the value of the running coupling $g^2_{R,SF}(L_1) = 4.484$ in the so-called *Schrödinger Functional scheme*. Note that the scale L_1, whose physical value is around 0.4 fm, is defined at vanishing quark masses, where standard and twisted mass Wilson quarks are equivalent. Thus for a fixed value of the gauge coupling $\beta = 6/g_0^2$, the two discretizations have the same lattice spacing. In order to achieve maximal twist, the hopping parameter κ (3.99) is set to its critical value κ_c (which reproduces a zero PCAC mass, see Eq. (3.82)) through an interpolation of published data [117, 119]. At every lattice spacing, the twisted mass parameter μ and the RGI mass of the charm quark M_c are chosen such that the pseudoscalar mass $\sqrt{t_0}m_{\eta_c}$ approximately corresponds to its physical value, i.e. $\sqrt{t_0}m_{\eta_c} \approx 1.80$[1]. Further details about the tuning of μ will be given in Chapter 6. At maximal twist, the clover term (introduced in Section 3.3) with non-perturbatively determined [72] coefficient c_{SW} (3.56) is not necessary for $O(a)$ improvement of physical observables. However, it was found that its inclusion reduces the $O(a^2)$ lattice artifacts, see e.g. [120].

The pure gauge theory has been simulated at four lattice spacings, in a range between 0.017 fm $\lesssim a \lesssim$ 0.049 fm, using Wilson's plaquette gauge action. As we explained in Section 2.3, on low energy observables like t_0, the applicability of decoupling [16, 17] of charm quarks from the fundamental Lagrangian is expected. Thus, on our quenched ensembles we set the lattice spacing requiring that

$$\sqrt{t_0}|_{N_f=0} = \sqrt{t_0(M_c)}|_{N_f=2} \quad \Rightarrow \quad a|_{N_f=0} = \frac{1}{\frac{\sqrt{t_0}|_{N_f=0}}{a|_{N_f=0}}} \times \sqrt{t_0(M_c)}|_{N_f=2}. \tag{4.105}$$

All the simulation parameters of our quenched and dynamical ensembles are listed in Table 4.2.

At our small lattice spacings, the critical slowing down represents one of the main obstacles to extract the continuum limit of the observables under study. In Figure 4.6, we show the

[1]Note that for $N_f = 2$ QCD, we find $\sqrt{t_0(M_c)} = 0.11$ fm, which significantly deviates from its physical value [80].

N_f	$\frac{T}{a} \times \left(\frac{L}{a}\right)^3$	β	a[fm]	κ	$a\mu$	$\sqrt{t_0}m_{\eta_c}$	t_0/a^2	MDUs
2	96×24^3	5.300	0.066	0.135943	0.36151	1.79321(53)	1.23950(85)	8000
	120×32^3	5.500	0.049	0.136638	0.165997	1.8049(16)	4.4730(95)	8000
	192×48^3	5.600	0.042	0.136710	0.130949	1.7655(15)	6.609(15)	8000
	120×32^3	5.700	0.036	0.136698	0.113200	1.7931(28)	9.104(36)	17184
	192×48^3	5.880	0.028	0.136509	0.087626	1.8129(29)	15.622(62)	23088
	192×48^3	6.000	0.023	0.136335	0.072557	1.8075(42)	22.39(12)	22400
0	120×32^3	6.100	0.049	–	–	–	4.4329(32)	64000
	120×32^3	6.340	0.036	–	–	–	9.034(29)	20080
	192×48^3	6.672	0.023	–	–	–	21.924(81)	73920
	192×64^3	6.900	0.017	–	–	–	39.41(15)	160200

Table 4.2 Simulation parameters of our ensembles. The columns show the lattice sizes, the gauge coupling $\beta = 6/g_0^2$, the lattice spacing in fm (determined from the $N_f = 2$ scale L_1 [46] and using decoupling for $N_f = 0$), the critical hopping parameter, the twisted mass parameter μ, the pseudoscalar mass in t_0 units, the hadronic scale t_0/a^2 defined in [50] and the total statistics in molecular dynamics units.

normalized autocorrelation function (3.114) of t_0 for the simulation $N_f = 2$, $\beta = 6.0$, see Table 4.2. The reference scale t_0 is an observable which manifests large autocorrelation times when $a \to 0$, thus we can estimate τ_{exp} from a fit of the form $A\exp(-t/\tau_{exp})$ to the tail of normalized autocorrelation function $\rho_{t_0}(t)$. In the example of Figure 4.6, the value of τ_{exp}, extracted from an exponential fit to the tail between $t = 15$ and $t = 42$, is $\tau_{exp} = 477(101)$ MDU. With open boundary conditions in time direction [79], one expects the scaling $\tau_{exp} \propto t_0/a^2$ and for the ensembles considered here can be parametrized as [121]

$$\tau_{exp} = -32(23) + 17.4(2.8)t_0/a^2. \tag{4.106}$$

The expected scaling of autocorrelation times with OB conditions has been shown in Figure 8 of Ref. [46].

As we already mentioned in Section 3.6, open boundary conditions mitigate the critical slowing down, but they can alter the values of the observables close to the boundaries. As example, we show in Figure 4.7 (l.h.s.) the dimensionless combination $t^2\langle E(t)\rangle$ for the ensemble $N_f = 2$, $\beta = 6.0$, where $E(t)$ is the energy density (4.101) and t is the flow time. To extract t_0 (r.h.s of Figure 4.7) we have considered the plateau average of $t^2\langle E(t)\rangle$ only in the range $x_0/a \in [32, 159]$, where boundary effects look negligible, and used a linear interpolation between the last value t_a which satisfies $t_a^2\langle E(t_a)\rangle < 0.3$ and the first value t_b which satisfies $t_b^2\langle E(t_b)\rangle > 0.3$.

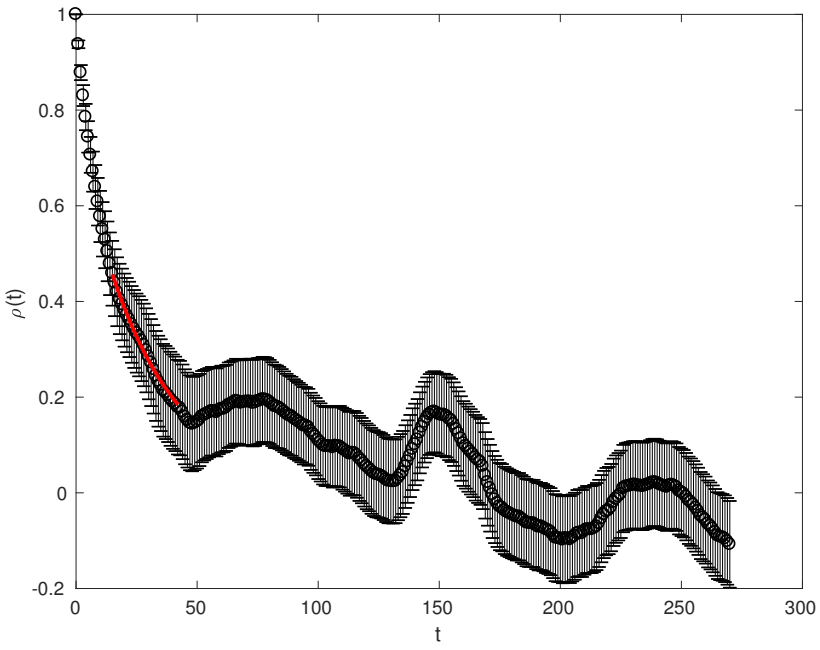

Figure 4.6 Autocorrelation function of t_0 for the ensemble $N_f = 2$, $\beta = 6.0$. The units on the x-axis correspond to 16 Molecular Dynamics Units (MDU). The red line is an exponential fit to estimate τ_{exp}. The picture has been taken from Ref. [121].

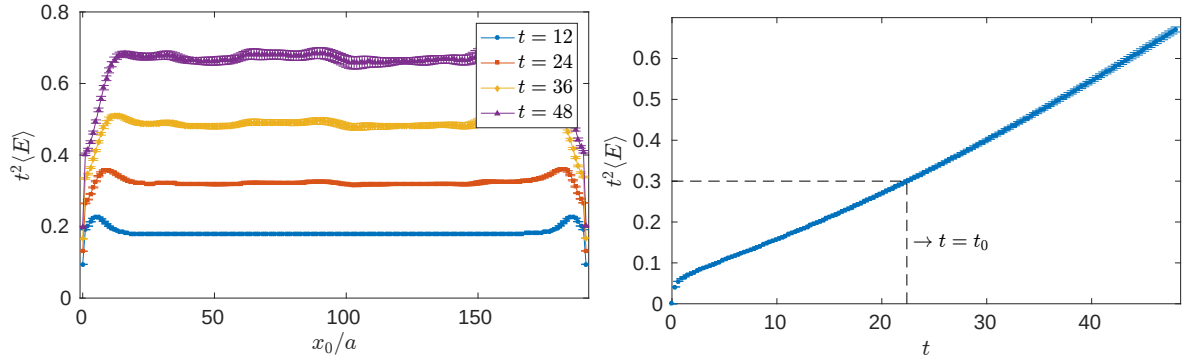

Figure 4.7 *Left panel*: Plot of $t^2\langle E(t)\rangle$ for some values of the flow time t as a function of x_0/a. *Right panel*: Plateau average of $t^2\langle E(t)\rangle$ in the range $x_0/a \in [32, 159]$ and interpolation of t_0.

Chapter 5

Charm sea effects on the strong coupling α_{qq} and on the static potential

In the first part of this work we want to give an estimate of the impact of a dynamical charm quark on pure gluonic observables. In particular, we focus on the ones that can be derived from Wilson loop measurements, like for example the static potential (4.74) and the strong coupling α_{qq} extracted from the static force (4.76). Our first results about these studies can be found in Refs. [122, 123]. Here we report the final results of our investigation and we explain in more detail the strategy which has been used.

5.1 Wilson loop measurements

As already mentioned in Section 4.3, the signal-to-noise ratio of Wilson loop measurements deteriorates when increasing the area of the loop. Therefore, instead of measuring $V(r)$ directly using Eq. (4.74), we follow the procedure described in Ref. [100]. The advantage is to reduce the unphysical static quark self energy contribution in the static potential and, as a consequence, improve the signal-to-noise ratio when measuring $V(r)$ at large spatial separations. In particular, before computing the Wilson loop values on our ensembles, we replace all the original gauge links by HYP2-smeared links [106], which correspond to the choice of smearing HYP-parameters written in Eq. (4.91). As the temporal links are concerned, their smearing corresponds to a choice of the static action. Then, the initial and the final lines of the Wilson loops are smeared up to four levels of HYP-smearing. This allows to extract the static potential with great accuracy after solving a generalized eigenvalue problem [124].

Once measured $V(r)$, we extract the static force and the strong coupling α_{qq} through Eqs. (4.79) and (4.76), where we used the improved distances r_I for HYP2-smeared links provided in Table 2 of Ref. [100]. The improved distances have a nontrivial dependence on the static quark line, therefore the values obtained for unsmeared links (see Ref. [96]) are slightly different from the ones obtained with HYP2-smeared links. Because of the local character of the HYP smearing, this discrepancy is more evident at short distances ($R \approx 2, 3, 4$), where its

distortion effects are more visible. Since the potential extracted at $R = 2$ may be affected by relatively large cutoff effects, we always consider Wilson loops with spatial extent $R \geq 3$.

5.2 Static potential

Following the strategy described in the previous section, we compute the static potential $V(r)$ on the ensembles listed in Table 4.2, neglecting the two coarsest lattices for $N_f = 2$ and $\beta = 5.3, 5.5$[1]. Since $V(r)$ can be determined only up to a constant, we choose to study the difference

$$\sqrt{8t_0}\Delta V(r) \equiv \sqrt{8t_0}\,[V(r) - V(r_A)], \quad r_A = 0.6\sqrt{8t_0}, \tag{5.1}$$

so that $\sqrt{8t_0}\Delta V(r)$ vanishes at $r = r_A$. To gain in statistical accuracy it is better to choose r_A as small as possible[2] and our choice $r_A = 0.6\sqrt{8t_0}$ corresponds to one of the smallest accessible distances for all the lattices under study here. In order to evaluate $V(r_A)$ on each ensemble, we use the interpolation function

$$V(r) = v_1 + v_2 r + \frac{v_3}{r} \tag{5.2}$$

suggested in Ref. [96]. In Eq. (5.2) the constants v_1, v_2 and v_3 have been determined using two distances r_1 and r_2 such that $r_1 < r_A < r_2$. As a third distance needed for the interpolation, we select the next accessible quark-antiquark separation r_3, larger than r_2 or smaller than r_1, such that the difference $|r_3 - r_A|$ is minimum. In Figure 5.1 we report the results of the

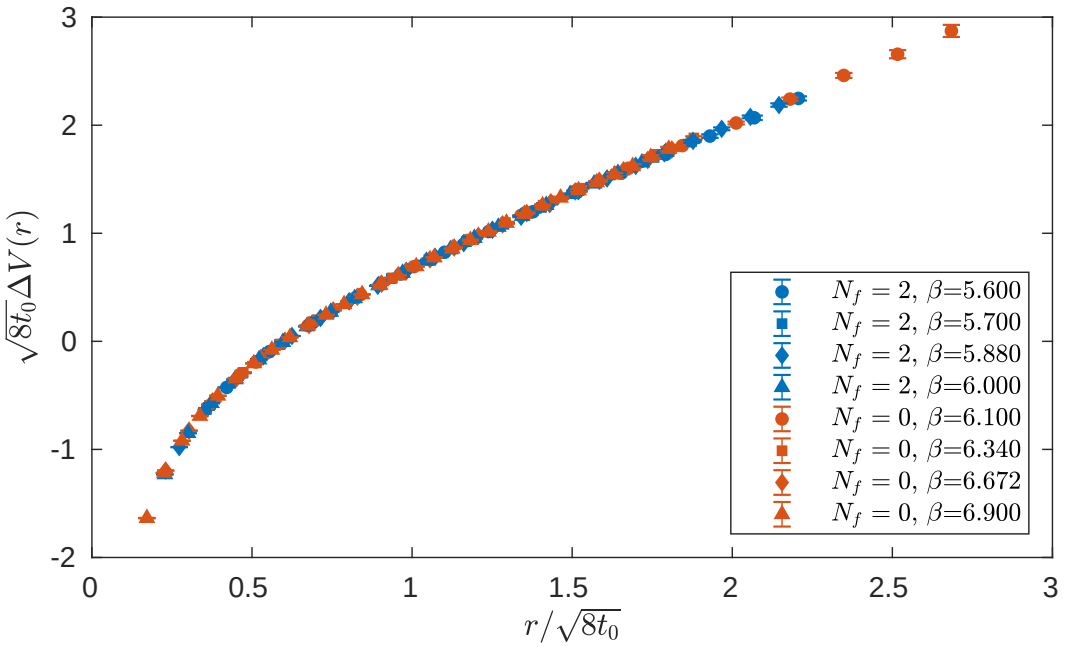

Figure 5.1 Static potential measured on our quenched ensembles (red markers) and dynamical ensembles (blue markers).

[1] As we will see better in the following sections, these lattices do not allow to measure the static potential at distances where charm sea effects become sizable and therefore they do not play a relevant role in the continuum extrapolation.

[2] The signal-to-noise ratio of Wilson loop measurements deteriorates at large distances.

static potential obtained with our quenched and dynamical ensembles. The behavior of our data looks quite regular, thus we do not expect large lattice artifacts. However, given that $\sqrt{8t_0}\Delta V(r)$ is not measured at the same physical distances on each lattice and because of the presence of possible cutoff effects in our data it is not easy to disentangle the charm sea effects from a direct comparison between $N_f = 0$ and $N_f = 2$ lattice data.

In order to evaluate these effects in the continuum limit, we calculate the difference (5.1) in the range of distances $r/\sqrt{8t_0} \in [0.35, 1.50]$ in steps of 0.05, making use of the interpolating function (5.2) again. Doing so, we measure $\sqrt{8t_0}\Delta V(r)$ at the same distances on different ensembles and this makes the achievement of our goals easier. From our lattice actions we expect $O(a^2)$ cutoff effects [100], thus we perform a best-fit to our data through the equation

$$\sqrt{8t_0}\Delta V(r,a) = \sqrt{8t_0}\Delta V(r,0) + k(r) \times \frac{a^2}{t_0}, \tag{5.3}$$

where the parameters to determine are the continuum value $\sqrt{8t_0}\Delta V(r,0)$ and the slope $k(r)$. The results of this procedure are shown in Figures 5.2, 5.3 and 5.4.

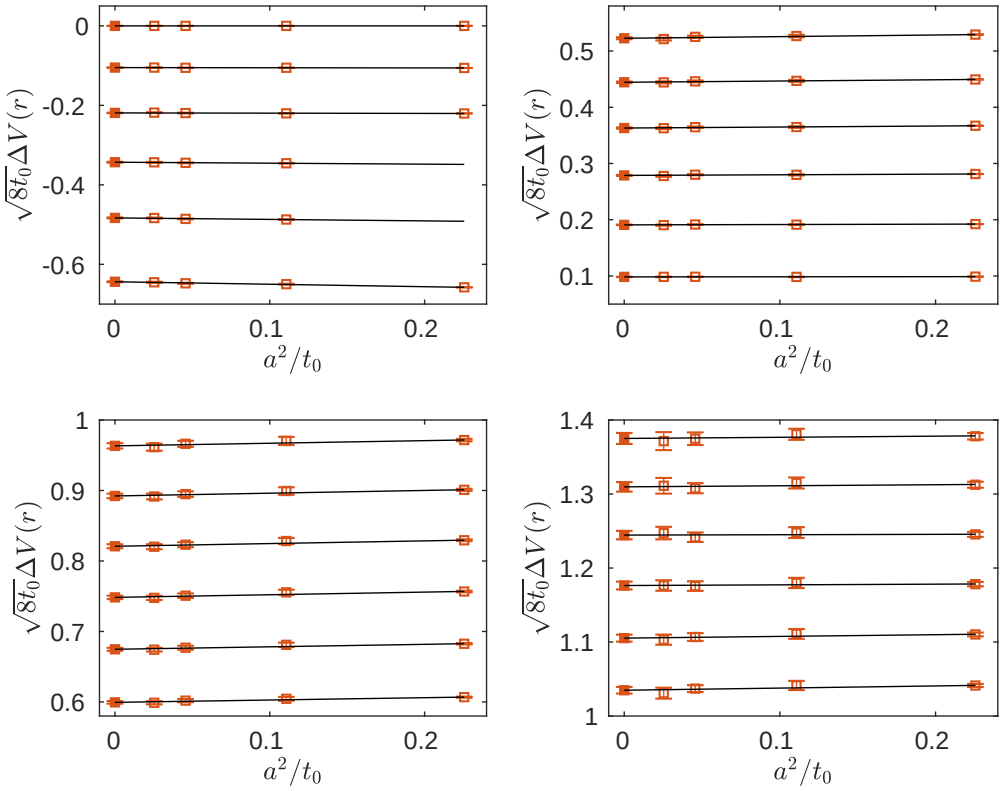

Figure 5.2 Continuum extrapolations of the static potential in the range of distances $r/\sqrt{8t_0} \in [0.35, 1.50]$ in steps of 0.05 for quenched QCD.

In particular, in Figures 5.2 and 5.3 we show the continuum extrapolations described by Eq. (5.3) at each interpolated distance in the range $r/\sqrt{8t_0} \in [0.35, 1.50]$. As can be seen the continuum extrapolations are performed with three or four lattice spacings, depending on the χ^2. The final result of these extrapolations is shown in Figure 5.4, where we compare the static potential of our two models in the continuum limit. As can be seen the dynamical charm see effects are not resolvable almost in the whole range of explored distances, except

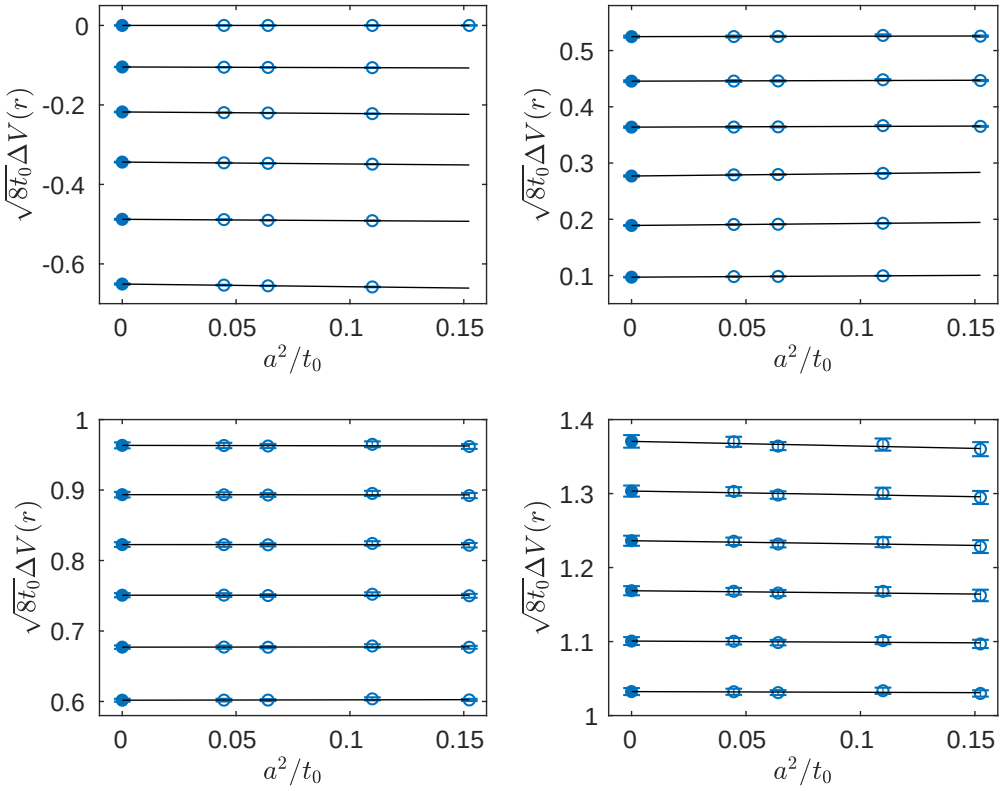

Figure 5.3 Continuum extrapolations of the static potential in the range of distances $r/\sqrt{8t_0} \in [0.35, 1.50]$ in steps of 0.05 for $N_f = 2$ QCD at $M = M_c$

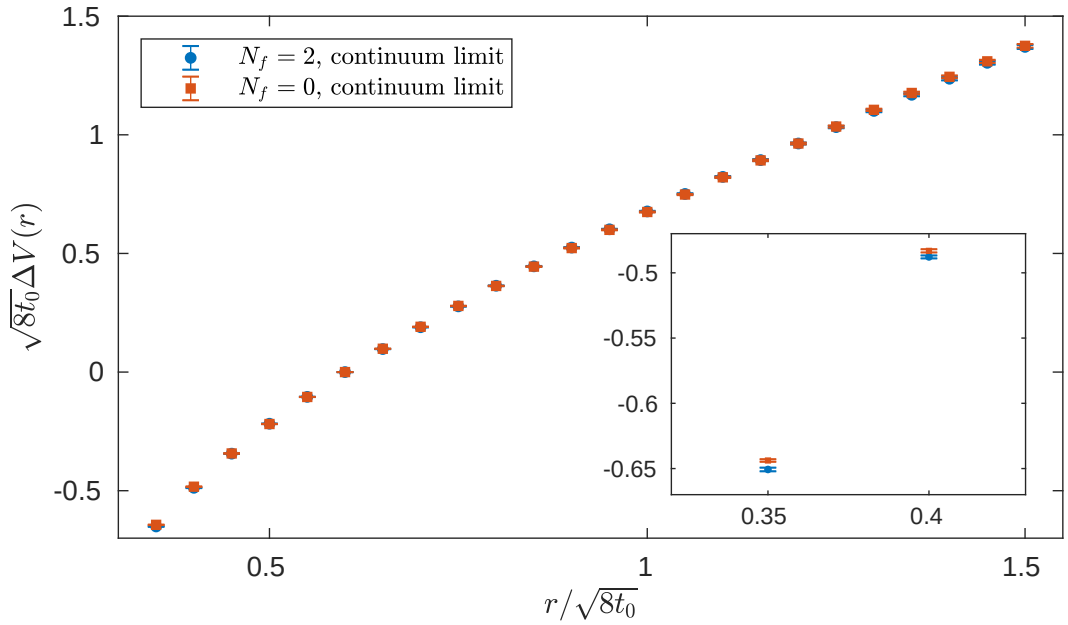

Figure 5.4 Comparison of the continuum extrapolations of the static potential in quenched QCD (red squares) and $N_f = 2$ QCD at $M = M_c$ (blue circles).

for $r/\sqrt{8t_0} \in [0.35, 0.40]$ where we observe a relative effect of around 1%. The limit of the approach described here is that the minimum distance where we can perform the continuum extrapolation is determined by the coarsest lattice. Therefore, we cannot compute the dynamical charm effects at smaller distances, where they are expected to be larger. As we will see in Section 5.5, for the strong coupling α_{qq} derived from the static force, we use a different strategy that allows to perform the continuum extrapolation at smaller distances.

5.3 Estimate of the string breaking distance for $N_f = 2$

When increasing the static quark separation, the dynamical charm effects on $\sqrt{8t_0}\Delta V(r)$ become smaller and smaller and the static potential seems to have the same shape in $N_f = 0$ and $N_f = 2$ QCD, as is evident from Figure 5.4. However, as explained in Section 4.5, this is true only for intermediate distances, because we expect string breaking in a theory with dynamical quarks. Thus, to give a rough estimate of the string breaking distance r_{sb} in QCD with $N_f = 2$ degenerate charm quarks, we study the static-charm meson correlator (4.92) to determine the distance r_{sb} such that

$$V_{Cornell}(r_{sb}) = 2M_{ps}, \tag{5.4}$$

where $V_{Cornell}(r)$ is the standard Cornell parametrization (4.75) and M_{ps} denotes the lowest energy state of the static-charm spectrum. To improve the accuracy of the correlator, we compute the Dirac propagator for 16 point sources for each spin and color component (which means $16 \times 12 = 192$ inversions in total). The space coordinate of the source is selected randomly, while we fix the time coordinate in a region of time slices where boundary effects can be considered negligible. We determine the mass of the ground state with the weighted plateau average (4.17) of the effective mass (4.15). In Figure 5.5 we report an example of this calculation for the dynamical ensemble with $\beta = 6.0$. Since our measurements of the static potential are always much below the value $2M_{ps}$, we fit the Cornell parametrization (4.75) to our lattice data and determine r_{sb} through extrapolation, as shown in Figure 5.6. We observe that Cornell's parametrization fits the static potential measured on our $N_f = 2$ ensembles very well for a large range of distances, with $\chi^2/N_{dof} < 1$. We repeat this procedure at every lattice spacing and we always find

$$6.5 \lesssim r_{sb}/\sqrt{8t_0} \lesssim 7.5, \tag{5.5}$$

as summarized in Table 5.1. However, since r_{sb} is much larger than the distances considered for

	$\beta = 5.60$	$\beta = 5.70$	$\beta = 5.88$	$\beta = 6.00$
$r_{sb}/\sqrt{8t_0}$	6.76(22)	6.64(14)	7.26(17)	7.31(16)

Table 5.1 Estimate of the string breaking distance on our $N_f = 2$ ensembles.

our measurements of the static potential, the systematic errors in r_{sb} due to the extrapolation of

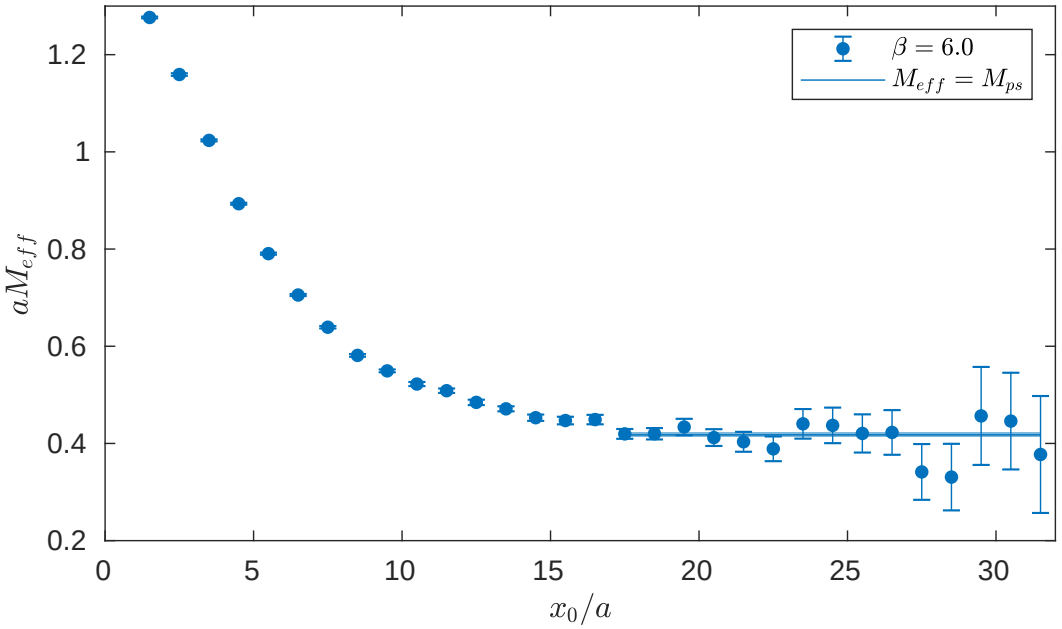

Figure 5.5 Calculation of the effective mass and plateau average to determine the ground state of the static-charm meson for the dynamical ensemble with $\beta = 6.0$.

$V(r)$ are probably bigger than the cutoff effects. Therefore, we do not perform any continuum extrapolation and we only provide an indicative estimate

$$\frac{r_{sb}}{\sqrt{8t_0(M_c)}} \approx 7.0 \quad \Rightarrow \quad r_{sb} \approx 2.24 \text{ fm}, \tag{5.6}$$

that can be easily obtained using [46, 117]

$$\frac{\sqrt{t_0(M_c)}}{L_1} = 0.2828(62), \quad L_1 = 0.40(1) \text{ fm}. \tag{5.7}$$

Note that our result (5.6) is significantly larger than the one found in Ref. [113] for $N_f = 2$ QCD with pion mass $m_\pi \approx 640$ MeV, that is $r_{sb} = 1.248(13)$ fm. This shows that the string breaking distance clearly depends on the pion mass and more detailed investigations can be useful to understand its mass dependence.

5.4 Determination of the β_{qq}-function

Now we show our continuum extrapolation of the β_{qq}-function in QCD with $N_f = 2$ degenerate charm quarks and quenched QCD. The main goal of this investigation is to evaluate the size of the dynamical charm effects first on the β_{qq}-function and then on the strong coupling in the qq-scheme.

After computing $g^2_{qq}(r_I) = 4\pi r^2 F(r_I)/C_F$ (see Eqs. (4.76) and (4.79)) on each of our lattices, we study the so-called *step scaling function* σ [125], whose definition in terms of a fixed scale factor f is

$$\sigma(f,u) = g^2_{qq}(f \times r)|_{g^2_{qq}(r)=u}. \tag{5.8}$$

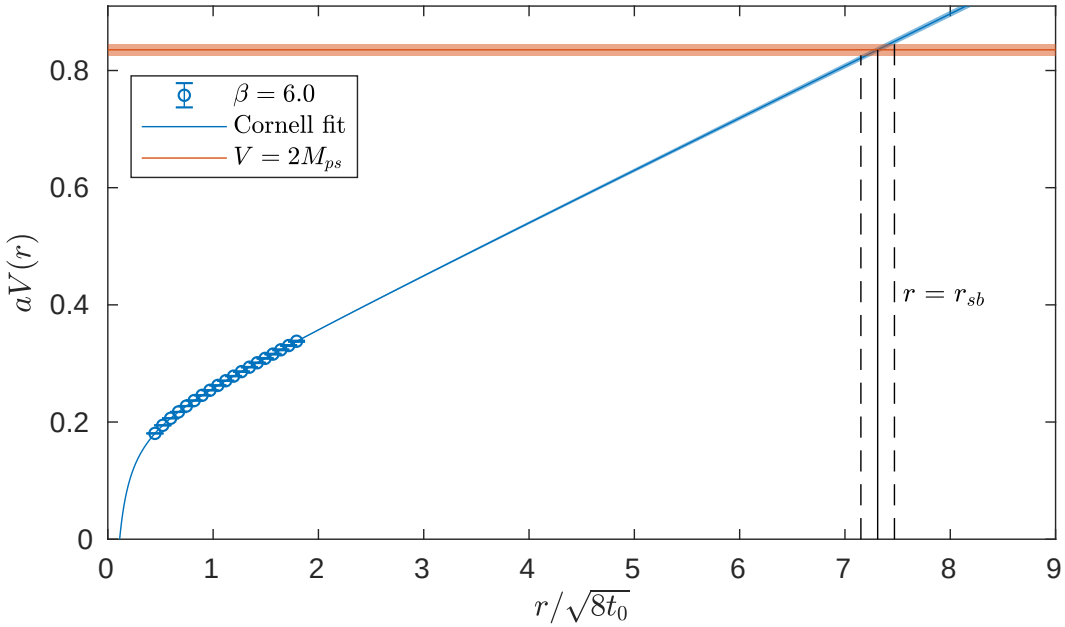

Figure 5.6 Cornell fit (blue band) to our lattice data (empty circles) at $\beta = 6.0$. The vertical dashed lines indicate the region where $V(r) = 2M_{ps}$ (red band). The width of the blue band comes from the covariance matrix of the best-fit parameters A, B and σ of Eq. (4.75).

Hence, $\sigma(f,u)$ measures the variation of the coupling g_{qq} if we change the distance scale by a factor f and it can be considered like a discrete version of the β_{qq}-function. Solving the ODE coming from the definition of β_{qq} (4.80), we arrive at the relation

$$\log(f) = -\int_{\sqrt{u}}^{\sqrt{\sigma(f,u)}} \frac{dx}{\beta_{qq}(x)}, \tag{5.9}$$

which is true only in the continuum limit. To adapt Eq. (5.9) to our lattice data, we use a slightly modified version of it, following a strategy used in Ref. [126].

First, we parametrize β_{qq} as

$$\beta_{qq} = -\frac{g_{qq}^3}{P(g_{qq}^2)}, \quad P(g_{qq}) = p_0 + p_1 g_{qq}^2 + p_2 g_{qq}^4 + \cdots + p_{n_{max}+1} g_{qq}^{2(n_{max}+1)}, \tag{5.10}$$

where we denote with $2\times(n_{max}+1)$ the degree of the polynomial $P(g_{qq})$. The advantage of the parametrization (5.10) lies in the fact that we can rewrite Eq. (5.9) in the handier form

$$\log(f) = -\frac{p_0}{2}\left[\frac{1}{\sigma(f,u)} - \frac{1}{u}\right] + \frac{p_1}{2}\log\left[\frac{\sigma(f,u)}{u}\right] + \sum_{n=1}^{n_{max}} \frac{p_{n+1}}{2n}\left[\sigma^n(f,u) - u^n\right]. \tag{5.11}$$

Even though the parametrization (5.10) is different from the one motivated by perturbation theory (see Eq. (4.81)), we will see that it is able to describe our non-perturbative data satisfactorily.

Then, the idea would be to extract the β_{qq}-parameters $p_0, p_1, \ldots, p_{n_{max}+1}$ from a global best-fit to our data through Eq. (5.11). However, given that from our simulations we cannot

access $\sigma(f,u)$, but only its lattice counterpart $\Sigma(f,u,a)$, which satisfies

$$\lim_{a\to 0}\Sigma(f,u,a)=\sigma(f,u), \tag{5.12}$$

instead of Eq. (5.11) we use

$$\begin{aligned}\log(f)+h(f,u,a)=&-\frac{p_0}{2}\left[\frac{1}{\Sigma(f,u,a)}-\frac{1}{u}\right]+\frac{p_1}{2}\log\left[\frac{\Sigma(f,u,a)}{u}\right]\\&+\sum_{n=1}^{n_{max}}\frac{p_{n+1}}{2n}\left[\Sigma^n(f,u,a)-u^n\right],\end{aligned} \tag{5.13}$$

where we introduce a function $h\equiv h(f,u,a)$ to also consider the cutoff effects. The form of our lattice actions induced us to choose the following parametrization of the lattice artifacts

$$h(f,u,a)=\rho(f,u)\times\frac{a^2}{8t_0},\quad \rho(f,u)=\sum_{i=0}^{n_\rho-1}\rho_i(f)u^i. \tag{5.14}$$

Thus, apart from the parameters of the β_{qq}-function, we have also to determine the parameters of the function h, which takes into account the presence of cutoff effects in our data.

To extract the continuum limit of β_{qq} for our two models, we choose the scale factor $f=2$. To keep this factor constant, we interpolate the static force at appropriate distances using the interpolating function

$$F(r)=f_1+f_2r^{-2} \tag{5.15}$$

suggested in Ref. [96]. At every distance of interest r, the constants f_1, f_2 have been determined using the two closest distances to r, that we call r_1 and r_2, such that $r_1<r<r_2$. The values of $\sigma(f,u)$ and u used in our best-fit procedure correspond to distances that approximately cover the range $r/\sqrt{8t_0}\in[0.20,1.30]$.

5.4.1 Best-fit procedure

Using a matrix notation, Eq. (5.13) can be written in the form

$$A_{m\times n}\cdot x_{n\times 1}=b_{m\times 1}, \tag{5.16}$$

where

$$x_{n\times 1}=\begin{pmatrix}p_0\\ \vdots\\ p_{n_{max}+1}\\ \rho_0\\ \vdots\\ \rho_{n_{\rho-1}}\end{pmatrix}_{n\times 1},\quad b_{m\times 1}=\begin{pmatrix}\log(2)\\ \vdots\\ \log(2)\end{pmatrix}_{m\times 1} \tag{5.17}$$

and $A_{m\times n}$ is a matrix which depends on m doublets of measurements $\{\Sigma,u\}$ performed at different distances for each lattice spacing. Our goal is to find the least square solution $\hat{x}$

of the problem (5.16) that allows to determine the parameters p_i and ρ_i of the functions β_{qq} (5.10) and h (5.14) respectively. This would be relatively easy if the elements of the matrix A were uncorrelated numbers without errors and the elements of b had a known covariance matrix $\mathrm{Cov}(b)_{(m\times m)}$. In such cases the least square solution $\hat{x}$ can be found minimizing

$$(b-Ax)^T \mathrm{Cov}^{-1}(b)(b-Ax). \tag{5.18}$$

However, in our case b is a fixed vector with no errors and correlations, while the elements of the matrix A are correlated, because the measurements of g^2_{qq} at different distances coming from the same ensemble are correlated. Thus, in order to find the least square solution $\hat{x}$ we proceed as follows:

1. Start from a guess solution $\hat{x}_0$ and evaluate the $(m\times 1)$ column vector $y = A\hat{x}_0$; here we choose the least square solution $\hat{x}_0$ of Eq. (5.16) when neglecting errors and correlations both on A and b.

2. Compute the covariance matrix of $y = (y_1, \cdots, y_m)$ through[3]

$$\mathrm{Cov}(y)_{(m\times m)} = S_{(m\times 2m)} \mathrm{Cov}(g^2_{qq})_{(2m\times 2m)} S^T_{(2m\times m)}, \tag{5.19}$$

   where S is the matrix of the derivatives

$$S_{k,l} = \frac{\partial y_k}{\partial g^2_{qq,l}} = \begin{pmatrix} \frac{\partial y_1}{\partial g^2_{qq,1}} & \frac{\partial y_1}{\partial g^2_{qq,2}} & \cdots & \frac{\partial y_1}{\partial g^2_{qq,2m}} \\ \frac{\partial y_2}{\partial g^2_{qq,1}} & \frac{\partial y_2}{\partial g^2_{qq,2}} & \cdots & \frac{\partial y_2}{\partial g^2_{qq,2m}} \\ \vdots & \vdots & \ddots & \vdots \\ \frac{\partial y_m}{\partial g^2_{qq,1}} & \frac{\partial y_m}{\partial g^2_{qq,2}} & \cdots & \frac{\partial y_m}{\partial g^2_{qq,2m}} \end{pmatrix}_{m\times 2m} \tag{5.20}$$

   evaluated on the mean value $\langle g^2_{qq}\rangle = (\langle g^2_{qq,1}\rangle, \cdots \langle g^2_{qq,2m}\rangle)$ and $\mathrm{Cov}(g^2_{qq})_{(2m\times 2m)}$ has a block diagonal form

$$\mathrm{Cov}(g^2_{qq}) = \begin{pmatrix} M_1 & 0 & \cdots & 0 \\ 0 & M_2 & \cdots & 0 \\ \vdots & \vdots & \ddots & \vdots \\ 0 & 0 & \cdots & M_{n_{ens}} \end{pmatrix}_{2m\times 2m} . \tag{5.21}$$

   This form is due to the fact that measurements of g^2_{qq} on different ensembles are independent, while the ones performed at different distances, but on the same ensemble, are not.

3. Assume $\mathrm{Cov}(b)_{(m\times m)} \equiv \mathrm{Cov}(y)_{(m\times m)}$ and find the standard least square solution $\hat{x}_{new}$ which minimizes Eq. (5.18).

[3]Note that for every measurement we need to determine the coupling at two distances, $g^2_{qq}(r)$ and $g^2_{qq}(2r)$, therefore the sizes of the matrices S and $\mathrm{Cov}(g^2_{qq})$ are $(m\times 2m)$ and $(2m\times 2m)$ respectively.

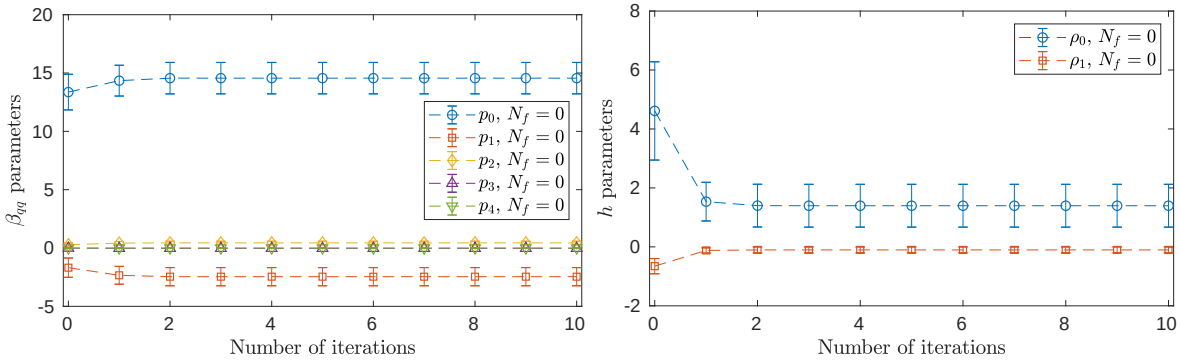

Figure 5.7 Example for $N_f = 0$ QCD using 5 parameters for β_{qq} (5.10) and 2 for h (5.14). *Left panel*: Convergence rate of the β_{qq} parameters. *Right panel*: Convergence rate of the h parameters.

4. Repeat the steps 1, 2, 3 replacing $\hat{x}_0 \to \hat{x}_{new}$ until convergence on the best-fit parameters is reached.

The covariance matrix (5.21) has been calculated using our analysis package based on the Matlab routine *UWerr.m* [77]. Convergence on the best-fit parameters is reached after a few iterations, as shown in the example of Figure 5.7 for $N_f = 0$ QCD, using 5 parameters for β_{qq} (5.10) and 2 for h (5.14).

5.4.2 Best-fit results

We performed several correlated best-fits, changing the number of parameters both in β_{qq} and h. We found a good agreement between different types of fits. Among several possible parametrizations to describe our data, here we focus only on the ones having a reasonable χ^2 and as few parameters as possible. The result of this procedure is depicted in Figure 5.8, where the red and blue bands represent the β_{qq}-functions of $N_f = 0$ and $N_f = 2$ QCD respectively, whilst the numerical details are summarized in Table 5.2.

Theory	Best-fit parameters					$\frac{\chi^2}{N_{dof}}$
$N_f = 0$	p_0	p_1	p_2	p_3	p_4	0.54
	14.6(1.3)	−2.46(78)	0.44(15)	−0.025(11)	0.00050(26)	
	ρ_0	ρ_1				
	1.40(73)	−0.10(10)				
$N_f = 2$ ($M = M_c$)	p_0	p_1	p_2	p_3		0.14
	17.0(1.2)	−2.42(45)	0.297(56)	−0.0084(21)		
	ρ_0	ρ_1	ρ_2	ρ_3		
	74.9(16.1)	−37.4(8.2)	6.3(1.4)	−0.354(85)		

Table 5.2 Results of the best-fit through which we extract the parameters of the β_{qq}-function in $N_f = 0$ QCD and QCD with $N_f = 2$ degenerate charm quarks.

From Figure 5.8, we see that the dynamical charm effects on the β_{qq}-function get quite visible (with our precision) starting from values of $\alpha_{qq} \lesssim 0.5$, i.e. when energy increases and becomes comparable or larger than the charm mass M_c. Since the smallest accessible distances used in our best-fits correspond to a coupling $\alpha_{qq} \approx 0.25$, the region where our extrapolation is more accurate and reliable starts approximately from this value of the coupling. However,

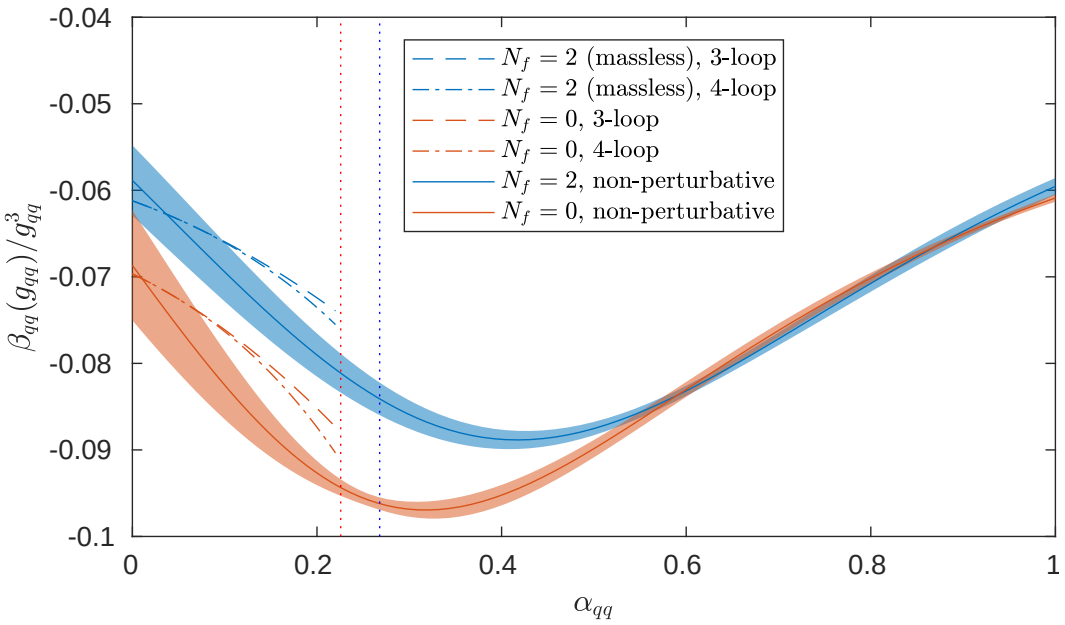

Figure 5.8 Comparison of the β_{qq}-functions in quenched QCD and $N_f = 2$ QCD at $M = M_c$. The vertical red and blue dotted lines indicate the smallest value of α_{qq} that we can reach with our measurements in $N_f = 0$ and $N_f = 2$ QCD respectively.

in order to see whether our non-pertubative functions make contact with the perturbative ones at high energies, we show our bands down to $\alpha_{qq} = 0$[4]. For quenched QCD, we observe that when $\alpha_{qq} \to 0$ there is an acceptable agreement between our non-perturbative β_{qq}-function (red band) and the perturbative ones up to 3 and 4 loops (dashed and dash-dot red lines). As concerns QCD with $N_f = 2$ degenerate charm quarks, it is interesting to remark that the non-perturbative β_{qq}-function (blue band) seems to get closer to the 3 and 4 loop perturbative functions (dashed and dash-dot blue lines) of the 2 flavor massless theory with increasing energy. Of course, when α_{qq} goes to zero the error band is not thin enough to give accurate results, however the behavior observed is the one foreseen: when the energy E increases and becomes much larger than the charm mass M_c, our model approaches the 2 flavor massless theory.

5.5 Strong coupling α_{qq}

Once computing the parameters of the β_{qq}-function for both models, we extract the continuum limit of the strong coupling α_{qq} solving the ODE given in the definition of β_{qq}, Eq. (4.80). As this method requires the choice of an initial condition, first we compute the continuum limit of α_{qq} at a certain reference distance r_{ref}. In order to do that, we set $r_{ref} = 0.75\sqrt{8t_0}$[5] and then we use the interpolation function (5.15) to measure $\alpha_{qq}\left(r_{ref}, a\right)$ on our quenched and

[4]The authors of Ref. [127] showed that there are visible deviations between the perturbative and non-perturbative running coupling at $\alpha_{qq} \approx 0.24$, even using the perturbatutive expansion of the β_{qq}-function up to four loops.

[5]This corresponds to one of the smallest accessible distances through which a continuum extrapolation with four lattice spacings is possible.

dynamical ensembles. Finally, fitting the curve[6]

$$\alpha_{qq}\left(r_{ref},a\right)=\alpha_{qq}\left(r_{ref},0\right)+k\times\frac{a^2}{t_0} \tag{5.22}$$

to the interpolated data we obtain

- $\alpha_{qq}\left(r_{ref},0\right)=0.7299(32)$, $\frac{\chi^2}{N_{dof}}=\frac{0.04}{2}$ in $N_f=0$ QCD,
- $\alpha_{qq}\left(r_{ref},0\right)=0.7329(37)$, $\frac{\chi^2}{N_{dof}}=\frac{0.52}{2}$ in $N_f=2$ QCD at $M=M_c$.

and we summarize the whole procedure in Figure 5.9. After calculating the initial conditions

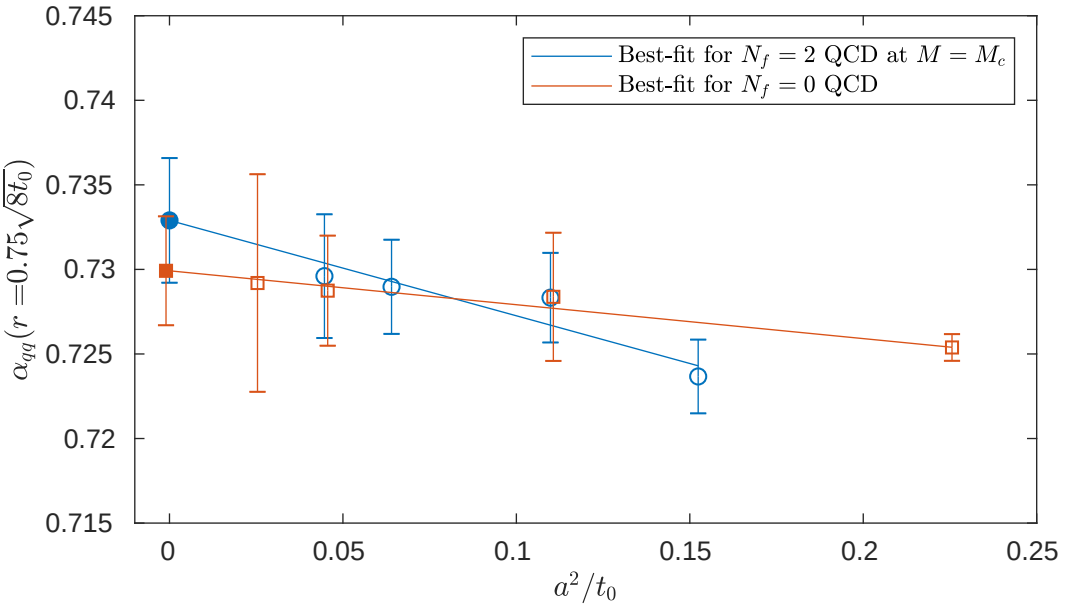

Figure 5.9 Continuum extrapolation of the strong coupling in the qq-scheme at the reference distance $r_{ref}=0.75\sqrt{8t_0}$. The lattice data of our quenched and dynamical ensembles are represented by empty squares and circles respectively. The analogous full markers denote the continuum limit values.

for our two theories, we solve their respective ODEs making use of the Matlab routine *ode45* and we show our final results in Figures 5.10 and 5.11.

The strong coupling α_{qq} is represented by an error band (red for quenched QCD and blue for $N_f=2$ QCD at $M=M_c$), whose thickness depends both on the statistical error of the initial condition and on the uncertainty on the parameters of the β_{qq}-function. In particular, in Figure 5.10 we present our continuum extrapolation of α_{qq} in $N_f=0$ QCD. Our results are compared to the ones found in Ref. [96] (black circles) and to the perturbative running coupling up to four loop (dashed black lines). The latter has been calculated by using the following estimate of the Λ parameter in the $\overline{\text{MS}}$ scheme

$$\sqrt{8t_0}\Lambda_{\overline{\text{MS}}}(N_f=0)=0.565(45), \tag{5.23}$$

[6] As in Eq. (5.3), the parametrization of the curve is suggested by the lattice actions.

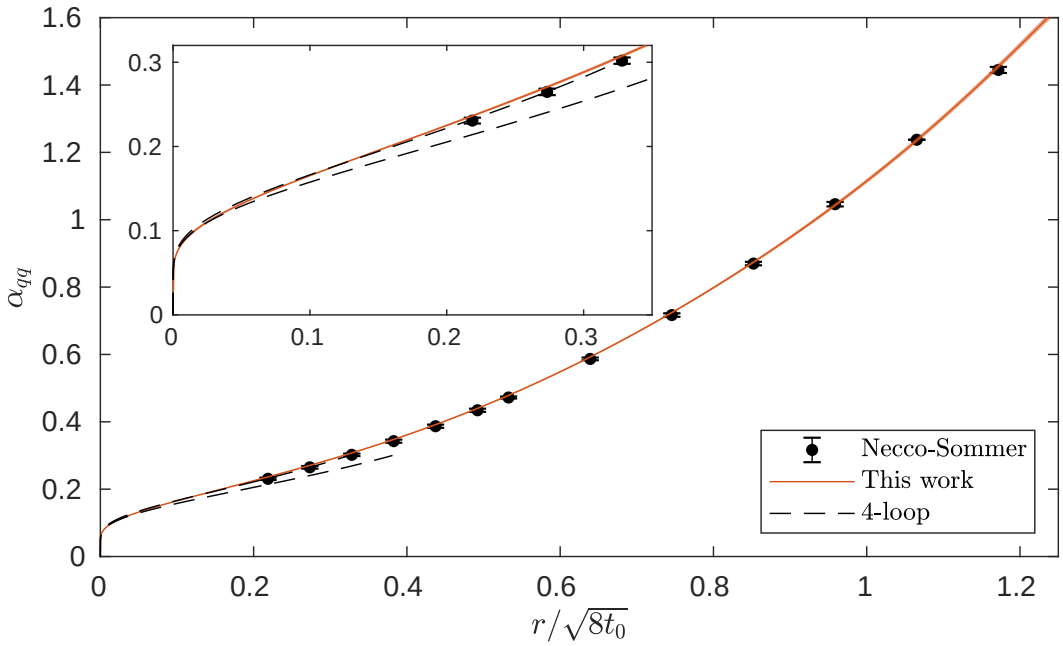

Figure 5.10 Comparison between our continuum extrapolation of α_{qq} in $N_f = 0$ QCD (the red band) and the one obtained in Ref. [96] (black circles). The dashed black lines represent the perturbative running coupling calculated up to four loops. The data of [96] refer to distances given in r_0 units, thus to express them in terms of $r/\sqrt{8t_0}$ we use the ratio $r_0/\sqrt{t_0} = 3.013(17)$ known from Ref. [88].

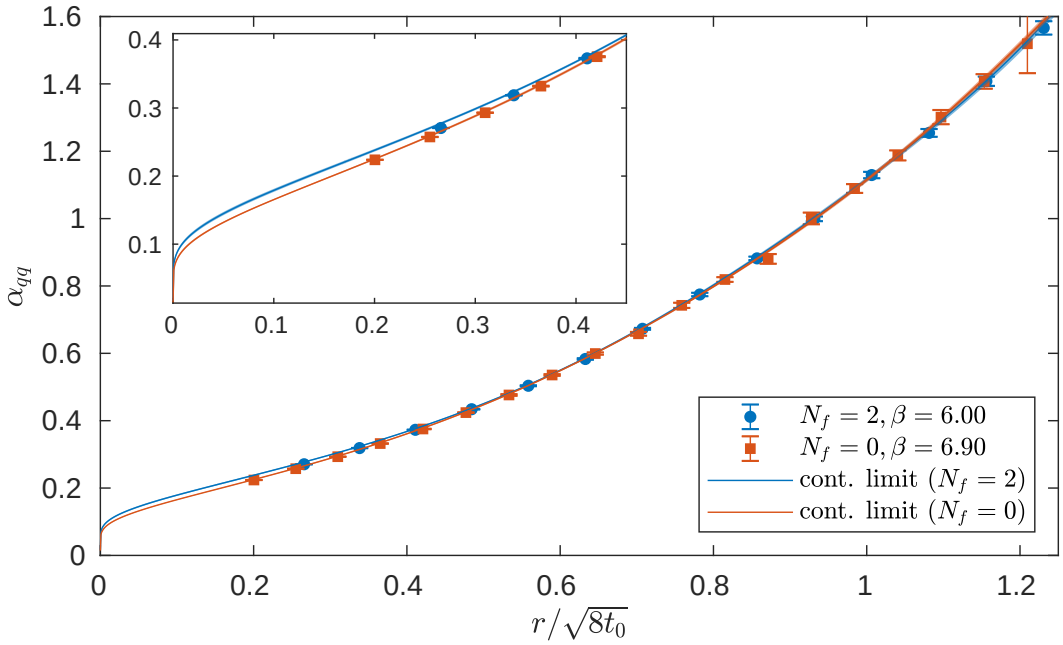

Figure 5.11 Comparison of α_{qq} in QCD with $N_f = 2$ degenerate charm quarks and $N_f = 0$ QCD.

obtained from $r_0\Lambda_{\overline{\rm MS}}(N_f = 0) = 0.602(48)$ [128] and $r_0/\sqrt{t_0} = 3.013(17)$ [88][7]. The spread between the two dashed black lines just comes from the uncertainty on the Lambda parameter.

[7] To convert the Lambda parameter (5.23) to the qq-scheme we use the relation [129]

$$\begin{aligned} &\Lambda_{qq} = \Lambda_{\overline{\rm MS}} e^{k_1/(8\pi b_0)}, \\ &k_1 = \frac{1}{4\pi}(a_1 + a_2 N_f), \quad a_1 = -\frac{35}{3} + 22\gamma_E, \quad a_2 = \frac{2}{9} - \frac{4}{3}\gamma_E, \end{aligned} \tag{5.24}$$

where $\gamma_E \approx 0.577$ is the Euler-Mascheroni constant.

We observe that our continuum extrapolation perfectly agrees with the one of Ref. [96]. In order to make contact with perturbation theory we would need to reach $\alpha_{qq} \lesssim 0.15$, but our lattices are not fine enough (see Ref. [127] for measurements at finer lattice spacings in $N_f = 0$ QCD). However, we observe that our continuum extrapolation seems to agree with the expectations of perturbation theory when $\alpha_{qq} \to 0$.

In Figure 5.11 a comparison of the strong coupling α_{qq} in $N_f = 0$ and $N_f = 2$ QCD is shown. Other than the continuum extrapolations, we also present the measurements originating from the quenched ensemble at $\beta = 6.90$ (red squares) and the dynamical ensemble at $\beta = 6.00$ (blue circles). From the comparison of our error bands, we observe that the dynamical charm effects on α_{qq} get clearly visible when

$$r \lesssim \frac{1}{M_c} \approx 0.13 \text{ fm} \quad \Rightarrow \quad \frac{r}{\sqrt{8t_0}} \lesssim 0.42, \tag{5.25}$$

where we use the RGI mass $M_c = 1510$ MeV [130] and the value of $\sqrt{t_0}$ given in Eq. (5.7). This is still more evident when considering the ratio

$$\frac{[\alpha_{qq}]^{N_f=2} - [\alpha_{qq}]^{N_f=0}}{[\alpha_{qq}]^{N_f=0}}, \tag{5.26}$$

as shown in Figure 5.12. As can be seen from our non-perturbative curve (blue band), when

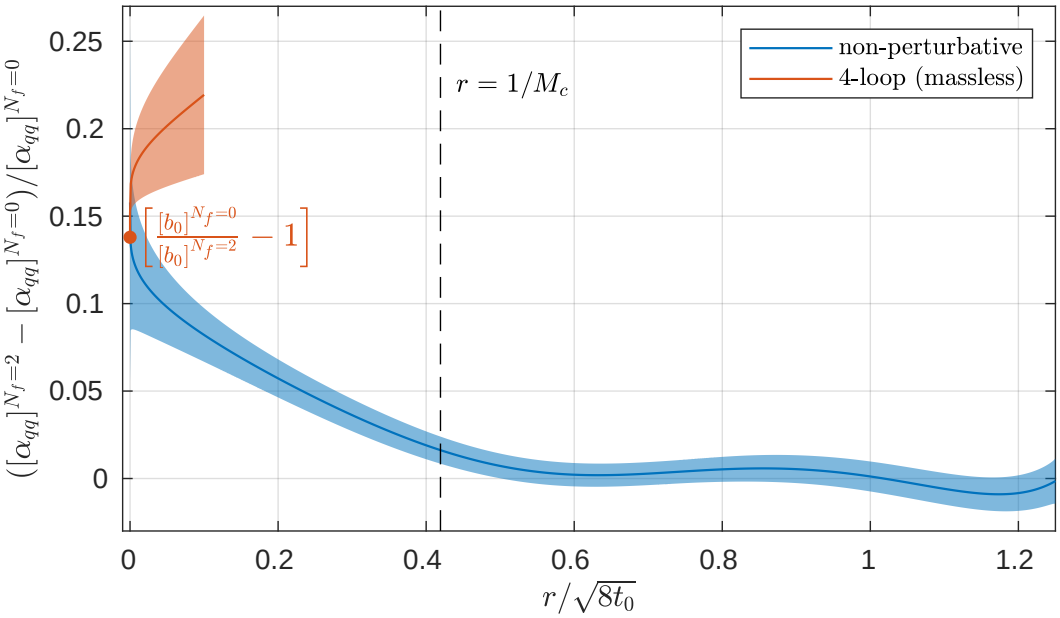

Figure 5.12 Computation of the derived quantity $([\alpha_{qq}]^{N_f=2} - [\alpha_{qq}]^{N_f=0})/[\alpha_{qq}]^{N_f=0}$. The vertical dashed line corresponds to the value $1/M_c$. The perturbative curve has been computed using the $N_f = 0$ Lambda parameter (5.23), the $N_f = 2$ Lambda parameter in units of L_1 known from Ref. [117], the value $\sqrt{t_0(0)}/L_1 = 0.3881(52)$ [46] and the conversion formula to the qq-scheme (5.24).

$r \gg 1/M_c$ decoupling of charm quarks applies and we can assume $[\alpha_{qq}]^{N_f=2} \approx [\alpha_{qq}]^{N_f=0}$. As the energy increases the charm sea effects on α_{qq} become more and more important and we observe around 6% effects at $r/\sqrt{8t_0} \approx 0.2$, which is approximately the smallest distance that we can reach with our finest lattices. To compare our results with the expectations

of perturbation theory (red band) for the $N_f = 2$ massless theory, we extrapolate our non-perturbative curve down to $r/\sqrt{8t_0} = 0$. The result that we obtain is physically equivalent to what we have already seen in Section 5.4.2 for the β_{qq}-function: at energies scales $E \gg M_c$ our model approaches the 2 flavor massless theory[8] and when we are close to the limit $r/\sqrt{8t_0} \to 0$ we can assume $[\alpha_{qq}]^{N_f=2}_{M=M_c} \approx [\alpha_{qq}]^{N_f=2}_{M=0}$.

5.6 Lambda parameter in $N_f = 0$ QCD

As a final application, we also tried to extract the Lambda parameter in $N_f = 0$ QCD from our lattice data. In the qq-scheme its expression is (see Eq. (2.27))

$$\Lambda_{qq} = \frac{1}{r}\left(b_0 g_{qq}^2\right)^{-\frac{b_1}{2b_0^2}} e^{-\frac{1}{2b_0 g_{qq}^2}} \exp\left\{-\int_0^{g_{qq}} dx \left[\frac{1}{\beta_{qq}(x)} + \frac{1}{b_0 x^3} - \frac{b_1}{b_0^2 x}\right]\right\}, \tag{5.28}$$

where the perturbative expansion of β_{qq} and its coefficients b_i up to 4-loop order are written in Eqs. (2.25), (4.81) and (4.82). To convert the results to the more familiar $\overline{\text{MS}}$-scheme, we use the relation (5.24) that for $N_f = 0$ reads

$$\Lambda_{\overline{\text{MS}}} = \Lambda_{qq} \times \exp\left(\frac{35}{66} - \gamma_E\right). \tag{5.29}$$

We remind that Λ_{qq} is an RGI quantity, therefore its value must be independent of g_{qq}. However, since the perturbative expansion of β_{qq} is known up to 4-loop order, Λ_{qq} has a residual dependence on g_{qq}, that becomes negligible only for small values of the coupling, i.e. in the limit $g_{qq} \to 0$.

In Figure 5.13 we show our calculation of $\Lambda_{\overline{\text{MS}}}$ using the 2-, 3- and 4-loop expressions of β_{qq} and the values of g_{qq} obtained with our continuum extrapolation discussed in Section 5.5. We report the error bands only down to $\alpha_{qq} = 0.15$. Beyond this value, extrapolation errors become important[9] and get significantly large when $\alpha_{qq} \to 0$. From our analysis, it seems that the 3- and 4-loop bands start making contact at $\alpha_{qq} \approx 0.2$. However, the range of couplings where $\Lambda_{\overline{\text{MS}}}$ is approximately constant is not reached yet, as we observe (although with a large statistical uncertainty) a drift towards smaller values of $\sqrt{8t_0}\Lambda_{\overline{\text{MS}}}$. This is also confirmed by the results of Ref. [127], where the Λ parameter is extracted from quenched simulations at extremely fine lattice spacings, that allow to measure g_{qq} at distances $r/r_0 = 0.07$.

Therefore we just give, as indicative result, the value of our extrapolation at $\alpha_{qq} = 0.15$

$$\left[\sqrt{8t_0}\Lambda_{\overline{\text{MS}}}(N_f = 0)\right]_{\alpha_{qq}=0.15} = 0.587(43). \tag{5.30}$$

[8] Note that in perturbation theory the quantity (5.26) is well defined even at $r = 0$, since

$$\lim_{r\to 0} \frac{[\alpha_{qq}]^{N_f=2} - [\alpha_{qq}]^{N_f=0}}{[\alpha_{qq}]^{N_f=0}} = \frac{b_0(N_f = 0)}{b_0(N_f = 2)} - 1 \approx 0.1379. \tag{5.27}$$

Eq. (5.27) is a simple consequence of the asymptotic behavior $\alpha_{qq}(r) = 1/[4\pi b_0 \log(r^{-2}\Lambda^{-2})]$ for distances $r \to 0$ (see Section 2.1.3).

[9] We remind that the smallest value of the coupling that we can reach with our finest lattice is $\alpha_{qq} \approx 0.20$.

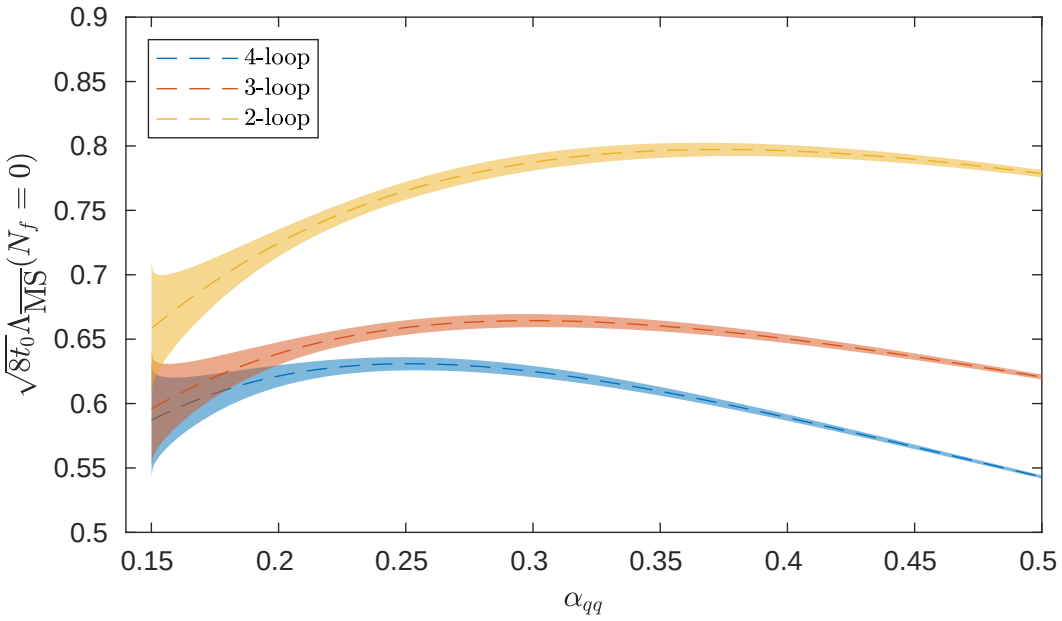

Figure 5.13 Λ parameter of $N_f = 0$ QCD obtained with the 2-, 3- and 4-loop perturbative expansions of β_{qq} and our continuum extrapolation of g_{qq}.

Using $r_0/\sqrt{t_0} = 3.013(17)$ [88] we can rewrite our estimate of Λ in units of r_0

$$\left[r_0\Lambda_{\overline{\rm MS}}(N_f = 0)\right]_{\alpha_{qq}=0.15} = 0.625(47). \tag{5.31}$$

Our (indicative) result is compatible with the value $r_0\Lambda_{\overline{\rm MS}}(N_f = 0) = 0.602(48)$ obtained in Ref. [128].

Chapter 6

Charm sea effects on charmonium systems and RGI mass

In this chapter we present the results of our numerical simulations concerning the study of charmonium states. Since our simplified setup (see Section 4.7) gives the opportunity to explore lattice spacings much smaller than the ones used nowadays for QCD simulations at the physical point, we can determine through careful continuum extrapolations the impact of a dynamical charm quark on charmonium masses, RGI mass and decay constants. Part of the study that we show here has also been presented in Refs. [122, 131, 132].

6.1 Computing meson masses and decay constants

Meson masses and decay constants are extracted through the computation of the two-point correlation functions (4.24). After Wick contractions, the computation of the meson correlators requires the evaluation of traces of matrices, that we compute making use of stochastic time-diluted estimators with 16 U(1) noise vectors, as explained in Section 4.1.2.

The ground state energy is determined by the weighted plateau average of the effective mass (Eqs. (4.15) and (4.17)) while the pseudoscalar and vector decay constants are computed through Eqs. (4.70), (4.71), (4.72) and (4.73) to remove the boundary effects from our lattice calculations. As already mentioned in Section 4.2, the calculation of f_{η_c} does not need any renormalization factor, while for $f_{J/\psi}$ we need to multiply the relevant matrix element by the renormalization factor Z_A of the axial current, which is known from Refs. [133–135] for the ensembles considered here. Note that the computation of R_X in Eq. (4.70) requires the knowledge of a *boundary-boundary correlator* of the type $f_X(T-y_0,y_0)$. However, when source and sink are far from each other, a determination of the meson correlator at a good accuracy is very difficult to achieve, because the relative precision of the solution of the Dirac equation deteriorates at large distances and this becomes much more prominent for heavy quark masses. This is due to the exponential decay of the heavy quark propagator, which is proportional to $\exp[-m_h(x_0-y_0)]$, where m_h is the mass of the heavy quark. To overcome this problem, we use the *distance preconditioning* for the Dirac operator proposed in Refs. [136, 137]. The idea is to rewrite the original linear system in such a way that the

solution of the new system at time-slices x_0 far away from the source is enhanced by an exponential factor $e^{\alpha_0(x_0-y_0)}$, which compensates the rapid decay of the quark propagator. α_0 is a parameter that needs to be tuned for each ensemble studying the *local residual*

$$r_{loc}(x_0-y_0) = \frac{\left|\frac{1}{L^3}\sum_{\vec{y}}[D(y,x)\psi(x)-\eta(y)]\right|}{\left|\frac{1}{L^3}\sum_{\vec{x}}\psi(x)\right|} \tag{6.1}$$

at the time separation of interest ($T-2y_0$ in our case, from Eq. (4.70)). In Eq. (6.1) $D(y,x)$ is the Dirac operator, while $\psi(x)$ and $\eta(y)$ denote the solution and the source respectively. The price to pay when using this algorithm is an increase of the computational costs. As can be seen in Figure 6.1, the solution becomes more and more accurate as α_0 increases. However, in this example we observe that for the solution to have a local residual $< 10^{-5}$ for all time-slices (which is enough given our statistical accuracy of the meson correlator) the number of solver iterations increases of around a factor 5 compared to the case $\alpha_0 = 0$ (no distance preconditioning applied).

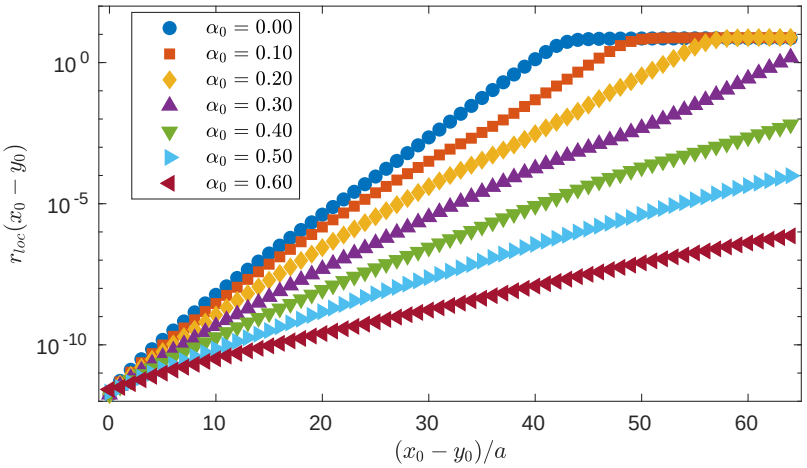

α_0	Iterations
0.00	265
0.10	287
0.20	335
0.30	411
0.40	536
0.50	768
0.60	1296

Figure 6.1 Tuning of the parameter α_0 of the distance preconditioning method for our coarsest lattice ($N_f = 2$, $\beta = 5.3$, see Table 4.2). We show the relative residual of the solution ψ as a function of the sink position x_0 with respect to the source set at $y_0/a = 16$. On the right, the number of iterations for the solver to converge is reported for the values of α_0 plotted in the Figure.

Such a small value of the residual is crucial to extract the meson correlator (and as a consequence the meson decay constants) reliably. Ideally one would choose $y_0 = a$, but to keep the computational effort as small as possible, we explored different source positions (with $y_0 > a$) to ensure the ground state dominance over a large range of time-slices and a reasonable number of iterations for the solver to converge.

Some examples of the calculation of meson masses and decay constants are shown in Figures 6.2 and 6.3. In particular, Figure 6.2 shows the effective masses and the plateau averages for the $N_f = 2$ ensemble with $\beta = 6$, whilst in Figure 6.3 we report the measurement, performed on the same ensemble, of the effective quantity R_P defined in Eq .(4.70). As can be seen, our numerical setup allows to take the plateau averages for a large range of time slices and this is crucial to determine the size of the charm sea effects with great accuracy.

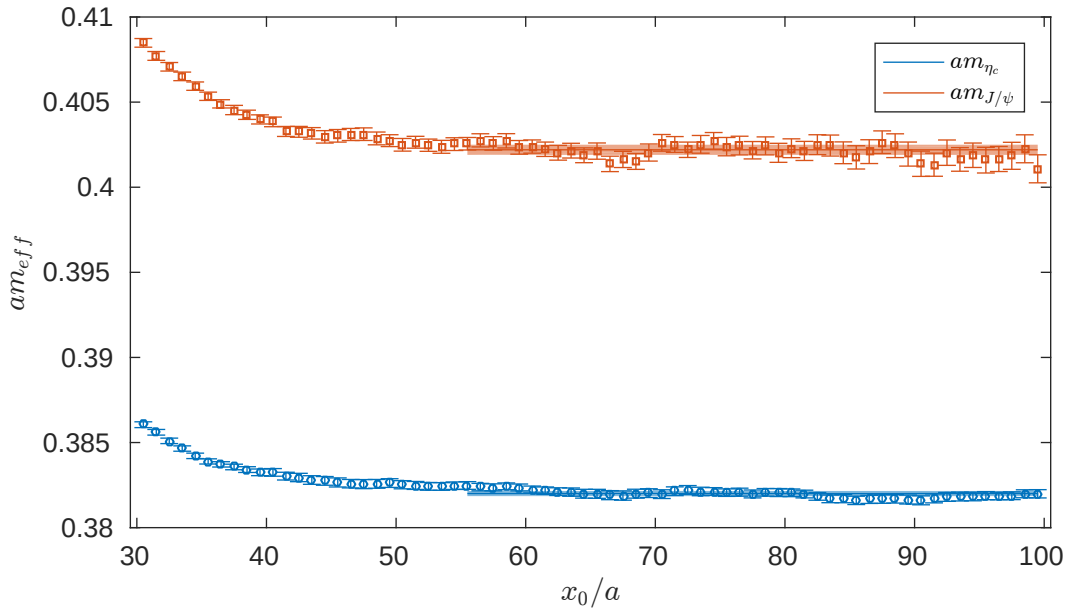

Figure 6.2 Effective masses and plateau averages for the mesons η_c (circles) and J/ψ (squares) on the $N_f = 2$ ensemble at $\beta = 6.0$.

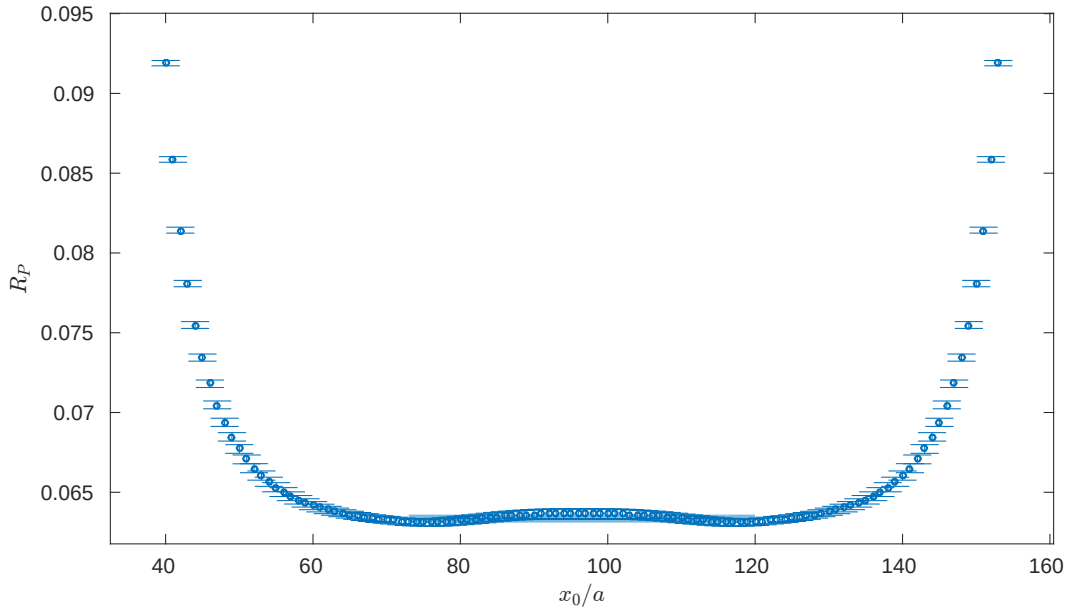

Figure 6.3 Extraction of the effective quantity R_P defined in Eq. (4.70) on the $N_f = 2$ ensemble at $\beta = 6.0$. The plateau average of R_P (blue band) allows to extract the pseudoscalar decay constant f_{η_c} through Eq. (4.72).

6.2 Tuning of the twisted mass parameter

To match $N_f = 0$ and $N_f = 2$ QCD we use the low energy observable $m^{had} = 1/\sqrt{t_0}$. For such observable decoupling applies [16, 17] and we can assume $\sqrt{t_0}|_{N_f=0} = \sqrt{t_0(M_c)}|_{N_f=2}$. However, if we want to compare the two theories we also need to fix the RGI mass M_c of the charm quark. Here, we choose a value of M_c such that for each lattice spacing explored (see Table 4.2) $\sqrt{t_0}m_{\eta_c}$ approximately corresponds to its physical value and it assumes the same value in $N_f = 0$ and $N_f = 2$ QCD. In order to do that, we proceed as described below.

On our finest $N_f = 2$ lattice, the RGI mass M_c of the charm quark is fixed by the relation

$$M_c/\Lambda_{\overline{\rm MS}} = 4.87, \tag{6.2}$$

where we use the preliminary value $M_c = 1510$ MeV of Ref. [130] (which agrees with Ref. [18]) and the 2 flavor Lambda parameter $\Lambda_{\overline{\rm MS}} = 310(20)$ MeV known from [117]. Since on our $N_f = 2$ ensembles the hopping parameter κ is set to its critical value, the renormalized physical quark mass (3.84) is simply given by $m_R = Z_P^{-1}\mu$ and the condition (6.2) is equivalent to fix the twisted mass parameter through

$$a\mu = \frac{M_c}{\Lambda_{\overline{\rm MS}}} \times Z_P(L_1^{-1}) \times \frac{m_R(L_1)}{M_c} \times \Lambda_{\overline{\rm MS}} L_1 \times \frac{a}{L_1}. \tag{6.3}$$

In the equation above, the value of the pseudoscalar renormalization constant Z_P at the renormalization scale L_1^{-1} in the Schrödinger Functional scheme

$$Z_P(L_1) = 0.5184(33) \quad \text{valid for } 5.2 \leq \beta \leq 6, \tag{6.4}$$

and the relation between the running mass $m_R(L_1)$ and the RGI mass

$$\frac{M}{m_R(L_1)} = 1.308(16) \tag{6.5}$$

are known from Refs. [117, 138]. As a value of the Λ parameter of the 2 flavor theory in L_1 units we take [139]

$$\Lambda_{\overline{\rm MS}} L_1 = 0.649(45), \tag{6.6}$$

whilst the ratio L_1/a is known from [46]. Taking into account the errors in the factors of Eq. (6.3), we can fix the charm quark mass only up to about 10% precision. This is however fully sufficient for us, as long as the relative mass differences between the different ensembles are under better control. To achieve this, we do not use Eq. (6.3) at the other lattice spacings. Instead, we tune the twisted mass parameter to a point $\mu^\star$ such that the renormalized quantity $\sqrt{t_0} m_{\eta_c}$ satisfies

$$\sqrt{t_0} m_{\eta_c}(\mu^\star) \equiv 1.807463, \tag{6.7}$$

which is independent of the overall scale $\Lambda_{\overline{\rm MS}}$ (known with a 7% accuracy) and corresponds (see Table 4.2) to the value obtained on our finest $N_f = 2$ lattice using the twisted mass parameter originating from Eq. (6.3).

6.2.1 Mass shifts

The tuning of the twisted mass parameter can only be carried out to a limited precision, at most to within the statistical errors. To account for the mis-tuning, a correction is applied to all observables, which is based on the computation of twisted mass derivatives. First the

target tuning point $\mu^\star$ is determined through the Taylor expansion

$$\mu^\star = \mu + (\sqrt{t_0} m_{\eta_c} - 1.807463) \left(\frac{d\sqrt{t_0} m_{\eta_c}}{d\mu} \right)^{-1} \tag{6.8}$$

and subsequently all quantities, denoted by A below, are corrected by

$$A(\mu^\star) = A(\mu) + (\mu^\star - \mu) \frac{dA}{d\mu}. \tag{6.9}$$

For a generic primary observable A, its twisted mass derivative is given by[1]

$$\frac{d\langle A \rangle}{d\mu} = -\left\langle \frac{dS}{d\mu} A \right\rangle + \left\langle \frac{dS}{d\mu} \right\rangle \langle A \rangle + \left\langle \frac{dA}{d\mu} \right\rangle, \tag{6.10}$$

where S is the lattice QCD action. For a doublet χ of twisted mass Wilson fermions, see Eq. (3.65), the derivative of the action reads

$$\frac{dS}{d\mu} = \sum_x \bar{\chi}(x) i\gamma_5 \tau_3 \chi(x). \tag{6.11}$$

Most quantities we are interested in are non-linear functions of various primary observables (e.g. meson masses, which are extracted through the plateau average (4.17) and, as a consequence, depend on suitable meson correlators (see Section 4.1.1) computed at various distances in the plateau). For such observable the chain rule dictates

$$\frac{df(\langle A_1 \rangle, \ldots, \langle A_N \rangle, \mu)}{d\mu} = \frac{\partial f}{\partial \mu} + \sum_{i=1}^{N} \frac{\partial f}{\partial \langle A_i \rangle} \frac{d\langle A_i \rangle}{d\mu}. \tag{6.12}$$

None of the observables that we consider have an explicit μ dependence, so the last term in Eq. (6.10) is absent.

When A is a purely gluonic observable, $A \equiv A[U]$, the first term of Eq. (6.10) is (for the notation see Section 4.1.2)

$$\begin{aligned} -\left\langle \frac{dS}{d\mu} A \right\rangle &= -i \sum_x \langle [\bar{\tilde{c}}_1(x)\gamma_5 \tilde{c}_1(x) - \bar{\tilde{c}}_2(x)\gamma_5 \tilde{c}_2(x)] A[U] \rangle \\ &= -i \sum_x \langle \mathrm{Tr}[\gamma_5 (S_2(x,x) - S_1(x,x))] A[U] \rangle_G \\ &= 2\mu \sum_{x,y} \left\langle \mathrm{Tr} \left[S_1^\dagger(x,y) S_1(y,x) \right] A[U] \right\rangle_G . \end{aligned} \tag{6.13}$$

The last line is a consequence of the following relation between the twisted mass Dirac operators D_1 and D_2 of the quark fields $\tilde{c}_1$ and $\tilde{c}_2$

$$D_1 - D_2 = 2i\gamma_5 \mu \quad \Rightarrow \quad S_2 - S_1 = 2i\mu S_1 \gamma_5 S_2. \tag{6.14}$$

[1] This can be easily shown from the path integral definition of $\langle A \rangle$ (see Eq. 3.96).

We compute the trace in Eq. (6.13) through the stochastic estimation discussed in Section 4.1.2. Indeed, any noise vector of the type (4.27) allows to write

$$\sum_{x,y} \mathrm{Tr}\left[S_1^\dagger(x,y)S_1(y,x)\right] = \sum_x \langle [S_1\eta]^\star_{\alpha a}(x)[S_1\eta]_{\alpha a}(x)\rangle_\eta . \tag{6.15}$$

We found that 64 $U(1)$ noise vectors are enough for the errors in the determination of the derivative to be dominated by gauge-noise, rather than the noise from the stochastic trace evaluation.

If the observables depend on fermionic fields too, the first term of Eq. (6.10) gives rise to new contractions that have to be computed. These are different for different fermionic observables. In the case of the two-point functions (4.24), we find contractions of the form

$$\frac{ia^6}{L^3}\sum_{\vec{x},\vec{y},z} \left\langle \mathrm{Tr}\left[\gamma_5(S_1(z,z)-S_2(z,z))\right]\mathrm{Tr}\left[\Gamma_A S_2(x,y)\bar{\Gamma}_B S_1(y,x)\right]\right\rangle_G , \tag{6.16}$$

that can be immediately computed because both traces have already been estimated for the evaluation of the correlator and of $dS/d\mu$ respectively, and new terms

$$\frac{ia^6}{L^3}\sum_{\vec{x},\vec{y},z} \left\langle \mathrm{Tr}\left[\gamma_5 S_2(z,y)\bar{\Gamma}_B S_1(y,x)\Gamma_A S_2(x,z)\right] - \mathrm{Tr}\left[\gamma_5 S_1(z,x)\Gamma_A S_2(x,y)\bar{\Gamma}_B S_1(y,z)\right]\right\rangle_G \tag{6.17}$$

that require some attention. It is easy to show that these new terms can be computed through the twisted mass derivative of the meson correlator (4.24) after performing Wick contractions (see Section 4.1.3). Indeed

$$\begin{aligned}
&\frac{d}{d\mu}\left[\frac{a^6}{L^3}\sum_{\vec{x},\vec{y}}\left\langle \mathrm{Tr}\left[\Gamma_A S_2(x,y)\bar{\Gamma}_B S_1(y,x)\right]\right\rangle_G\right] = \\
&\frac{a^6}{L^3}\sum_{\vec{x},\vec{y}}\left\langle \mathrm{Tr}\left[\Gamma_A\frac{dS_2(x,y)}{d\mu}\bar{\Gamma}_B S_1(y,x) + \Gamma_A S_2(x,y)\bar{\Gamma}_B\frac{dS_1(y,x)}{d\mu}\right]\right\rangle_G = \\
&\frac{ia^6}{L^3}\sum_{\vec{x},\vec{y},z} \left\langle \mathrm{Tr}\left[\gamma_5 S_2(z,y)\bar{\Gamma}_B S_1(y,x)\Gamma_A S_2(x,z)\right] - \mathrm{Tr}\left[\gamma_5 S_1(z,x)\Gamma_A S_2(x,y)\bar{\Gamma}_B S_1(y,z)\right]\right\rangle_G ,
\end{aligned} \tag{6.18}$$

where we use the fact that

$$S_1 = [D+m_0+i\mu\gamma_5]^{-1} \quad \Rightarrow \quad \frac{dS_1}{d\mu} = -iS_1\gamma_5 S_1 , \tag{6.19}$$

$$S_2 = [D+m_0-i\mu\gamma_5]^{-1} \quad \Rightarrow \quad \frac{dS_2}{d\mu} = iS_2\gamma_5 S_2 . \tag{6.20}$$

We compute the twisted mass derivatives (6.18) using stochastic techniques, as explained in Section 4.1.3. For such calculations we have seen that 16 $U(1)$ noise vectors allow to determine the derivatives (6.18) with satisfactory accuracy.

Note that in Eqs. (6.8) and (6.9) we assume that the initial tuning was precise enough for the omitted quadratic terms to be negligible, compared to the statistical precision. Figure 6.4

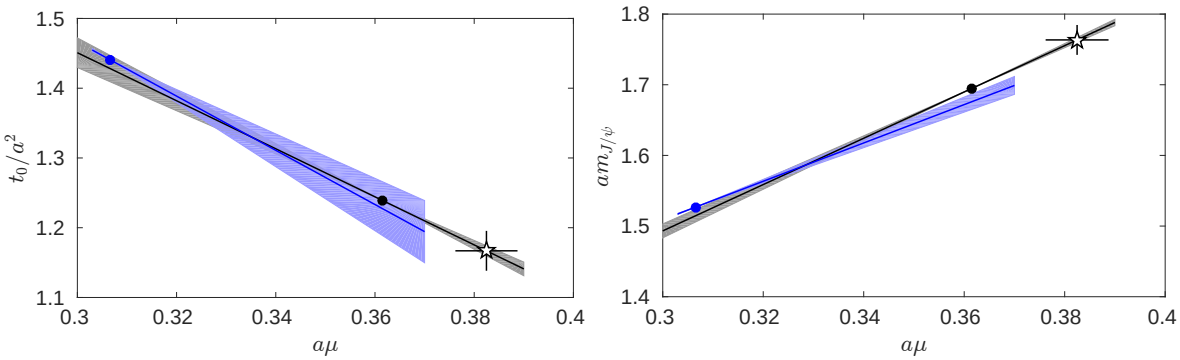

Figure 6.4 The solid black and blue markers are direct simulation results for t_0/a^2 (left) and $am_{J/\psi}$ (right) on our coarsest ensembles with $\beta = 5.3$. The simulations were carried out at slightly different masses, namely $a\mu = 0.36151$ (black) and $a\mu = 0.30651$ (blue). The lines, with their respective error bands illustrate the value and error of the derivative of the observable with respect to the twisted mass parameter. The black pentagram depicts the values obtained at the tuning point where $\sqrt{t_0}m_{\eta_c} = 1.8$ (we will use the tuning point (6.7) in our final calculations). Its vertical error bar is the complete error, including all correlations, while the horizontal error bar is the uncertainty on $\mu^\star$.

demonstrates the procedure for a purely gluonic observable like t_0 and for the vector mass $m_{J/\psi}$, which depends on the fermion fields. A comparison with direct simulations indicates that even for large shifts of $\approx 15\%$ in $a\mu$ the linear approximation works well. For the $N_f = 2$ ensembles of Table 4.2 the shifts in $a\mu$ with respect to the tuning point (6.7) are at most 6%.

In a pure gauge theory the action does not depend on the quark masses and we need the twisted mass parameter μ only for the inversion of the Dirac operator. Thus, to reproduce the tuning value $\mu^\star$ (6.7) for our $N_f = 0$ ensembles, we carry out the measurements at three different values of the twisted mass parameter μ and the tuning point $\mu^\star$ is found through a linear interpolation of the measurements. An example of this procedure is shown in Figure 6.5. The critical hopping parameters have been obtained through an interpolation of the values of κ_c reported in Ref. [71]. In this last reference, also the dependence of the clover coefficient $c_{SW}^{N_f=0}$ on the bare coupling g_0 has been computed and is reported here in Eq. (3.55).

6.2.2 Data analysis

All the statistical errors shown in this chapter have been determined with the Matlab package *UWerr.m* [77]. Note that observables like the effective masses (4.15) or the effective quantity R_X (4.70), which are needed to determine the meson decay constants, are non-linear functions of "primary observables", i.e. the meson correlators. When incorporating the mistuning corrections (6.8) and (6.9), the necessary nonlinear functions can become quite unwieldy. For instance, the vector meson mass $\sqrt{t_0}m_{J/\psi}$ at $\mu^\star$ depends on $\sqrt{t_0}$ (which in turn is not a primary observable), on the vector correlator in the plateau region, but also on the pseudoscalar correlator in its plateau region, since

$$\begin{aligned}\sqrt{t_0}m_{J/\psi}(\mu^\star) &= \sqrt{t_0}m_{J/\psi} + (\mu^\star - \mu)\frac{d\sqrt{t_0}m_{J/\psi}}{d\mu} \\ &= \sqrt{t_0}m_{J/\psi} + (\sqrt{t_0}m_{\eta_c} - 1.807463)\left(\frac{d\sqrt{t_0}m_{\eta_c}}{d\mu}\right)^{-1}\frac{d\sqrt{t_0}m_{J/\psi}}{d\mu}.\end{aligned} \tag{6.21}$$

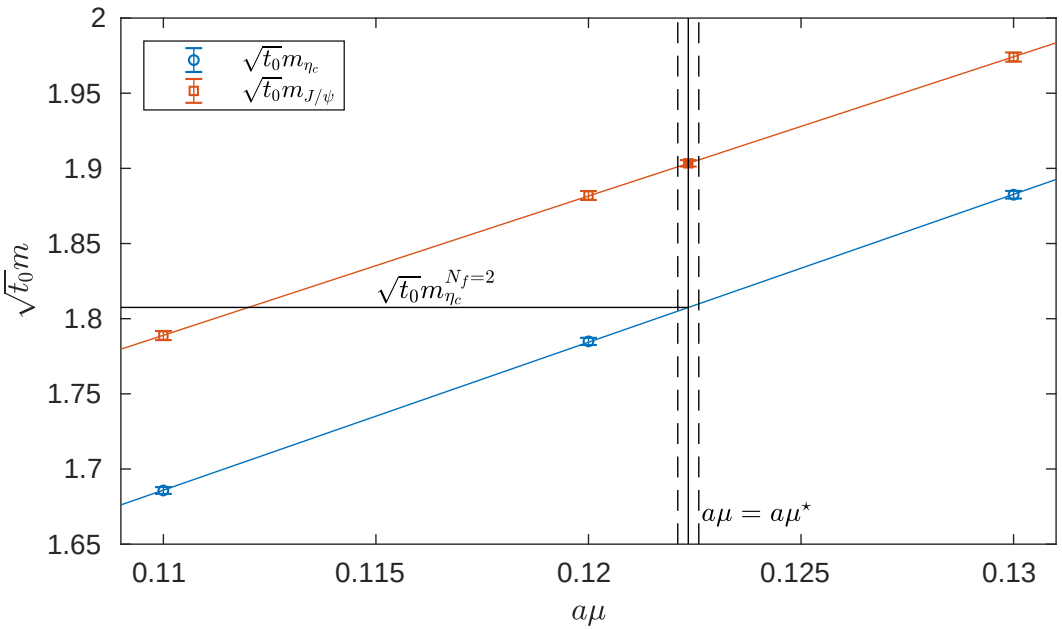

Figure 6.5 Interpolation of the measured pseudoscalar masses (blue circles) on the $N_f = 0$ ensemble at $\beta = 6.34$. The horizontal line depicts the tuning point. The vertical lines are the resulting interpolated twisted mass parameter $a\mu^\star$ and its statistical error. The measured vector meson masses (red squares) can then be interpolated to the tuning point, resulting in the solid square point. In the error bars all the correlations among the data have been taken into account.

Furthermore, because of Eqs. (6.10) and (6.12), $\sqrt{t_0}m_{J/\psi}(\mu^\star)$ is also a function of the μ-derivatives of pseudoscalar and vector correlators, of the μ-derivative of the action and of the μ-derivative of the action times the correlators. The analysis can be simplified using the chain rule for computing the derivatives of composition of functions.

For the quenched measurements the analysis is a bit simpler. If we still consider the case of $\sqrt{t_0}m_{J/\psi}$, we compute $\sqrt{t_0}m_{J/\psi}$ and $\sqrt{t_0}m_{\eta_c}$ for three values of μ. Then, through a linear fit

$$\sqrt{t_0}m_{\eta_c}(\mu) = c_1 a\mu + c_2, \tag{6.22}$$

$$\sqrt{t_0}m_{J/\psi}(\mu) = c_3 a\mu + c_4, \tag{6.23}$$

one can determine the parameters c_i and their covariance matrix[2]. Thus, the tuning point $\mu^\star$ is given by

$$a\mu^\star = \frac{1.807463 - c_2}{c_1}, \tag{6.24}$$

while the value of the vector mass at the tuning point $\mu^\star$ reads

$$\sqrt{t_0}m_{J/\psi}(\mu^\star) = c_3 \left(\frac{1.807463 - c_2}{c_1} \right) + c_4. \tag{6.25}$$

Finally, the statistical errors of $\sqrt{t_0}m_{J/\psi}(\mu^\star)$ and $a\mu^\star$ can be found through standard error propagations.

[2]The covariances are not needed if we implement the μ-shifts as a single complicated function of the primary observables.

Eqs. (6.21) and (6.25) can be easily generalized to any other observable, like mass ratios, decay constants, RGI masses, other meson masses, etc. and summarize our strategy to evaluate all the observables we are interested in at the tuning point $\mu^\star$ defined in Eq. (6.7).

6.3 Results

In this section we show the main results of our study. In particular, we focus on:

1. the lightest masses of charmonium spectrum, i.e. the pseudoscalar and vector masses m_{η_c} and $m_{J/\psi}$;
2. the hyperfine splitting $(m_{J/\psi} - m_{\eta_c})/m_{\eta_c}$;
3. the decay constants f_{η_c} and $f_{J/\psi}$;
4. the RGI mass M_c of a charm quark.

6.3.1 Meson masses and hyperfine splitting

Before carrying out the continuum extrapolations we analyzed the discretization effects of our measurements at finite lattice spacing. As example of this investigation, in Figure 6.6 we present our study of the lattice artifacts for the vector mass $m_{J/\psi}$ in $N_f = 2$ QCD.

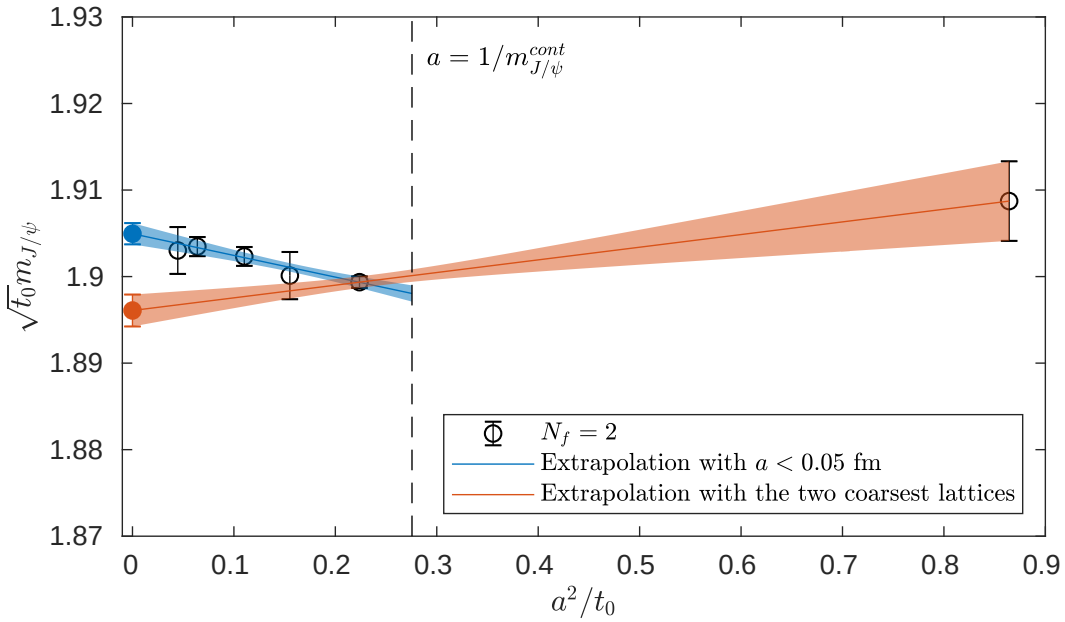

Figure 6.6 Continuum extrapolations (linear in a^2) of $\sqrt{t_0} m_{J/\psi}$ using the two coarsest lattices (red band) and the five finest lattices (blue band) listed in the first six rows of Table 4.2.

We clearly see that beyond $a^2/t_0 \approx 0.8$, which corresponds to $a \approx 0.06 - 0.07$ fm, the discretization effects become considerable. This behavior is somehow expected, since at these lattice spacings the condition $am_{J/\psi} < 1$ is no longer satisfied. Similar discretization effects for these values of the lattice spacing were also found in Ref. [140] in the context of a precision computation of the D_s meson decay constant in quenched QCD. Moreover, in the

same figure two different continuum extrapolations are shown: one with our two coarsest lattice spacings, $a = 0.049$ fm and $a = 0.066$ fm (red band), and one with five lattice spacings in the range $0.023 \text{ fm} \leq a \leq 0.049$ fm (blue band). As can be seen, we find a non-trivial dependence on the lattice spacing and that lattice spacings $a \lesssim 0.05$ fm have to be employed to obtain reliable continuum extrapolations at 1% precision. Thus, we decide not to include the coarsest $N_f = 2$ lattice at $\beta = 5.3$ (see Table 4.2) for the final continuum extrapolations.

In Figures 6.7 and 6.8 we compare the continuum limits of $\sqrt{t_0} m_{J/\psi}$ and of the hyperfine splitting $(m_{J/\psi} - m_{\eta_c})/m_{\eta_c}$ in $N_f = 0$ and $N_f = 2$ QCD. As can be seen from a comparison

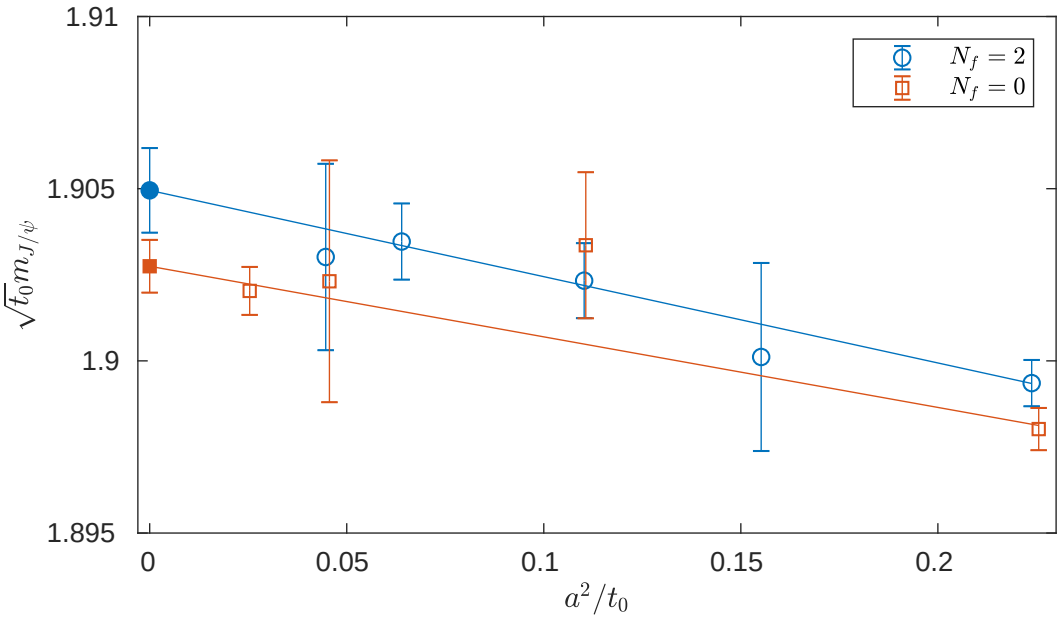

Figure 6.7 Continuum extrapolation of $\sqrt{t_0} m_{J/\psi}$ in $N_f = 0$ and $N_f = 2$ QCD for $\sqrt{t_0} m_{\eta_c}|_{N_f=2} = \sqrt{t_0} m_{\eta_c}|_{N_f=0} = 1.807463$, performed with lattice spacings $0.02 \text{ fm} \lesssim a \lesssim 0.05$ fm.

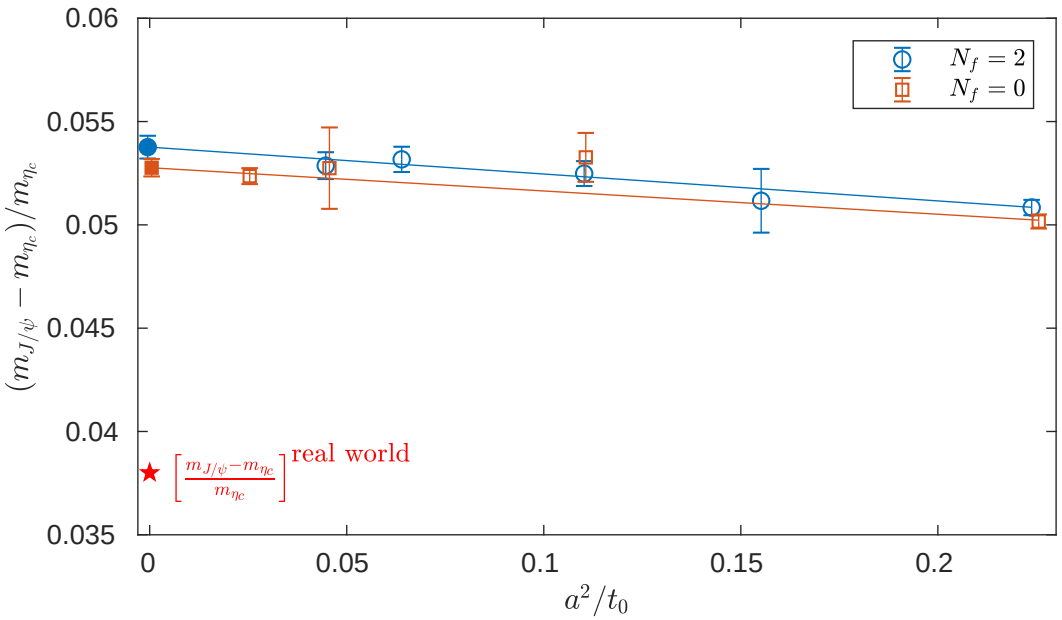

Figure 6.8 Continuum extrapolation of the hyperfine splitting $(m_{J/\psi} - m_{\eta_c})/m_{\eta_c}$ in $N_f = 0$ and $N_f = 2$ QCD for $\sqrt{t_0} m_{\eta_c}|_{N_f=2} = \sqrt{t_0} m_{\eta_c}|_{N_f=0} = 1.807463$, performed with lattice spacings $0.02 \text{ fm} \lesssim a \lesssim 0.05$ fm.

of the values obtained in the continuum (full markers), dynamical charm effects on these observables are barely resolvable, although the great accuracy of our extrapolations to zero lattice spacing. In particular, we obtain the following relative effects

$$\frac{\left[\sqrt{t_0}m_{J/\psi}\right]^{N_f=2} - \left[\sqrt{t_0}m_{J/\psi}\right]^{N_f=0}}{\left[\sqrt{t_0}m_{J/\psi}\right]^{N_f=0}} = 0.00116(76), \tag{6.26}$$

$$\frac{\left[(m_{J/\psi} - m_{\eta_c})/m_{\eta_c}\right]^{N_f=2} - \left[(m_{J/\psi} - m_{\eta_c})/m_{\eta_c}\right]^{N_f=0}}{\left[(m_{J/\psi} - m_{\eta_c})/m_{\eta_c}\right]^{N_f=0}} = 0.019(13). \tag{6.27}$$

The discrepancy between our continuum estimates of the hyperfine splitting with its physical value is probably due to effects of light sea quarks, disconnected contributions and electromagnetism that are neglected in this work.

6.3.2 Decay constants

In principle, from the correlators used to compute pseudoscalar and vector masses, we could also extract the meson decay constants f_{η_c} and $f_{J/\psi}$. However, as we already mentioned in Section 6.1, a correct estimate of the effective quantity R_X (4.70) requires the use of the distance preconditioning method for the Dirac operator, which leads to a considerable increase of the computational costs. For such reasons, the measurements of these observables are still in progress and the results shown here are intended to be preliminary.

In Figure 6.9 we present the results for the observable $\sqrt{t_0}f_{\eta_c}$ in $N_f = 2$ QCD. As can

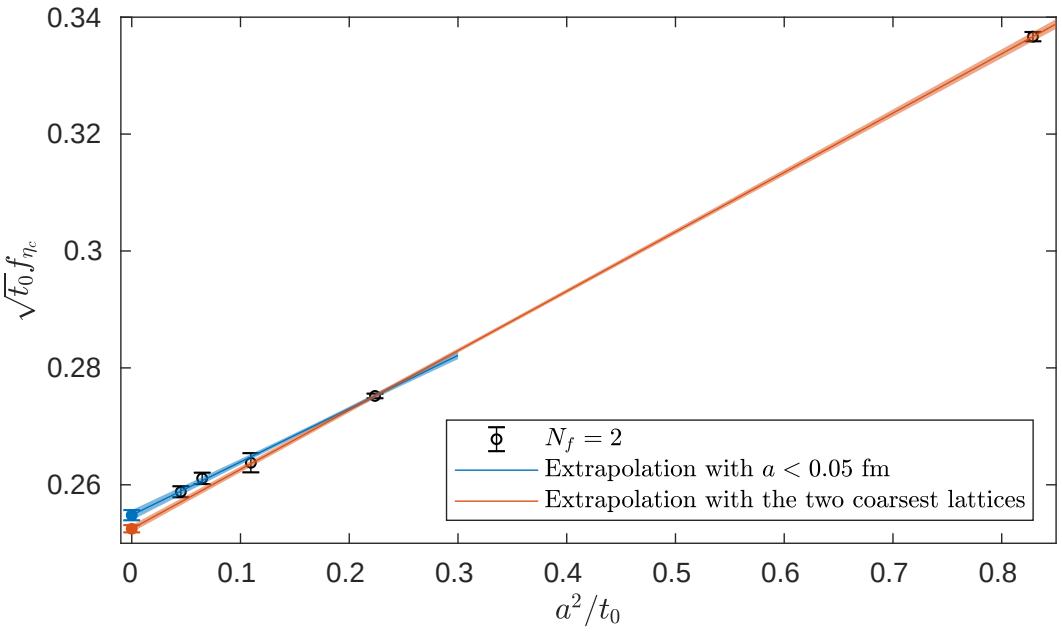

Figure 6.9 Continuum extrapolations (linear in a^2) of $\sqrt{t_0}f_{\eta_c}$ using the two coarsest lattices (red band) and four lattices (blue band) with 0.02 fm $\lesssim a \lesssim$ 0.05 fm (see Table 4.2).

be seen, we reach a sub-percent accuracy at every lattice spacing explored, which allows to perform a careful study of the lattice artifacts. Similarly to what observed for $\sqrt{t_0}m_{J/\psi}$ in the previous section, we find that linear fits in a^2 do not work well in the range of lattice spacings

0.02 fm $\lesssim a \lesssim$ 0.07 fm, if one aims at measurements with 1% precision. Therefore, we compare the continuum limits of $\sqrt{t_0} f_{\eta_c}$ and $\sqrt{t_0} f_{J/\psi}$ in $N_f = 0$ and $N_f = 2$ QCD, performing extrapolations to zero lattice spacing only in the range 0.02 fm $\lesssim a \lesssim$ 0.05 fm. This study is shown in Figures 6.10 and 6.11. As can be seen in Figure 6.10, the current status of our measurements of $\sqrt{t_0} f_{\eta_c}$ in $N_f = 0$ QCD shows a non-clear linear behavior in a^2 (solid red line), with $\chi^2/N_{dof} \approx 2$. On the other hand, the two measurements at the two finest lattice spacings seem well approximated by a constant fit (dashed red line), with $\chi^2/N_{dof} \approx 0.37$. For these reasons, at the moment we prefer to give only an indicative estimate of the continuum limit in $N_f = 0$ QCD (full red diamond), whose error bar covers the range of values obtained with a linear and constant fit in a^2 (full red upward- and downward-pointing triangle respectively).

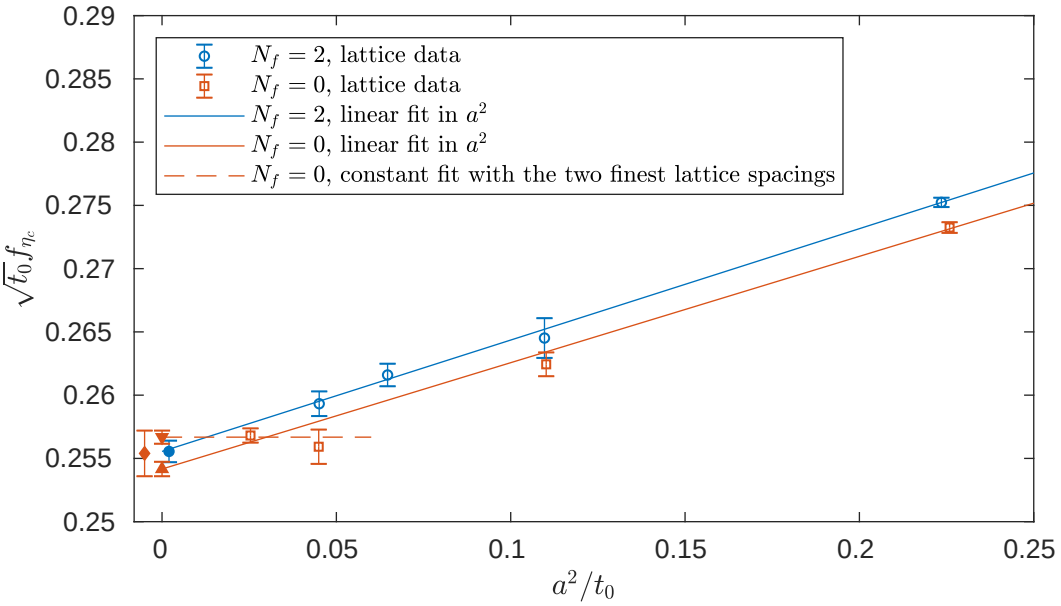

Figure 6.10 Continuum extrapolation of $\sqrt{t_0} f_{\eta_c}$ in $N_f = 0$ and $N_f = 2$ QCD for $\sqrt{t_0} m_{\eta_c}|_{N_f=2} = \sqrt{t_0} m_{\eta_c}|_{N_f=0} = 1.807463$, performed with lattice spacings 0.02 fm $\lesssim a \lesssim$ 0.05 fm.

This preliminary study seems to confirm that even for the meson decay constants f_{η_c} and $f_{J/\psi}$ the impact of dynamical charm quarks is extremely small, as we find

$$\frac{\left[\sqrt{t_0} f_{\eta_c}\right]^{N_f=2} - \left[\sqrt{t_0} f_{\eta_c}\right]^{N_f=0}}{\left[\sqrt{t_0} f_{\eta_c}\right]^{N_f=0}} = 0.0006(78), \tag{6.28}$$

$$\frac{\left[\sqrt{t_0} f_{J/\psi}\right]^{N_f=2} - \left[\sqrt{t_0} f_{J/\psi}\right]^{N_f=0}}{\left[\sqrt{t_0} f_{J/\psi}\right]^{N_f=0}} = 0.013(14). \tag{6.29}$$

Since the ratios above are smaller then their statistical uncertainties, we conclude that the charm loop effects on $\sqrt{t_0} f_{\eta_c}$ and $\sqrt{t_0} f_{J/\psi}$ do not exceed 0.78% and 1.4% respectively.

6.3.3 RGI mass

Finally, we present our results for the RGI quark mass M_c. For such calculation, we first determine the continuum limit of the running mass m_R in $N_f = 0$ and $N_f = 2$ QCD. Since we

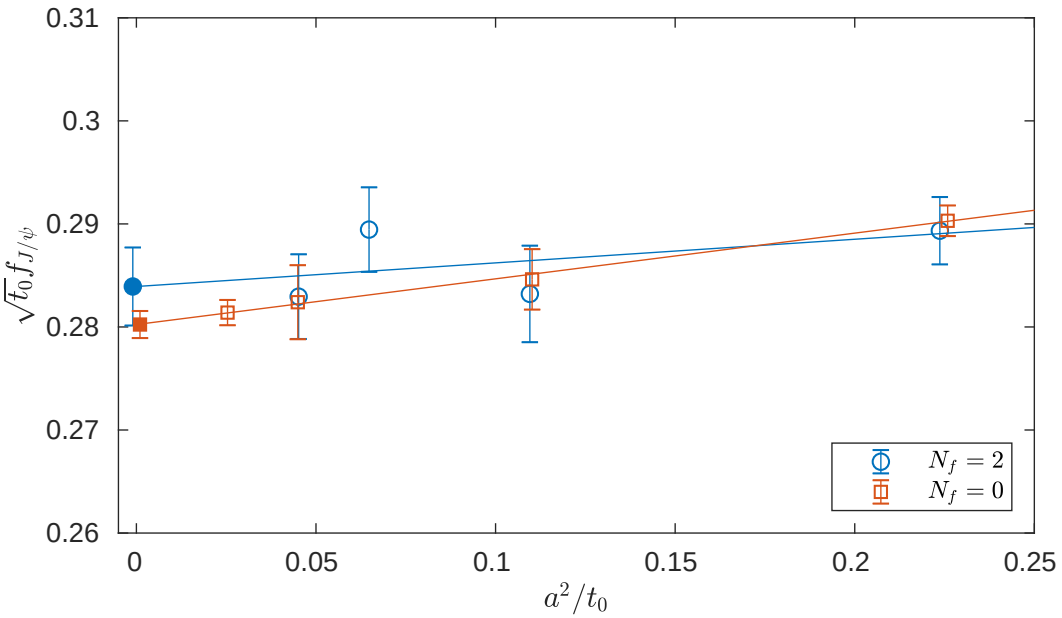

Figure 6.11 Continuum extrapolation of $\sqrt{t_0} f_{J/\psi}$ in $N_f = 0$ and $N_f = 2$ QCD for $\sqrt{t_0} m_{\eta_c}|_{N_f=2} = \sqrt{t_0} m_{\eta_c}|_{N_f=0} = 1.807463$, performed with lattice spacings 0.02 fm $\lesssim a \lesssim$ 0.05 fm.

are at maximal twist, m_R is entirely given by the twisted mass parameter at the tuning point $\mu^\star$, i.e.

$$m_R = \frac{1}{Z_P} \mu^\star. \tag{6.30}$$

The renormalization factors Z_P of the pseudoscalar current have been determined for $N_f = 0$ and $N_f = 2$ QCD in Refs. [141, 117]. In Figure 6.12 we show the extrapolation to zero lattice spacing for the dimensionless quantity $\sqrt{t_0} m_R$. The results of these continuum extrapolations

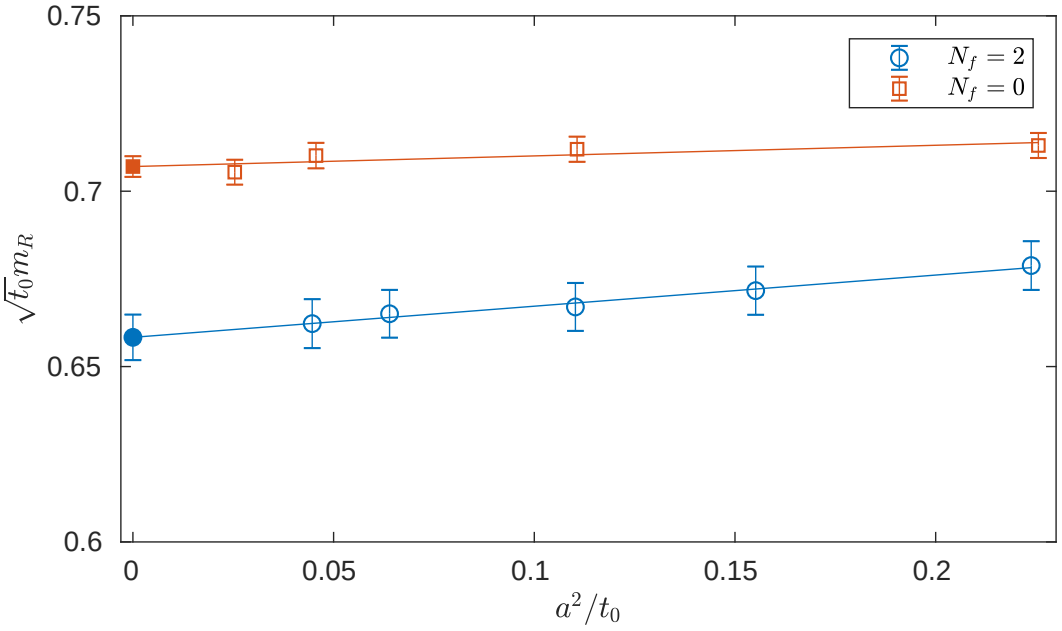

Figure 6.12 Continuum extrapolation of $\sqrt{t_0} m_R$ in $N_f = 0$ and $N_f = 2$ QCD for $\sqrt{t_0} m_{\eta_c}|_{N_f=2} = \sqrt{t_0} m_{\eta_c}|_{N_f=0} = 1.807463$, performed with lattice spacings 0.02 fm $\lesssim a \lesssim$ 0.05 fm.

can be easily translated into the RGI mass, since also the ratios M/m_R are known in both

theories [141, 117]. The final results for $\sqrt{t_0}M_c$ in the continuum limit are shown in Table 6.1.

	$N_f = 0$	$N_f = 2$
$\sqrt{t_0}M_c$	0.8180(91)	0.861(14)

Table 6.1 Continuum values of $\sqrt{t_0}M_c$ in $N_f = 0$ and $N_f = 2$ QCD for $\sqrt{t_0}m_{\eta_c}|_{N_f=2} = \sqrt{t_0}m_{\eta_c}|_{N_f=0} = 1.807463$.

We remind that the RGI mass M_c is both scale and scheme independent, therefore it makes sense to compare the continuum limits obtained in $N_f = 0$ and $N_f = 2$ QCD for this quantity. In this case the dynamical charm effects seem relevant (albeit with a large statistical uncertainty) and we observe a deviation between the RGI masses of the two theories of around 5%. Indeed we find

$$\frac{[\sqrt{t_0}M_c]^{N_f=2} - [\sqrt{t_0}M_c]^{N_f=0}}{[\sqrt{t_0}M_c]^{N_f=0}} = 0.050(20). \tag{6.31}$$

Because of the uncertainty in the ratio M/m_R, the RGI masses have larger errors than the running masses. This deteriorates a bit the accuracy of our final estimate and therefore it would be certainly useful to further reduce the error on the quantity (6.31) in future works.

Chapter 7

Conclusions and future plans

In this thesis we have presented a *model study* for the evaluation of charm loop effects in QCD. Through a direct comparison of results obtained in $N_f = 0$ QCD and QCD with $N_f = 2$ degenerate charm quarks we have estimated the charm sea effects on several quantities. The aim is to understand for which kind of observables it is necessary to introduce a dynamical charm quark in lattice QCD simulations, since the inclusion of a charm quark in the *sea* typically leads to an increase of the computational costs and requires smaller lattice spacings than $N_f = 2+1$ (up, down, strange) QCD simulations, due to the large charm quark mass.

For quantities without an explicit charm-quark dependence, like the static potential and the strong coupling α_{qq} derived from the static force, we expect negligible effects at energies much below the charm quark mass, because of decoupling [16, 17]. However, this kind of quantities gives also the possibility to explore short-distance physics, where decoupling no longer applies. The results of our investigation further confirm decoupling of heavy quarks at low energies. Both for the static potential and the strong coupling α_{qq} we observe that charm sea effects are completely negligible at distances $r \gg \frac{1}{M_c} \approx 0.13$ fm, where M_c is the RGI mass of a charm quark. On the other hand, at $r \lesssim 0.13$ fm the charm sea effects become clearly visible and at $r \approx 0.06$ fm we find a relative effect on α_{qq} of around 6%.

We also focus on quantities with an explicit charm-quark dependence, where in principle decoupling does not apply, because the charm quarks cannot be completely removed after fermionic integration. From our investigations, we conclude that the effects of a dynamical charm quark are sizable for the RGI mass M_c (around 5%) and tiny on the vector mass $m_{J/\psi}$ (around 0.1%)[1]. For the hyperfine splitting $(m_{J/\psi} - m_{\eta_c})/m_{\eta_c}$ we observe a 2% effect, albeit with a large statistical uncertainty. Our preliminary studies of charmonium decay constants seem to indicate that the effect of dynamical charm quarks is tiny also on the pseudoscalar decay constant f_{η_c} (smaller than 0.78%) and on the vector decay constant $f_{J/\psi}$ (smaller than 1.4%).

Notice that the size of dynamical charm effects given here refers to our model with $N_f = 2$ charm quarks. If these effects originate from charm loops, the leading contribution comes from one loop (due to the heavy quark mass) and is proportional to N_f. In Nature charm loop

[1] The matching of the charm mass in $N_f = 0$ and $N_f = 2$ QCD has been performed through the pseudoscalar mass m_{η_c}.

effects are to a good approximation half of the ones we measure in our model. From our studies it seems that decoupling also applies to differences of binding energies of charmonium. We expect that the size of dynamical charm effects in binding energies of charmonium is a factor 0.5 smaller in Nature than in our model calculation with two charm quarks.

In the near future we plan to study also other charmonium states (χ_{c0}, χ_{c1}, h_c) to have a more complete scenario of the charm loop effects on the lightest particles of the charmonium spectrum, exploring different quantum numbers J^{PC}. It can also be interesting to study the effects of a dynamical charm quark on the hyperfine splitting of a B_c meson made of a bottom quark (antiquark) and a charm antiquark (quark). Our simplified setup gives the possibility to reach fine lattice spacings and to provide an estimate of the charm sea effects on the masses of charmed B mesons. Since the first observation of the B_c meson by the CDF collaboration at Fermilab's Tevatron in 1998, the properties of the charmed B meson system are of special interest in quarkonium spectroscopy, because they are the only quarkonia consisting of heavy quarks with different flavours. Because they carry flavour, they cannot annihilate into gluons and so are more stable with widths less than a hundred keV. At the LHC, with its higher luminosity, the spectroscopy and decay of $B_c^\star$ mesons can now be experimentally measured with much better confidence such that, on the theory side, precision studies of these meson states by means of lattice QCD become increasingly important.

Bibliography

[1] W. N. Cottingham and D. A. Greenwood, *An introduction to the standard model of particle physics*. Cambridge University Press, 2007.

[2] Wikipedia, "Standard model." https://en.wikipedia.org/wiki/Standard_Model, 2019.

[3] P. W. Higgs, *Broken Symmetries and the Masses of Gauge Bosons*, *Phys. Rev. Lett.* **13** (1964) 508.

[4] F. Englert and R. Brout, *Broken Symmetry and the Mass of Gauge Vector Mesons*, *Phys. Rev. Lett.* **13** (1964) 321.

[5] ATLAS collaboration, G. Aad et al., *Observation of a new particle in the search for the Standard Model Higgs boson with the ATLAS detector at the LHC*, *Phys. Lett.* **B716** (2012) 1 [1207.7214].

[6] CMS collaboration, S. Chatrchyan et al., *Observation of a new boson at a mass of 125 GeV with the CMS experiment at the LHC*, *Phys. Lett.* **B716** (2012) 30 [1207.7235].

[7] W. Heisenberg, *On the structure of atomic nuclei*, *Z. Phys.* **77** (1932) 1.

[8] M. Gell-Mann, *A Schematic Model of Baryons and Mesons*, *Phys. Lett.* **8** (1964) 214.

[9] G. Zweig, *An SU(3) model for strong interaction symmetry and its breaking. Version 2*, in *DEVELOPMENTS IN THE QUARK THEORY OF HADRONS. VOL. 1. 1964 - 1978* (D. Lichtenberg and S. P. Rosen, eds.), pp. 22–101. 1964.

[10] O. W. Greenberg, *Spin and Unitary Spin Independence in a Paraquark Model of Baryons and Mesons*, *Phys. Rev. Lett.* **13** (1964) 598.

[11] M. Y. Han and Y. Nambu, *Three Triplet Model with Double SU(3) Symmetry*, *Phys. Rev.* **139** (1965) B1006.

[12] Y. Nambu, *A systematics of hadrons in subnuclear physics*, *Preludes in Theoretical Physics* (1966) 133.

[13] D. J. Gross and F. Wilczek, *Ultraviolet Behavior of Nonabelian Gauge Theories*, *Phys. Rev. Lett.* **30** (1973) 1343.

[14] H. D. Politzer, *Reliable Perturbative Results for Strong Interactions?*, *Phys. Rev. Lett.* **30** (1973) 1346.

[15] K. G. Wilson, *Confinement of Quarks*, *Phys. Rev.* **D10** (1974) 2445.

[16] T. Appelquist and J. Carazzone, *Infrared Singularities and Massive Fields*, *Phys. Rev.* **D11** (1975) 2856.

[17] S. Weinberg, *Effective Gauge Theories*, *Phys. Lett.* **91B** (1980) 51.

[18] PARTICLE DATA GROUP collaboration, M. Tanabashi et al., *Review of Particle Physics*, *Phys. Rev.* **D98** (2018) 030001.

[19] C.-N. Yang and R. L. Mills, *Conservation of Isotopic Spin and Isotopic Gauge Invariance*, *Phys. Rev.* **96** (1954) 191.

[20] M. E. Peskin and D. V. Schroeder, *An Introduction to quantum field theory*. Addison-Wesley, Reading, USA, 1995.

[21] M. Maggiore, *A Modern introduction to quantum field theory*, Oxford Series in Physics. Oxford University Press, 2005.

[22] G. 't Hooft, *Dimensional regularization and the renormalization group*, *Nucl. Phys.* **B61** (1973) 455.

[23] W. A. Bardeen, A. J. Buras, D. W. Duke and T. Muta, *Deep Inelastic Scattering Beyond the Leading Order in Asymptotically Free Gauge Theories*, *Phys. Rev.* **D18** (1978) 3998.

[24] C. G. Callan, Jr., *Broken scale invariance in scalar field theory*, *Phys. Rev.* **D2** (1970) 1541.

[25] K. Symanzik, *Small distance behavior in field theory and power counting*, *Commun. Math. Phys.* **18** (1970) 227.

[26] W. E. Caswell, *Asymptotic Behavior of Nonabelian Gauge Theories to Two Loop Order*, *Phys. Rev. Lett.* **33** (1974) 244.

[27] D. R. T. Jones, *Two Loop Diagrams in Yang-Mills Theory*, *Nucl. Phys.* **B75** (1974) 531.

[28] S. A. Larin and J. A. M. Vermaseren, *The Three loop QCD Beta function and anomalous dimensions*, *Phys. Lett.* **B303** (1993) 334 [hep-ph/9302208].

[29] T. van Ritbergen, J. A. M. Vermaseren and S. A. Larin, *The Four loop beta function in quantum chromodynamics*, *Phys. Lett.* **B400** (1997) 379 [hep-ph/9701390].

[30] M. Czakon, *The Four-loop QCD beta-function and anomalous dimensions*, *Nucl. Phys.* **B710** (2005) 485 [hep-ph/0411261].

[31] P. A. Baikov, K. G. Chetyrkin and J. H. Kühn, *Five-Loop Running of the QCD coupling constant*, *Phys. Rev. Lett.* **118** (2017) 082002 [1606.08659].

[32] T. Luthe, A. Maier, P. Marquard and Y. Schröder, *Towards the five-loop Beta function for a general gauge group*, *JHEP* **07** (2016) 127 [1606.08662].

[33] F. Herzog, B. Ruijl, T. Ueda, J. A. M. Vermaseren and A. Vogt, *The five-loop beta function of Yang-Mills theory with fermions*, *JHEP* **02** (2017) 090 [1701.01404].

[34] K. G. Chetyrkin, *Quark mass anomalous dimension to O (alpha-s**4)*, *Phys. Lett.* **B404** (1997) 161 [hep-ph/9703278].

[35] ALPHA collaboration, S. Sint and P. Weisz, *The Running quark mass in the SF scheme and its two loop anomalous dimension*, *Nucl. Phys.* **B545** (1999) 529 [hep-lat/9808013].

[36] ALPHA collaboration, T. Korzec, *Determination of the Strong Coupling Constant by the ALPHA Collaboration*, *EPJ Web Conf.* **175** (2018) 01018 [1711.01084].

[37] S. Aoki et al., *Review of lattice results concerning low-energy particle physics*, *Eur. Phys. J.* **C77** (2017) 112 [1607.00299].

[38] S. L. Adler, *Axial vector vertex in spinor electrodynamics*, *Phys. Rev.* **177** (1969) 2426.

[39] J. S. Bell and R. Jackiw, *A PCAC puzzle: $\pi^0 \to \gamma\gamma$ in the σ model*, *Nuovo Cim.* **A60** (1969) 47.

[40] G. 't Hooft, *Symmetry Breaking Through Bell-Jackiw Anomalies*, *Phys. Rev. Lett.* **37** (1976) 8.

[41] K. Fujikawa, *Path Integral Measure for Gauge Invariant Fermion Theories*, *Phys. Rev. Lett.* **42** (1979) 1195.

[42] E. Witten, *Current Algebra Theorems for the U(1) Goldstone Boson*, *Nucl. Phys.* **B156** (1979) 269.

[43] G. Veneziano, *U(1) Without Instantons*, *Nucl. Phys.* **B159** (1979) 213.

[44] J. Goldstone, A. Salam and S. Weinberg, *Broken Symmetries*, *Phys. Rev.* **127** (1962) 965.

[45] V. Koch, *Introduction to chiral symmetry*, in *3rd TAPS Workshop on Electromagnetic and Mesonic Probes of Nuclear Matter Bosen, Germany, September 10-15, 1995*, 1995, `nucl-th/9512029`.

[46] A. Athenodorou, J. Finkenrath, F. Knechtli, T. Korzec, B. Leder, M. K. Marinković et al., *How perturbative are heavy sea quarks?*, `1809.03383`.

[47] B. C. Tiburzi, *Chiral Perturbation Theory*, *Lect. Notes Phys.* **889** (2015) 107.

[48] ALPHA collaboration, M. Bruno, J. Finkenrath, F. Knechtli, B. Leder and R. Sommer, *Effects of Heavy Sea Quarks at Low Energies*, *Phys. Rev. Lett.* **114** (2015) 102001 [`1410.8374`].

[49] R. Sommer, *A New way to set the energy scale in lattice gauge theories and its applications to the static force and alpha-s in SU(2) Yang-Mills theory*, *Nucl. Phys.* **B411** (1994) 839 [`hep-lat/9310022`].

[50] M. Lüscher, *Properties and uses of the Wilson flow in lattice QCD*, *JHEP* **08** (2010) 071 [`1006.4518`].

[51] W. Bernreuther and W. Wetzel, *Decoupling of Heavy Quarks in the Minimal Subtraction Scheme*, *Nucl. Phys.* **B197** (1982) 228.

[52] K. G. Chetyrkin, J. H. Kuhn and C. Sturm, *QCD decoupling at four loops*, *Nucl. Phys.* **B744** (2006) 121 [`hep-ph/0512060`].

[53] Y. Schroder and M. Steinhauser, *Four-loop decoupling relations for the strong coupling*, *JHEP* **01** (2006) 051 [`hep-ph/0512058`].

[54] H. J. Rothe, *Lattice gauge theories: An Introduction*, *World Sci. Lect. Notes Phys.* **43** (1992) 1.

[55] I. Montvay and G. Munster, *Quantum fields on a lattice*, Cambridge Monographs on Mathematical Physics. Cambridge University Press, 1997, 10.1017/CBO9780511470783.

[56] C. Gattringer and C. B. Lang, *Quantum chromodynamics on the lattice*, *Lect. Notes Phys.* **788** (2010) 1.

[57] F. Knechtli, M. Günther and M. Peardon, *Lattice Quantum Chromodynamics: Practical Essentials*, SpringerBriefs in Physics. Springer, 2017, 10.1007/978-94-024-0999-4.

[58] B. Sheikholeslami and R. Wohlert, *Improved Continuum Limit Lattice Action for QCD with Wilson Fermions*, *Nucl. Phys.* **B259** (1985) 572.

[59] ALPHA collaboration, R. Frezzotti, P. A. Grassi, S. Sint and P. Weisz, *Lattice QCD with a chirally twisted mass term*, *JHEP* **08** (2001) 058 [hep-lat/0101001].

[60] R. Frezzotti and G. C. Rossi, *Chirally improving Wilson fermions. 1. O(a) improvement*, *JHEP* **08** (2004) 007 [hep-lat/0306014].

[61] T. Reisz and H. J. Rothe, *Renormalization of lattice gauge theories with massless Ginsparg Wilson fermions*, *Nucl. Phys.* **B575** (2000) 255 [hep-lat/9908013].

[62] J. B. Kogut and L. Susskind, *Hamiltonian Formulation of Wilson's Lattice Gauge Theories*, *Phys. Rev.* **D11** (1975) 395.

[63] H. B. Nielsen and M. Ninomiya, *No Go Theorem for Regularizing Chiral Fermions*, *Phys. Lett.* **105B** (1981) 219.

[64] M. Lüscher, *Exact chiral symmetry on the lattice and the Ginsparg-Wilson relation*, *Phys. Lett.* **B428** (1998) 342 [hep-lat/9802011].

[65] P. H. Ginsparg and K. G. Wilson, *A Remnant of Chiral Symmetry on the Lattice*, *Phys. Rev.* **D25** (1982) 2649.

[66] G. Heatlie, G. Martinelli, C. Pittori, G. C. Rossi and C. T. Sachrajda, *The improvement of hadronic matrix elements in lattice QCD*, *Nucl. Phys.* **B352** (1991) 266.

[67] K. Symanzik, *Continuum Limit and Improved Action in Lattice Theories. 1. Principles and phi**4 Theory*, *Nucl. Phys.* **B226** (1983) 187.

[68] K. Symanzik, *Continuum Limit and Improved Action in Lattice Theories. 2. O(N) Nonlinear Sigma Model in Perturbation Theory*, *Nucl. Phys.* **B226** (1983) 205.

[69] M. Lüscher, S. Sint, R. Sommer and P. Weisz, *Chiral symmetry and O(a) improvement in lattice QCD*, *Nucl. Phys.* **B478** (1996) 365 [hep-lat/9605038].

[70] M. Lüscher, *Advanced lattice QCD*, in *Probing the standard model of particle interactions. Proceedings, Summer School in Theoretical Physics, NATO Advanced Study Institute, 68th session, Les Houches, France, July 28-September 5, 1997. Pt. 1, 2*, pp. 229–280, 1998, hep-lat/9802029.

[71] M. Lüscher, S. Sint, R. Sommer, P. Weisz and U. Wolff, *Nonperturbative O(a) improvement of lattice QCD*, *Nucl. Phys.* **B491** (1997) 323 [hep-lat/9609035].

[72] ALPHA collaboration, K. Jansen and R. Sommer, *O(a) improvement of lattice QCD with two flavors of Wilson quarks*, *Nucl. Phys.* **B530** (1998) 185 [hep-lat/9803017].

[73] S. Sint, *Lattice QCD with a chiral twist*, in *Workshop on Perspectives in Lattice QCD Nara, Japan, October 31-November 11, 2005*, 2007, hep-lat/0702008, DOI.

[74] A. Shindler, *Twisted mass lattice QCD*, *Phys. Rept.* **461** (2008) 37 [0707.4093].

[75] XLF collaboration, K. Jansen, M. Papinutto, A. Shindler, C. Urbach and I. Wetzorke, *Light quarks with twisted mass fermions*, *Phys. Lett.* **B619** (2005) 184 [hep-lat/0503031].

[76] J. Finkenrath, F. Knechtli and B. Leder, *One flavor mass reweighting in lattice QCD*, *Nucl. Phys.* **B877** (2013) 441 [1306.3962].

[77] ALPHA collaboration, U. Wolff, *Monte Carlo errors with less errors*, *Comput. Phys. Commun.* **156** (2004) 143 [hep-lat/0306017].

[78] M. Lüscher, *Computational Strategies in Lattice QCD*, in *Modern perspectives in lattice QCD: Quantum field theory and high performance computing. Proceedings, International School, 93rd Session, Les Houches, France, August 3-28, 2009*, pp. 331–399, 2010, 1002.4232.

[79] M. Lüscher and S. Schaefer, *Lattice QCD without topology barriers*, *JHEP* **07** (2011) 036 [1105.4749].

[80] M. Bruno, T. Korzec and S. Schaefer, *Setting the scale for the CLS* $2+1$ *flavor ensembles*, *Phys. Rev.* **D95** (2017) 074504 [1608.08900].

[81] HADRON SPECTRUM collaboration, H.-W. Lin et al., *First results from 2+1 dynamical quark flavors on an anisotropic lattice: Light-hadron spectroscopy and setting the strange-quark mass*, *Phys. Rev.* **D79** (2009) 034502 [0810.3588].

[82] PACS-CS collaboration, S. Aoki et al., *Physical Point Simulation in 2+1 Flavor Lattice QCD*, *Phys. Rev.* **D81** (2010) 074503 [0911.2561].

[83] W. Bietenholz et al., *Tuning the strange quark mass in lattice simulations*, *Phys. Lett.* **B690** (2010) 436 [1003.1114].

[84] RBC, UKQCD collaboration, R. Arthur et al., *Domain Wall QCD with Near-Physical Pions*, *Phys. Rev.* **D87** (2013) 094514 [1208.4412].

[85] M. Bruno et al., *Simulation of QCD with* $N_f = 2 + 1$ *flavors of non-perturbatively improved Wilson fermions*, *JHEP* **02** (2015) 043 [1411.3982].

[86] M. Lüscher, *Volume Dependence of the Energy Spectrum in Massive Quantum Field Theories. 1. Stable Particle States*, *Commun. Math. Phys.* **104** (1986) 177.

[87] ALPHA collaboration, F. Knechtli, M. Bruno, J. Finkenrath, B. Leder and R. Sommer, *Perturbative versus non-perturbative decoupling of heavy quarks*, *PoS* **LATTICE2015** (2016) 256 [1511.04914].

[88] ALPHA collaboration, F. Knechtli, T. Korzec, B. Leder and G. Moir, *Power corrections from decoupling of the charm quark*, *Phys. Lett.* **B774** (2017) 649 [1706.04982].

[89] T. Korzec, "Meson correlators." https://github.com/to-ko/mesons, 2014.

[90] T. Korzec, "mesons relase 1.2." https://github.com/to-ko/mesons, 2014.

[91] UKQCD collaboration, C. Michael and J. Peisa, *Maximal variance reduction for stochastic propagators with applications to the static quark spectrum*, *Phys. Rev.* **D58** (1998) 034506 [hep-lat/9802015].

[92] V. Koch, *Aspects of chiral symmetry*, *Int. J. Mod. Phys.* **E6** (1997) 203 [nucl-th/9706075].

[93] C. T. H. Davies, C. McNeile, E. Follana, G. P. Lepage, H. Na and J. Shigemitsu, *Update: Precision* D_s *decay constant from full lattice QCD using very fine lattices*, *Phys. Rev.* **D82** (2010) 114504 [1008.4018].

[94] XLF collaboration, K. Jansen, A. Shindler, C. Urbach and I. Wetzorke, *Scaling test for Wilson twisted mass QCD*, *Phys. Lett.* **B586** (2004) 432 [hep-lat/0312013].

[95] M. Bruno, *The energy scale of the 3-flavour Lambda parameter*, Ph.D. thesis, Humboldt U., Berlin, 2015.

[96] S. Necco and R. Sommer, *The N(f) = 0 heavy quark potential from short to intermediate distances*, *Nucl. Phys.* **B622** (2002) 328 [hep-lat/0108008].

[97] M. Alberti, G. S. Bali, S. Collins, F. Knechtli, G. Moir and W. Söldner, *Hadroquarkonium from lattice QCD*, *Phys. Rev.* **D95** (2017) 074501 [1608.06537].

[98] E. Eichten, K. Gottfried, T. Kinoshita, J. B. Kogut, K. D. Lane and T.-M. Yan, *The Spectrum of Charmonium*, *Phys. Rev. Lett.* **34** (1975) 369.

[99] R. Sommer, *Scale setting in lattice QCD*, *PoS* **LATTICE2013** (2014) 015 [1401.3270].

[100] M. Donnellan, F. Knechtli, B. Leder and R. Sommer, *Determination of the Static Potential with Dynamical Fermions*, *Nucl. Phys.* **B849** (2011) 45 [1012.3037].

[101] M. Peter, *The Static potential in QCD: A Full two loop calculation*, *Nucl. Phys.* **B501** (1997) 471 [hep-ph/9702245].

[102] Y. Schroder, *The Static potential in QCD to two loops*, *Phys. Lett.* **B447** (1999) 321 [hep-ph/9812205].

[103] N. Brambilla, A. Pineda, J. Soto and A. Vairo, *Potential NRQCD: An Effective theory for heavy quarkonium*, *Nucl. Phys.* **B566** (2000) 275 [hep-ph/9907240].

[104] C. Anzai, Y. Kiyo and Y. Sumino, *Static QCD potential at three-loop order*, *Phys. Rev. Lett.* **104** (2010) 112003 [0911.4335].

[105] A. V. Smirnov, V. A. Smirnov and M. Steinhauser, *Three-loop static potential*, *Phys. Rev. Lett.* **104** (2010) 112002 [0911.4742].

[106] A. Hasenfratz and F. Knechtli, *Flavor symmetry and the static potential with hypercubic blocking*, *Phys. Rev.* **D64** (2001) 034504 [hep-lat/0103029].

[107] APE collaboration, M. Albanese et al., *Glueball Masses and String Tension in Lattice QCD*, *Phys. Lett.* **B192** (1987) 163.

[108] M. Della Morte, A. Shindler and R. Sommer, *On lattice actions for static quarks*, *JHEP* **08** (2005) 051 [hep-lat/0506008].

[109] A. Grimbach, D. Guazzini, F. Knechtli and F. Palombi, *O(a) improvement of the HYP static axial and vector currents at one-loop order of perturbation theory*, *JHEP* **03** (2008) 039 [0802.0862].

[110] ALPHA collaboration, F. Knechtli and R. Sommer, *String breaking in SU(2) gauge theory with scalar matter fields*, *Phys. Lett.* **B440** (1998) 345 [hep-lat/9807022].

[111] O. Philipsen and H. Wittig, *String breaking in nonAbelian gauge theories with fundamental matter fields*, *Phys. Rev. Lett.* **81** (1998) 4056 [hep-lat/9807020].

[112] ALPHA collaboration, F. Knechtli and R. Sommer, *String breaking as a mixing phenomenon in the SU(2) Higgs model*, *Nucl. Phys.* **B590** (2000) 309 [hep-lat/0005021].

[113] SESAM collaboration, G. S. Bali, H. Neff, T. Duessel, T. Lippert and K. Schilling, *Observation of string breaking in QCD*, *Phys. Rev.* **D71** (2005) 114513 [hep-lat/0505012].

[114] J. Bulava, B. Hörz, F. Knechtli, V. Koch, G. Moir, C. Morningstar et al., *String breaking by light and strange quarks in QCD*, 1902.04006.

[115] R. Sommer, *Introduction to Non-perturbative Heavy Quark Effective Theory*, in *Modern perspectives in lattice QCD: Quantum field theory and high performance computing. Proceedings, International School, 93rd Session, Les Houches, France, August 3-28, 2009*, pp. 517–590, 2010, 1008.0710.

[116] S. Borsanyi et al., *High-precision scale setting in lattice QCD*, *JHEP* **09** (2012) 010 [1203.4469].

[117] P. Fritzsch, F. Knechtli, B. Leder, M. Marinkovic, S. Schaefer, R. Sommer et al., *The strange quark mass and Lambda parameter of two flavor QCD*, *Nucl. Phys.* **B865** (2012) 397 [1205.5380].

[118] ALPHA collaboration, B. Blossier, M. Della Morte, P. Fritzsch, N. Garron, J. Heitger, H. Simma et al., *Parameters of Heavy Quark Effective Theory from Nf=2 lattice QCD*, *JHEP* **09** (2012) 132 [1203.6516].

[119] ALPHA collaboration, P. Fritzsch, N. Garron and J. Heitger, *Non-perturbative tests of continuum HQET through small-volume two-flavour QCD*, *JHEP* **01** (2016) 093 [1508.06938].

[120] P. Dimopoulos, H. Simma and A. Vladikas, *Quenched B(K)-parameter from Osterwalder-Seiler tmQCD quarks and mass-splitting discretization effects*, *JHEP* **07** (2009) 007 [0902.1074].

[121] F. Knechtli, T. Korzec, B. Leder and G. Moir, *Decoupling of charm beyond leading order*, *EPJ Web Conf.* **175** (2018) 10001 [1710.07590].

[122] T. Korzec, F. Knechtli, S. Calì, B. Leder and G. Moir, *Impact of dynamical charm quarks*, *PoS* **LATTICE2016** (2017) 126 [1612.07634].

[123] S. Calì, F. Knechtli, T. Korzec and H. Panagopoulos, *Charm quark effects on the strong coupling extracted from the static force*, *EPJ Web Conf.* **175** (2018) 10002 [1710.06221].

[124] B. Blossier, M. Della Morte, G. von Hippel, T. Mendes and R. Sommer, *On the generalized eigenvalue method for energies and matrix elements in lattice field theory*, *JHEP* **04** (2009) 094 [0902.1265].

[125] M. Lüscher, P. Weisz and U. Wolff, *A Numerical method to compute the running coupling in asymptotically free theories*, *Nucl. Phys.* **B359** (1991) 221.

[126] ALPHA collaboration, M. Dalla Brida, P. Fritzsch, T. Korzec, A. Ramos, S. Sint and R. Sommer, *Slow running of the Gradient Flow coupling from 200 MeV to 4 GeV in $N_{\rm f} = 3$ QCD*, *Phys. Rev.* **D95** (2017) 014507 [1607.06423].

[127] N. Husung, M. Koren, P. Krah and R. Sommer, *SU(3) Yang Mills theory at small distances and fine lattices*, *EPJ Web Conf.* **175** (2018) 14024 [1711.01860].

[128] S. Capitani, M. Lüscher, R. Sommer and H. Wittig, *Non-perturbative quark mass renormalization in quenched lattice QCD*, *Nucl. Phys.* **B544** (1999) 669 [hep-lat/9810063].

[129] S. Necco, *The Static quark potential and scaling behavior of SU(3) lattice Yang-Mills theory*, Ph.D. thesis, Humboldt U., Berlin, 2003. hep-lat/0306005.

[130] J. Heitger, G. M. von Hippel, S. Schaefer and F. Virotta, *Charm quark mass and D-meson decay constants from two-flavour lattice QCD*, *PoS* **LATTICE2013** (2014) 475 [1312.7693].

[131] S. Calì, F. Knechtli and T. Korzec, *Comparison between models of QCD with and without dynamical charm quarks*, in *36th International Symposium on Lattice Field Theory (Lattice 2018) East Lansing, MI, United States, July 22-28, 2018*, 2018, 1811.05285.

[132] S. Calì, F. Knechtli and T. Korzec, *How much do charm sea quarks affect the charmonium spectrum?*, 1905.12971.

[133] M. Lüscher, S. Sint, R. Sommer and H. Wittig, *Nonperturbative determination of the axial current normalization constant in O(a) improved lattice QCD*, *Nucl. Phys.* **B491** (1997) 344 [hep-lat/9611015].

[134] M. Della Morte, R. Hoffmann, F. Knechtli, R. Sommer and U. Wolff, *Non-perturbative renormalization of the axial current with dynamical Wilson fermions*, *JHEP* **07** (2005) 007 [hep-lat/0505026].

[135] M. Dalla Brida, T. Korzec, S. Sint and P. Vilaseca, *High precision renormalization of the flavour non-singlet Noether currents in lattice QCD with Wilson quarks*, *Eur. Phys. J.* **C79** (2019) 23 [1808.09236].

[136] G. M. de Divitiis, R. Petronzio and N. Tantalo, *Distance preconditioning for lattice Dirac operators*, *Phys. Lett.* **B692** (2010) 157 [1006.4028].

[137] S. Collins, K. Eckert, J. Heitger, S. Hofmann and W. Soeldner, *Charmed pseudoscalar decay constants on three-flavour CLS ensembles with open boundaries*, *PoS* **LATTICE2016** (2017) 368 [1701.05502].

[138] ALPHA collaboration, M. Della Morte, R. Hoffmann, F. Knechtli, J. Rolf, R. Sommer, I. Wetzorke et al., *Non-perturbative quark mass renormalization in two-flavor QCD*, *Nucl. Phys.* **B729** (2005) 117 [hep-lat/0507035].

[139] ALPHA collaboration, M. Della Morte, R. Frezzotti, J. Heitger, J. Rolf, R. Sommer and U. Wolff, *Computation of the strong coupling in QCD with two dynamical flavors*, *Nucl. Phys.* **B713** (2005) 378 [hep-lat/0411025].

[140] J. Heitger and A. Juttner, *Lattice cutoff effects for F(D(s)) with improved Wilson fermions: A Final lesson from the quenched case*, *JHEP* **05** (2009) 101 [0812.2200].

[141] A. Juttner, *Precision lattice computations in the heavy quark sector*, Ph.D. thesis, Humboldt U., Berlin, 2004. hep-lat/0503040.